LAWRENCE
LIVERMORE
NATIONAL
LABORATORY

LLNL-TR-411150

The Properties of Confined Water and Fluid Flow at the Nanoscale

E. Schwegler, J. Reed, E. Lau, D. Prendergast, G. Galli, J. C. Grossman, G. Cicero

March 10, 2009

Disclaimer

This work performed under the auspices of the U.S. Department of Energy by Lawrence Livermore National Laboratory under Contract DE-AC52-07NA27344.

FY08 LDRD Final Report
The Properties of Confined Water and Fluid Flow at the Nanoscale
LDRD Project Tracking Code: 06-ERD-039
Eric Schwegler, Principal Investigator

Abstract
This project has been focused on the development of accurate computational tools to study fluids in confined, nanoscale geometries, and the application of these techniques to probe the structural and electronic properties of water confined between hydrophilic and hydrophobic substrates, including the presence of simple ions at the interfaces. In particular, we have used a series of ab-initio molecular dynamics simulations and quantum Monte Carlo calculations to build an understanding of how hydrogen bonding and solvation are modified at the nanoscale. The properties of confined water affect a wide range of scientific and technological problems – including protein folding, cell-membrane flow, materials properties in confined media and nanofluidic devices.

Introduction/Background
While the properties of the bulk fluid are relatively well characterized, much less is known about water confined at the nanometer scale, where conventional experimental probes (e.g. neutron diffraction and X-ray scattering) are difficult to use and accurate simulations become extremely challenging. Equilibrium properties, phase transformations and molecular mobility of water have all been observed to change upon confinement, however a thorough characterization of these changes is still missing.

A number of theoretical studies using both molecular dynamics and Monte Carlo techniques have been carried out to address some of the issues involved in confined water. However, it should be noted that the existing simulations have all been based on empirically derived classical potentials. Since these potentials are usually designed to reproduce the properties of bulk water, and it is unclear whether they can accurately describe confined states as well. Furthermore, in many situations subtle electronic effects play an important role in understanding the behavior of both water-water and water-solute interactions, and usually these cannot be captured using simple classical potentials.

The primary benefits of this research project are in three areas: (i) the development of a first-principles based computational framework for investigating and characterizing liquids that are confined at the nanoscale, (ii) the application of these advanced computational methods to gain a better understanding of how the properties of water change upon nanoscale confinement by hydrophobic and hydrophilic surfaces, and (iii) the development and validation of a suitable empirical model that can be used to describe the flow of water in confined media.

Research Activities
In the following sections, we briefly describe the main systems that have been examined in this project, including the solvation of small hydrophobic solutes[1,2], and

the structural[3], vibrational[4,5] and magnetic response[6] of confined water. Additional detailed information can be found in the attached papers.

Over the course of this project, we made significant progress in using first-principles molecular dynamics simulations to examine a series of prototypical confined water systems. *i.e.* water inside carbon nanotubes and between graphitic sheets, 1 to 2.5 nm apart. Our simulations indicate the presence of a thin, interfacial liquid layer (~5 Å) whose macroscopic density depends on surface separation, but whose microscopic structure and thickness are independent of the distance between confining layers. The properties of the hydrogen-bond network are very similar to those of the bulk outside the interfacial region, in spite of the breaking of hydrogen bonds at the interface, and even in the case of strong confinement. These results indicate that the perturbation induced by the presence of confining media is extremely local in liquid water, and we propose that many of the effects attributed to novel phases under confinement are determined by subtle electronic structure rearrangements occurring at the interface with the confining medium. We also find that lateral diffusion is significantly enhanced in confined water compared to bulk diffusion, due to a decrease of the dipole moment of interfacial molecules, and correspondingly a decrease in hydrogen bond strength, compared to the bulk liquid. In the following, the structural and dynamical properties of confined water are discussed in detail along with preliminary results on ion solvation in carbon nanotubes.

1. Structural Properties

As illustrated in Fig. 1, when liquid water is confined by a hydrophobic surface, the presence of the solid-liquid interface causes pronounced density oscillations in the liquid[7,8]. In the case of confinement by graphitic sheets, we found that water molecules are excluded from a region with a thickness of ~2.5 Å; the particle density rises sharply outside this excluded volume, with a first peak extending up to ~5 Å. The height of this peak increases with decreasing distance between the surfaces (from 2.38 g/cm^3 to 1.96 g/cm^3 in going from 10.09 to 25.02 Å confinement distances), but its position is independent of the confining length. From a comparison of the top panels of Fig. 1 (a-c) it is clear that increased confinement results in enhanced density oscillations. This may be understood in terms of interfering effects of the two facing surfaces, and at extreme confinement the perturbation induced on water at the two interfaces is amplified. In panel (c) of Fig. 1, where the distance between graphitic sheets is the largest (25.02 Å), density oscillations are nearly suppressed, indicating that interference is minimal and the effect of the surface perturbation is highly localized. In this case, only the water layer in contact with the surface has density higher than the bulk; beyond ~5 Å from the

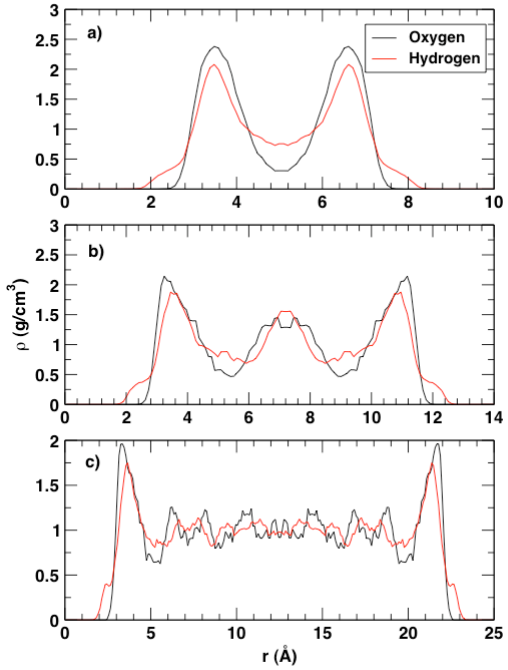

Fig.1 The density profile of oxygen (black curve) and hydrogen (red cuve) from water confined by graphitic sheets separated by a) 10 Å, b) 14 Å, and c) 25 Å.

surface the density curve becomes flatter and reaches the bulk value (1.0 g/cm^3).

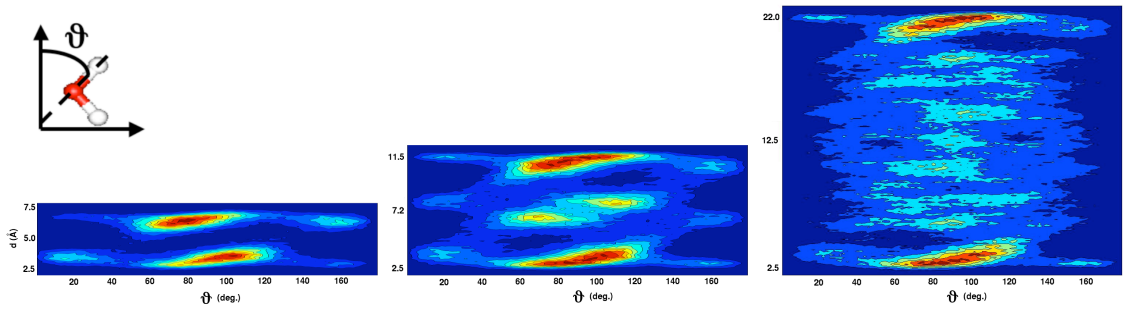

Fig. 2 Tilt angle distribution for water molecules confined between graphitic sheets at the same separations listed in Fig. 1.

We note that in all of the hydrogen density profiles reported in Fig. 1, a small shoulder is present in the first density peak, which indicates a slight preference for some interfacial water molecules to point an OH bond towards the surface. To further illustrate this effect, in Fig. 2 the OH tilt angle distribution for water confined between graphite sheets. The color maps represent the probability of finding, at a certain distance from the surface, an OH bond forming a specific angle (θ) with the direction perpendicular to the surface. Near the solid-liquid interface, the water molecules have strong preferential orientations. In particular, at about 2.7 Å from the surface two angles are favored: 75° and 150°. This geometric configuration corresponds to water molecules having one of the OH bonds nearly parallel to the surface and the other pointing towards it. At 3.3 Å, the opposite orientation in found with an OH pointing away from the surface (25°) and the other nearly parallel (100°) to it. At about 3 Å, there is a strong peak at 90°, indicating that most of the molecules have both OH bonds roughly parallel to the surface. In the high-density layer, the planar orientation is preferred in order to maximize in-plane hydrogen bonds. The most remarkable feature of the distributions shown in Fig. 2, is that the orientation of water bonds in the interfacial layer does not depend on surface separation. At a distance of 10.09 Å, the system consists of only two water layers, yet these appear to be nearly equivalent to the two interfacial layers observed for the 25.02 Å separation. A similar behavior is found in the case of water confined in carbon nanotubes when calculating the orientation of the OH bonds with respect to the radial direction. Although the preferential angles are slightly different because the surface is curved, the qualitative features of the angular distribution are very similar, and the interfacial layer structuring appears to be independent on the confining distance (*i.e.* tube diameter).

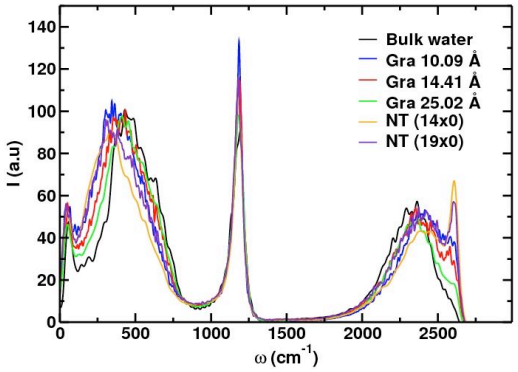

Fig. 3 The vibrational power spectra of water confined by graphitic sheets (Gra) and carbon nanotubes (NT). The spectrum for bulk water is reported for comparison.

2. Dynamical Properties

In Fig. 3, the power spectrum of the hydrogen atoms velocity autocorrelation function is shown, which is related to the IR spectrum of the sample. For confinement with both graphitic sheets and nanotubes, a peak appears at frequencies higher than in the bulk spectrum (2600 cm^{-1}), in the region of the OH stretching mode (deuterium has been used in all simulations). This signal is related to OH groups not involved in H-bonds, since these OH bonds are likely to have a higher spring constant, and to vibrate at a frequency higher than OH groups in a bulk environment. With the aim of discerning between confinement and surface effects, we artificially cut our water samples in layers of increasing distance from the interface, and we calculated the power spectra of each layer. We found that the peak at 2600 cm^{-1} is mainly related to water molecules in close proximity with the surface, with non hydrogen-bonded OH bonds likely pointing towards the surface. The water layer in the middle of the slab shows instead a power spectrum similar to that of the bulk liquid. This suggests that the peak at 2600 cm^{-1} is mainly due to a surface effect and confirms the locality of the perturbation induced by the surface on water, as observed in our structural analysis. We note that confinement enhances the high frequency power spectrum signal, as it increases the surface to volume ratio of the liquid. We believe this is the reason why the high frequency peak is more pronounced in the power spectra of water confined by carbon nanotubes than with graphitic sheets.

Another interesting region of the power spectrum of Fig. 3 is the band at low frequencies (120-800 cm^{-1}) that is usually assigned to librational modes, and thus related to intra-molecular hydrogen bonds. This band undergoes a red shift in the most confined samples, indicating a weakening of the HB strength in the interfacial region. The band at 1178 cm^{-1}, related to the water molecule bending mode, is mostly unchanged in all of our samples.

In order to investigate diffusion, we calculated the mean square displacement (MSD) of the oxygen in the direction parallel to the interface in the case of graphite and along the nanotube axes. The MSD is related to the self-diffusion coefficient through the Einstein relation, using the appropriate normalization factor for one and two-dimensional diffusion processes. Our results show that the lateral diffusion constant of water increases at extreme confinement. In particular, when the liquid is confined with a flat surface the diffusion increases with decreasing interlayer separation, and becomes 2.8×10^{-5} cm^2/s, *i.e.* almost three times larger than that calculated for the bulk (1.0×10^{-5} cm^2/s for deuterated water), for a distance of 10.09 Å. In the case of nanotubes, this effect appears to be enhanced, although it is not possible to establish a trend as a function of the tube radius from only two systems. At a diameter of 15 Å the diffusion constant reaches 3.1×10^{-5} cm^2/s, which is significantly different from that of bulk water. When decreasing the nanotube radius to 11.10 Å, the diffusion constant slightly decreases (2.3×10^{-5} cm^2/s), however remaining larger than the bulk value. In the case of two-dimensional confinement, for a CNT diameter smaller than an optimal value, the translational motion of water molecules may become so constrained that the diffusion constant does not increase as the radius decreases, unlike the case of graphitic sheets.

3. Magnetic response

We have investigated the use of DFT-based linear response theory with plane wave basis sets and periodic boundary conditions for evaluating the magnetic response and 1H-NMR chemical shieldings of water confined in carbon nanotubes (CNTs). In this investigation, the shieldings were sampled from trajectories generated via first-principles molecular dynamics simulations at ambient conditions, for water confined

in (14,0) and (19,0) CNTs with diameters of d = 11 Å and 14.9 Å, respectively. We have found that the confined water resonance is shifted upfield relative to free, bulk liquid water. In particular, for the liquid-filled CNTs that we have examined, we find the magnitude of the upfield shift can be as large as ~-23 ppm relative to unconfined liquid water. The shift is a consequence of strongly anisotropic magnetic fields induced in the CNT by an applied magnetic field. A manuscript describing this work has been completed and submitted for publication in the Journal of Physical Chemistry C.

4. Ion Solvation

In addition to examining the effects of confinement on pure liquid water, we have recently performed a series of both classical and first-principles simulations of various salt solutions confined in carbon nanotubes. These simulations were carried out in close collaboration with 07-LW-056 "The structure and transport of water and hydrated ions within hydrophobic, nanoscale channels" (PI: Jason Holt).

In Fig. 4a, the density profile is shown from a classical MD simulation of the solvation of sodium chloride in a carbon nanotube. The classical simulation is based on the SPC/E potential, which is a non-polarizable, rigid water model that is commonly used to examine the properties of confined water. In Fig 4b, the corresponding simulation based on first-principles molecular dynamics is shown. In the case of the classical molecular dynamics simulation, both the cation and the anion are fully solvated and exhibit a clear preference to reside in the inner-most layer of water. In contrast, the ions in the first-principles simulation show a strong preference for the interfacial layer between the water and the nanotube surface, with a slight preference for the anion to be located at the outermost layer. The specific ordering of the cations and anions in the interfacial region, which originates from the OH bond distribution described earlier combined with the large polarizability of the chloride anion[9], bears many interesting similarities to the liquid-vapour interface of aqueous salt solutions[10]. We are currently working to fully characterize these subtle effects, which may play an important role in understanding the transport properties of ions in nanoscale channels[11,12] (*e.g.* desalination membranes based on carbon nanotubes).

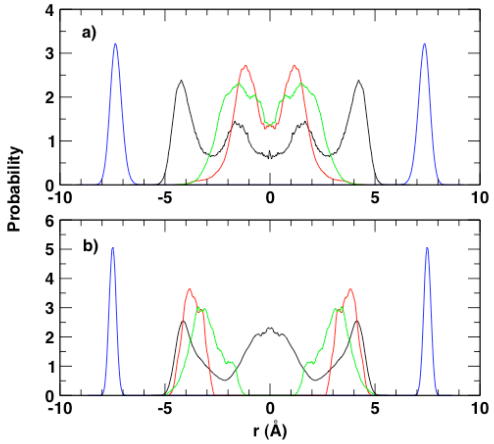

Fig. 4 The atomic density profile of an aqueous sodium chloride solution confined by a (19x0) carbon nanotube. The distribution of carbon, oxygen, sodium and chlorine atoms are represented by blue, black, green and red curves, respectively. In a) the classical SPC/E water model was used, while in b) the simulations were carried out with first-principles molecular dynamics.

Exit Plan

The research carried out within this project has formed the basis for several new projects that are currently being considered for funding. In particular, the following three proposals, which have recently been submitted for funding, are a direct result of this work:

1. *In-Situ Determination of Simulant-Surface Interaction in Aqueous Environments* (PI: Eric Schwegler), submitted to the Defense Threat Reduction Agency (DTRA), currently under review for funding in FY10-11.
2. Microscopic mechanisms of photocatalytic hydrogen production (PI: Tadashi Ogitsu), submitted to the DOE Office of Basic Energy Sciences, currently under review for possible funding in FY09.
3. *Catalytic properties of iron oxide/water interfaces from coupled atomistic and ab initio simulations* (PI: Eric Schwegler), submitted to the DOE Office of Basic Energy Sciences, currently under review for possible funding in FY09

Summary

The primary results of this research project has been in three areas: (1) the development of a first-principles based computational framework for investigating and characterizing the properties of liquids in confined media and nanofluidic devces, (2) an improved understanding of how the properties of water change upon nanoscale confinement by hydrophobic and hydrophilic surfaces, and (3) the identification of a suitable empirical model that can be used to describe the flow of water in confined media.

References

[1] M. Allesch, E. Schwegler and G. Galli "Structure of hydrophobic hydration of benzene and hexafluorobenzene from first principles" J. Phys. Chem. B **111**, 1081 (2007).

[2] M. Allesch, F.C. Lightstone, E. Schwegler, and G. Galli "First principles and classical molecular dynamics simulations of solvated benzene" J. Chem. Phys. **128**, 014501 (2008).

[3] G. Cicero, J.C. Grossman, E. Schwegler, F. Gygi and G. Galli "Water confined in nanotubes and between graphene sheets: A first principle study" J. Amer. Chem. Soc. **130**, 1871 (2008).

[4] M. Sharna, D. Donadio, E. Schwegler and G. Galli "Probing properties of water under confinement: Infrared spectra" Nano Lett. **8**, 2959 (2008).

[5] D. Donadio, G. Cicero, E. Schwegler, M. Sharma and G. Galli "Electronic effects in the IR spectrum of water under confinement" J. Phys. Chem C, accepted for publication (2008).

[6] P. Huang, E. Schweger and G. Galli "Water confined in carbon nanotubes: Magnetic response and proton chemical shieldings" J. Phys. Chem. C accepted for publication (2009).

[7] C.Y. Lee, *et al.* "The structure of liquid water at an extended hydrophobic surface" J. Chem. Phys. **80**, 4448 (1984).

[8] L. Cheng, *et al.* Phys. Rev. Lett. **87**, 156103 (2001).

[9] P. B. Petersen and R. J. Saykally "On the nature of ions at the liquid water surface" Annu. Rev. Phys. Chem. **57**, 333 (2006).

[10] P. Jungwirth and D. J. Tobias "Molecular structure of salt solutions: A new view of the interface with implications for heterogeneous atmospheric chemistry" J. Phys. Chem. B **105**, 10468 (2001).

[11] H. Liu, *et al.* "Ion permeation dynamics in carbon nanotubes" J. Chem. Phys. **125**, 084713 (2006).

[12] C. Peter and G. Hummer "Ion transport through membrane-spanning nanopores studied by molecular dynamics simulations and continuum electrostatics calculations" Biophys. J. **89**, 2222 (2005).

LAWRENCE
LIVERMORE
NATIONAL
LABORATORY

UCRL-JRNL-225529

Structure of hydrophobic hydration of benzene and hexafluorobenzene from first principles

Markus Allesch, Eric Schwegler, Giulia Galli

October 24, 2006

Journal of Physical Chemistry B

Structure of hydrophobic hydration of benzene and hexafluorobenzene from first principles

Markus Allesch,[1,2] Eric Schwegler*,[2] and Giulia Galli[2,3]

[1]*Department of Theoretical and Computational Physics, Graz University of Technology, Austria*

[2]*Lawrence Livermore National Laboratory, P.O. Box 808, Livermore, CA 84559*

[3]*University of California, Davis, CA 95616*

(Dated: August 22, 2006)

Abstract

We report on the aqueous hydration of benzene and hexafluorobenzene, as obtained by carrying out extensive (>100 ps) first principles molecular dynamics simulations. Our results show that benzene and hexafluorobenzene do not behave as ordinary hydrophobic solutes, but rather present two distinct regions, one equatorial and the other axial, that exhibit different solvation properties. While in both cases the equatorial regions behave as typical hydrophobic solutes, the solvation properties of the axial regions depend strongly on the nature of the π-water interaction. In particular, π-hydrogen and π-lone pair interactions are found to dominate in benzene and hexafluorobenzene, respectively, which leads to substantially different orientations of water near the two solutes. We present atomic and electronic structure results (in terms of Maximally Localized Wannier Functions) providing a microscopic description of benzene- and hexafluorobenzene-water interfaces, as well as a comparative study of the two solutes. Our results point at the importance of an accurate description of interfacial water in order to characterize hydration properties of apolar molecules, as these are strongly influenced by subtle charge rearrangements and dipole moment redistributions in interfacial regions.

I. INTRODUCTION

Interactions between aromatic molecules and water play a key role in determining the properties of biophysical systems, including the structure of proteins, and molecular recognition processes. In order to examine the nature of these interactions, the aqueous solvation of benzene is often used as a simple model system. Although typically referred to as a hydrophobic solute [1, 2], benzene is actually capable of forming hydrogen bonds through its π-electrons. In particular, the slight electronegativity of carbon relative to hydrogen and the overall D_{6h} symmetry of benzene leads to a large negative quadrupole moment ($\Theta = -33.3 \cdot 10^{-40} Cm^2$ [3]), which can act as a weak hydrogen bond acceptor with water [4–8].

Experimentally, the interaction of benzene with water has been the subject of numerous studies with a variety of techniques, including NMR and resonant ion dip IR spectroscopy (see, *e.g.* References [9–24]). These investigations examined the solvation of benzene in liquid water, water in liquid benzene, as well as gas-phase benzene-water clusters. Although these studies have established various important properties such as solubilities and binding energies, they are not able to provide a detailed picture of the structural and electronic properties of the local hydration structure.

Theoretical studies based on empirical potentials and *ab initio* quantum chemical methods have focused on the water-benzene dimer [2, 25, 26], and small $C_6H_6 - (H_2O)_n$ clusters [1, 27, 28]. For fully solvated species, all past investigation have been restricted to empirical potential models [29–38].

In this paper, we investigate the structural and electronic properties of fully solvated benzene using first principles molecular dynamics (FPMD) for the first time. We have also compared benzene with hexafluorobenzene, which has similar structural properties, but a very different π-electron system, with an inverse quadrupole moment ($\Theta = 31.7 \cdot 10^{-40} Cm^2$ [3]) with respect to benzene.

As compared to benzene, very little is known about the interaction of hexafluorobenzene with water. Experimental studies on the dynamics of the solvation of water in hexafluorobenzene have been performed [39] but not vice versa. Theoretical studies have focused on the hexafluorobenzene-water dimer and found a preferred water orientation that is roughly opposite to the one found for the benzene-water dimer [40–43]. However, no experimental

nor theoretical study on the solvation structure around fully solvated hexafluorobenzene has been reported to date. To the best of our knowledge, the simulations presented here are the first *ab initio* molecular dynamics studies of these two, fully solvated systems.

Simulating these aqueous solutions presents challenging size and time scale requirements because highly accurate simulations of the order of 100 ps are required to get statistically meaningful averages for structural properties. Therefore, we have used our previously developed rigid water approximation [44] to perform FPMD simulations of the different solutes for more than 100 ps, which constitute the most extensive simulations of its kind today. Our main goal is to understand the fundamental interactions between aromatic biomolecular building blocks and nature's most important solvent, at a molecular level. In addition, our comparison between benzene and hexafluorobenzene allows us to study the influence of charge distribution and quadrupole moments on structural and electronic properties of fully solvated aromatic systems.

II. METHOD

We have performed FPMD simulations [45, 46] of solvated benzene and hexafluorobenzene (HFB) under ambient pressure and temperature conditions. The simulations consist of 73 water molecules surrounding a benzene or HFB molecule in a periodically repeated cubic cell with a lateral dimension of 13.25 $\mathring{A}$, which in the case of benzene is based on the experimentally measured molar volume of the solute [47, 48]. The chosen size of the simulation box allows us to include the number of solvent molecules that are expected to be in the first and second solvation shells [30, 31].

All of our simulations were performed with the Car-Parrinello (CP) technique [49], which uses a Lagrangian that couples together the system's electronic and ionic degrees of freedom [50]. The electronic structure was described within density functional theory (DFT) [51, 52] with the PBE generalized gradient approximation (GGA) [53]. The valence wave functions and charge density were expanded in a plane wave basis, which was truncated in reciprocal space at 85 and 340 Ry, respectively. Norm-conserving pseudopotentials of the Hamman type were used to describe valence-core interactions [54, 55].

Since the geometry of water molecules is not expected to change significantly in the vicinity of the solute [25, 40] compared to its bulk values, we have utilized a rigid water model

[44]. In addition to our previous study of pure rigid water we have also successfully applied this model to a solvated cation (Ca^{2+}) [56], which gives us confidence in its suitability for the systems under consideration here. The use of a rigid water model permits the utilization of a larger fictitious mass in the CP dynamics, compared to flexible water and thus a larger MD timestep.

The initial configurations for our *ab initio* studies were obtained from 100 ps classical MD simulations performed with the TINKER package [57]. In order to reach a temperature of approximately 300 K we have initially applied a weakly-coupled velocity scaling thermostat for at least 3 ps before removing the thermostat and collecting statistics within the NVE ensemble.

Three independent simulations were performed for benzene, and one continuous trajectory was calculated for HFB. The total *ab initio* simulation times for solvated benzene and HFB were 152.1 ps and 103.5 ps respectively with average temperatures of 303.3 K and 299.1 K.

In addition to the 100 ps classical MD simulations that were used to obtain starting configurations, we have performed additional classical MD simulations to investigate the effects of simulation parameters such as size, time scales and symmetry operations. The GROMACS 3.2.1 code [58] with the OPLSAA force field [59] and the TIP4P model for water [60] was used to estimate realistic error bars by performing long time scale simulations of benzene solvated by 512 water molecules. This analysis will be presented in detail in a forthcoming publication [61].

A central point in our analysis is the investigation of the electronic structure of water around the solutes. To this end, we have calculated maximally localized Wannier functions (MLWF) for several hundred configurations along our MD trajectories. The MLWF were computed "on the fly" following a joint approximate diagonalization scheme [62]. Besides our analysis of the positions and spreads of the Wannier function centers (WFC) we have also used the procedure of Silvestrelli *et al.* [63] to compute an approximate dipole moment of each of the water molecules in the simulation.

III. RESULTS AND DISCUSSION

To test the accuracy of our theoretical approach we have performed binding energy calculations of the benzene-H_2O and HFB-H_2O dimers within the aforementioned theoretical

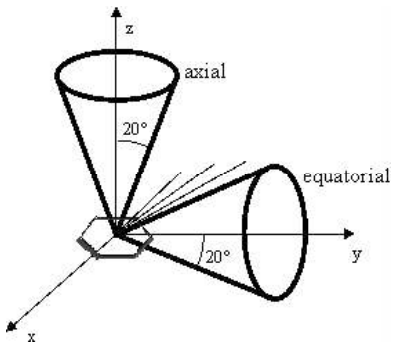

FIG. 1: Definition of the axial and equatorial region around benzene and hexafluorobenzene. The equatorial region extends from the center of the solute in all directions throughout the xy-plane.

framework of DFT/PBE. For these calculations the optimized geometries were determined with the limited memory method of Broyden-Fletcher-Goldfarb-Shanno (LBFGS) [64]. For benzene the distance from the center of the ring to the oxygen was found to have a very shallow minimum around 3.86 $\mathring{A}$, which considering the constrained intramolecular geometry that is enforced in our calculations, is in satisfactory agreement with previous quantum chemical studies (3.74 $\mathring{A}$) [42]. The preferred orientation of the optimized benzene-H_2O dimer exhibits one hydrogen atom of water pointing at the π-cloud, in good agreement with both experimental and theoretical studies.

Using the same plane wave cutoff as in our simulations (85 Ry) we obtained binding energies of -1.91 kcal/mol for benzene-H_2O and -1.13 kcal/mol for the HFB-H_2O dimer. Increasing the energy cutoff to 120 Ry did not result in significantly different binding energies. For benzene-H_2O our computed binding energy is consistent with quantum chemical results that have ranged from -1.50 kcal/mol to -2.90 kcal/mol depending on optimized geometry, and level of theory [12, 25, 28, 42, 65]. For HFB, previous studies also exhibit a range of binding energies from -1.55 kcal/mol to -2.69 kcal/mol [40–43], in satisfactory agreement with our calculations.

A. Radial distribution functions

A standard approach for describing the average structure of liquids and molecules in solution is to calculate the radial distribution function between atoms (RDF, or $g(r)$). Earlier

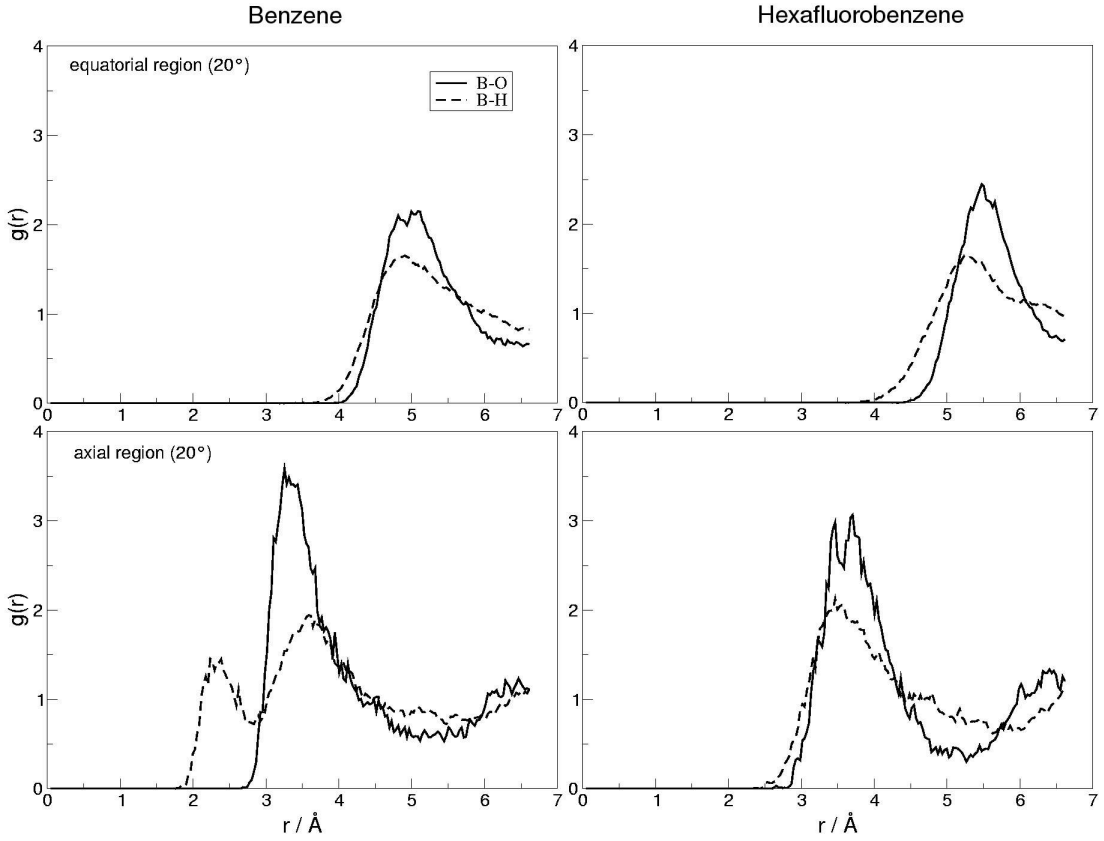

FIG. 2: Solute center-Oxygen (dashed lines) and solute center-Hydrogen (solid lines) radial distribution functions in the equatorial and axial regions (see Fig.1). The left column shows RDFs for benzene (B), the right column the RDFs for hexafluorobenzene (HFB).

works have examined this quantity by using the carbon atoms of benzene as the reference point, which leads to a rather featureless $g(r)$. Here, we have used the benzene/HFB ring center as reference point, which gives more structured RDFs and provides a clearer picture of the average structure of the liquid near the solute. The mirror plane symmetry of the solute molecule was exploited to improve statistics for all reported RDFs. We have also tested different bin sizes, Δr, from 0.01 to 0.09 $\mathring{A}$ to ensure independence of our reported RDFs from our discretization procedure. For all graphs shown in this section $\Delta r = 0.03$ $\mathring{A}$ has proven to be a suitable choice. We have also divided the space around the solute into an equatorial and an axial region, since these areas exhibit distinctively different interactions (see Fig. 1).

Figure 2 shows the average radial distribution of oxygen and hydrogen atoms in the

equatorial and axial region using the solute center as a reference point. Results for solvated benzene and HFB are shown in the left and right column, respectively. The top panels compare the distribution around both solutes in the equatorial region (20 degrees on both sides of the plane defined by the solute molecule) whereas the bottom panels show the axial region (20 degrees around the z-axis, defined perpendicular to the solute plane). $g_{B-O}(r)$ in the equatorial region around benzene (top left) shows slightly more structure than the corresponding $g_{B-H}(r)$ but both distributions are peaked around 4.9 $\mathring{A}$ with a similar onset located at 4.1 $\mathring{A}$ and 3.7 $\mathring{A}$, respectively. In contrast, the distributions calculated from the axial region show a strong qualitative difference when compared to each other. The axial $g_{B-H}(r)$ in Fig. 2 displays a double peak with maxima at 2.3 $\mathring{A}$ and 3.6 $\mathring{A}$, whereas the axial $g_{B-O}(r)$ shows only one distinct maximum at 3.3 $\mathring{A}$. The characteristic first $g_{B-H}(r)$-peak, located at smaller distances (by about 1 $\mathring{A}$) than the corresponding $g_{B-O}(r)$ peak, suggests that there is a strong orientational preference for the water molecules near the axial region of benzene.

A similar analysis for water molecules surrounding HFB in the equatorial region (top right in Fig. 2) shows $g_{HFB-O}(r)$ shifted outwards by approximately 0.6 $\mathring{A}$, with a peak at 5.5 $\mathring{A}$, and $g_{HFB-H}(r)$ with a similar onset but a maximum shifted by about 0.4 $\mathring{A}$ when compared to the B-water system. Steric effects cannot fully account for this shift of $g_{HFB-O}(r)$ and $g_{HFB-H}(r)$ in the equatorial region.

The two $g(r)s$ calculated from the axial region around HFB (bottom right in Fig. 2) are qualitatively different from those obtained for the benzene-water system. Only one H-peak appears at 3.5 $\mathring{A}$ corresponding to the $g_{HFB-O}(r)$ peak centered at 3.6 $\mathring{A}$. The similar onset and shape of both distributions in Fig. 2 suggest that any possible orientational effects on the faces of HFB must be of a different nature than in the case of water on the faces of benzene. This will be further discussed in Section III.C. In the case of benzene, the axial g_{B-H}-double peak points at an orientation where the two hydrogen molecules of water are located at different distances from the solute center. Comparing peak positions in the axial regions to the optimized dimer geometries we notice that in the case of both benzene and HFB the condensed phase values for the solute center-oxygen distances are significantly smaller than in the gas phase. For both benzene and HFB, the overall structure of the water as described by the $g_{O-O}(r)$, $g_{O-H}(r)$ and $g_{H-H}(r)$ distribution functions (not shown) are very similar to those of pure water as described within the rigid approximation [44].

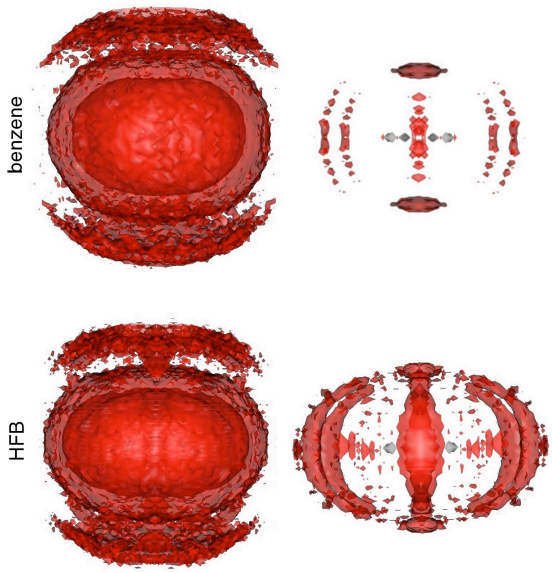

FIG. 3: Spatial distribution function (shown in red) of oxygen around benzene (upper panel) and HFB (lower panel) illustrating the spheroidal shape (isosurface 1) on the left and the cage-like structure in the equatorial region of the first shell and the high concentration at the faces (isosurface 2.6) on the right. The spatial distribution of carbon is shown in grey. Due to the spheroidal shape of the second solvation shell compared to the cubic shape of the simulation box, the second shell is not fully represented within the MD cell.

B. Spatial distribution functions

In order to gain a better understanding of the three-dimensional local solvation structure, we have calculated spatial distribution functions (SDF) [66] of oxygen and hydrogen around benzene and HFB. Normalization of all SDF data has been performed with respect to the experimental bulk water density at ambient conditions. A common problem when trying to resolve solvation details around hydrophobic solutes is the long simulation time required to gather sufficient statistical data on spatial distributions [67]. We have overcome this difficulty by using the rigid water approximation, thus extending the timescales accessible by *ab initio* MD by a factor of three [44], and by exploiting all symmetry operations of the solute, so as to obtain sufficiently smooth SDF. To verify that no bias is introduced into our data by these symmetry operations, we have tested our SDF analysis on random distributions and large classical MD data sets [61].

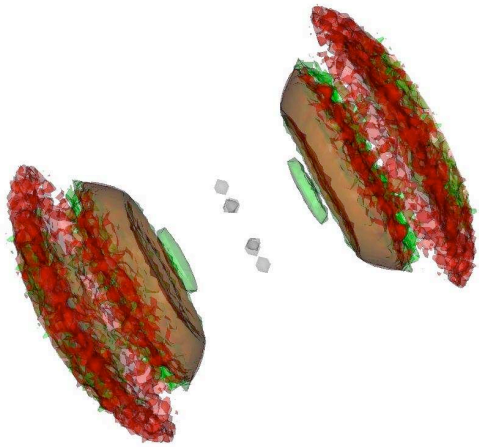

FIG. 4: Combination of spatial distribution functions (isosurface 1) of oxygen and hydrogen around benzene in the axial region (45 degrees from z-axis). Oxygen is shown in red, hydrogen in green and carbon in grey. In addition to the first and second solvation shell, a region of hydrogen density much closer to the benzene center is visible. The corresponding SDF for HFB looks almost identical except for the absence of this hydrogen density region.

Figure 3 shows the distribution of oxygen (red) around benzene (top) and HFB (bottom) for two different isosurfaces. The SDFs on the left illustrate the spheroidal shape of the first solvation shell and part of the second, whereas the right pictures show the distinct structures in the axial and equatorial region, which dominate within the first solvation shell. The cage-like oxygen density in the equatorial region around benzene (top right) is located in between the hydrogens of benzene and exhibits maxima in the equatorial plane (compare to Fig. 5). The axial region is characterized by a rather broad maximum of oxygen density around the C_6-symmetry axis of the molecule. Upon close inspection this axial oxygen density is found to have a torus-like shape.

The corresponding SDFs for hydrogen around benzene show a similar albeit less pronounced density in the equatorial region, and a clearly different distribution in the axial region. Figure 4 illustrates this difference between oxygen and hydrogen density distribution by showing both densities at an isosurface level of 1 for a 90 degree axial cone. Clearly visible are the two solvation shells with an additional region of hydrogen density much closer to the solute, which gives rise to the first hydrogen peak in the bottom left panel of Figure

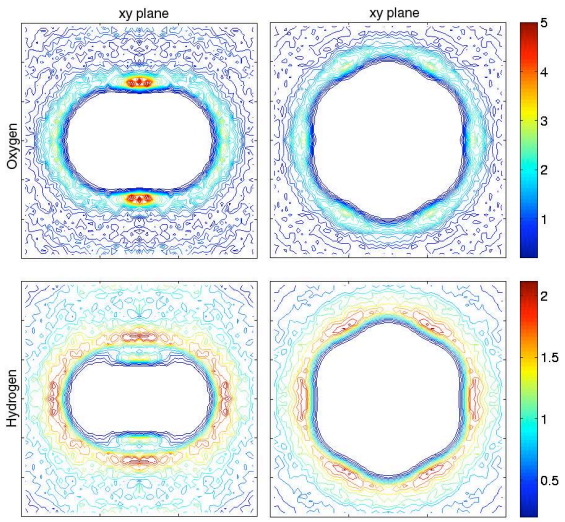

FIG. 5: Contour planes (yz and xy) through the oxygen- and hydrogen-spatial distribution functions (SDFs) of benzene

2.

Another, more quantitative analysis of this data is shown in Figure 5. Plots of the yz and xy contour planes depict more pronounced oxygen SDFs in both regions, and a specific hydrogen density closer to the solute than the first solvation shell.

Analogous contour plots for oxygen and hydrogen densities around HFB (Fig. 6) show several differences. In the equatorial region, oxygen shows higher densities and enhanced localization, i.e. a stronger cage-like structure. The hydrogen SDF contour plots show similar density values in the equatorial region but a somewhat broader spatial extension in the equatorial plane. Also, the equatorial extension of the solute cavity appears bigger, in part as a result of steric effects due to the fluorine atoms. In the axial region, a much more localized oxygen density and the total absence of the specific hydrogen density found for benzene are remarkable. In particular, the distribution of hydrogen atoms forms a broad disk on the faces. A direct comparison is drawn in Figure 7 where a top view of the oxygen SDFs of solvated benzene and HFB are shown for the same isosurface.

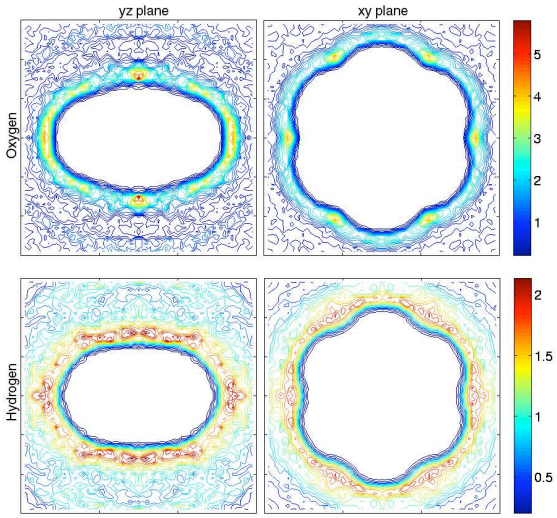

FIG. 6: Contour planes (yz and xy) through the Oxygen- and Hydrogen-SDFs of HFB.

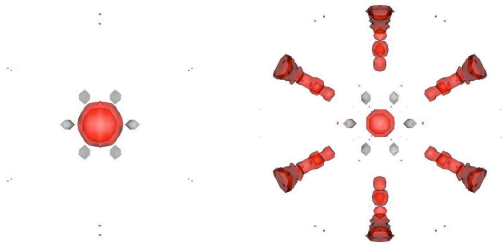

FIG. 7: Top view of the spatial distribution function of oxygen around benzene (left) and HFB (right) for an isosurface of 3. Oxygen is shown in red, carbon atoms in grey, hydrogen and fluorine are not shown.

C. Angular distribution functions and preferred orientations

The analysis of RDFs and SDFs has indicated that preferred orientations of water exist around benzene and possibly around HFB, particularly in the axial region. In this section, the orientations of water molecules are investigated depending on their position relative to the solute by calculating the tilt angles of individual H_2O molecules. As shown by Grossman *et al.* a first principles description is needed to accurately resolve angular preferences of solvent molecules around small hydrophobic molecules [68]. Again, the mirror symmetry of the solute has been exploited to improve statistics. A graphic definition of the polar angle and the tilt angle is given in Fig. 8.

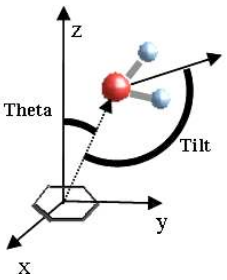

FIG. 8: Definition of the water tilt angle used throughout this study (see text).

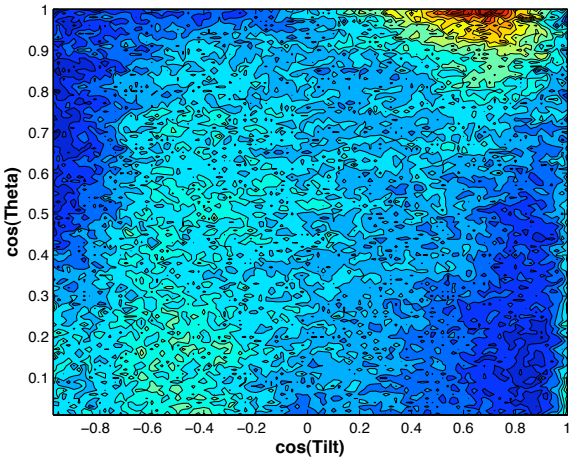

FIG. 9: Cosine of the tilt angle of water molecules surrounding benzene up to a distance of 6.6 angstrom versus the polar angle Theta measured from the C_6 axis of the solute. The color map is scaled relative to the maximum.

For benzene, the tilt angle distribution (Figure 9) shows a strong maximum axially at a tilt angle of $\sim 46\,^\circ$ and a much weaker, rather broad distribution in the equatorial region around $121\,^\circ$. While the characteristic orientation in the axial region is concentrated in a very small region around the C_6-axis (i.e. around the maxima in the axial oxygen and hydrogen SDF, see Fig. 5) the equatorial orientation stretches much further and appears to be the preferred underlying orientation of water around these hydrophobic solutes, locally disrupted by a specific interaction of water on the faces. HFB yields a different picture in the axial region with a less pronounced maximum at $\sim 123\,^\circ$ and again a very broad maximum in the equatorial region roughly around $115\,^\circ$ (Note that the colors in Fig. 9 and 10 are scaled relative to their respective maxima). This preferred orientation of approximately $120\,^\circ$, which has also been found in a classical MD study of benzene and cyclohexane [37] and in

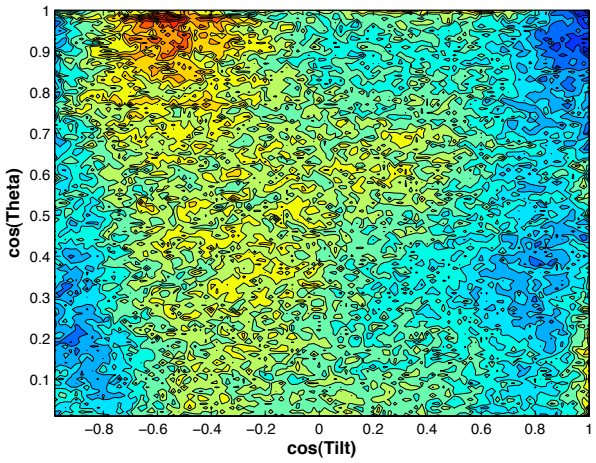

FIG. 10: Cosine of the tilt angle of water molecules surrounding HFB up to a distance of 6.6 angstrom versus the polar angle Theta measured from the C_6 axis of the solute.

a first principles study of solvated methane and silane [68], appears to be a characteristic feature of water near small hydrophobic solutes. We also note that a smaller peak exists at $\cos(tilt) = 1$ for both solutes representing small tilt angles. This has also been observed for other small hydrophobic molecules and was shown to arise from solvent molecules in the outer parts of the first solvation shell, whereas the dominant equatorial peak at $\sim 120\,^\circ$ comes from molecules closest to the solute [68, 69].

If one assumes that water tilt angles of $\sim 120\,^\circ$ are characteristic of hydrophobic hydration of small apolar solutes, then Figures 9 and 10 nicely show why both molecules (benzene in particular) can be considered "atypical" hydrophobic solutes. While they show many characteristic properties, e.g. a large positive hydration heat capacity [70], both solutes bind weakly to water molecules in the axial region leading to preferred orientations (i.e. the two dominant peaks in the axial region in Figures 9 and 10) which differ significantly from those commonly found around small hydrophobic solutes. While Figure 10 might suggest that HFB differs less from a normal hydrophobic solute than benzene, this is only true insofar as the axial interaction with H_2O is weaker. Still fully solvated HFB leads to different orientational preferences of water molecules in the axial region than expected around small apolar solutes, and this can be traced back to a distinct π-lone pair interaction.

Figure 11 shows a cartoon illustrating the two dominant orientations of water on the faces of benzene and HFB. Whereas the orientation of water on the faces of benzene is similar to

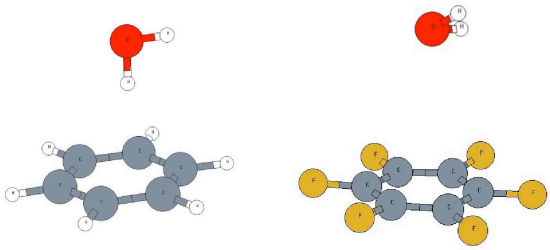

FIG. 11: Characteristic orientation of water molecules bound to benzene and HFB.

the optimized gas phase dimer (although the B-O distance is different), solvent molecules on the faces of HFB show a much smaller tilt angle than in the gas phase. Our geometry optimization as well as quantum chemical studies [42] have shown that the optimized HFB-water dimer displays a tilt angle of 180 °, i.e. oxygen pointing directly into the π-electron system. Despite this clear orientational preference in the axial region of both solutes, it is important to note that a high degree of freedom remains for the solvent molecules since a rotation around the C_6-axis of benzene will not change the preferred tilt angle. The broad hydrogen SDF in Figure 4 is a manifestation of this nonrigidity.

It is interesting to note that a recent computational study, which used classical potentials and Monte-Carlo simulations, to investigate orientational effects in the benzene-water interfacial region [71] found that water molecules in the interface close to the apolar phase prefer to point one O-H bond towards the benzene phase, whereas water molecules on the aqueous side of the interface prefer to orient parallel to the interfacial plane. benzene generally showed a preference to orient its plane parallel to the interface. The observed orientational preferences, although weaker at higher temperatures, and the radius of the first solvation shell were shown to be qualitatively independent of the thermodynamic conditions. These results agree qualitatively with the data presented here and highlight the importance of the environment on the relative orientation of benzene and water to each other.

D. Electronic properties

One of the strengths of *ab initio* MD simulations comes from the inclusion of the electronic structure of the system at each step, including properties such as charge densities, charge

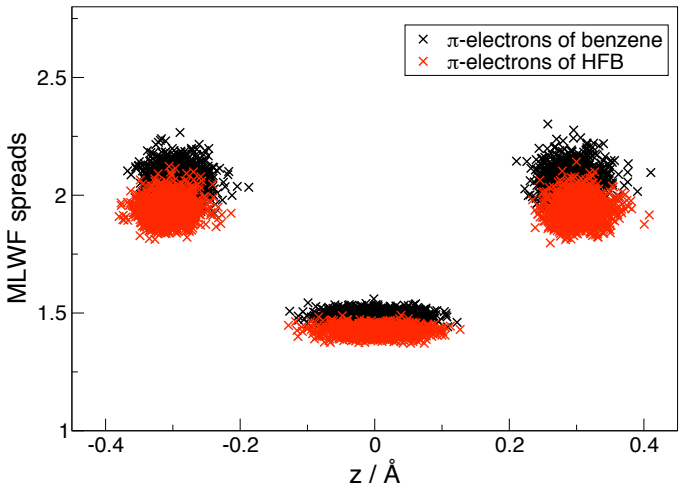

FIG. 12: Spreads of the MLWFs belonging to the σ- and the π-electrons and the distance (denoted as z) of their Wannier function centers from the plane defined by the solutes (fitted through the 6 C-atoms).

transfer and dipole moments. In the following section we investigate the differences between benzene and HFB in terms of their electronic structure and the peculiarities of the bonds established on the faces of benzene and HFB.

1. MLWF analysis

After investigating details of the solvent structure and orientation, we analyzed the changes in electronic structure of the solutes and the solvent during our MD simulations in order to better understand the nature of their interactions. Maximally localized Wannier functions (MLWF) offer an intuitive view of chemical bonds in condensed phases and an efficient way to explore the changes in electronic structure along MD trajectories [62]. Within the commonly used pseudopotential approximation there are four doubly occupied MLWF for each water molecule, 15 for benzene (6 localized on the C-H bonds and 9 for the π-electron system) and 33 for HFB (18 localized on F atoms, 6 localized on the C-F bonds and 9 for the π-electron system).

First, we compare the π-electrons of benzene and HFB in terms of their spreads and their center's distance (WFC) from the molecule's plane. In the case of a delocalized π-electron system, the MLWFs resemble a series of single and double bonds, analogous to the classic Kekule representation. Figure 12 shows that the π-electrons of HFB exhibit a

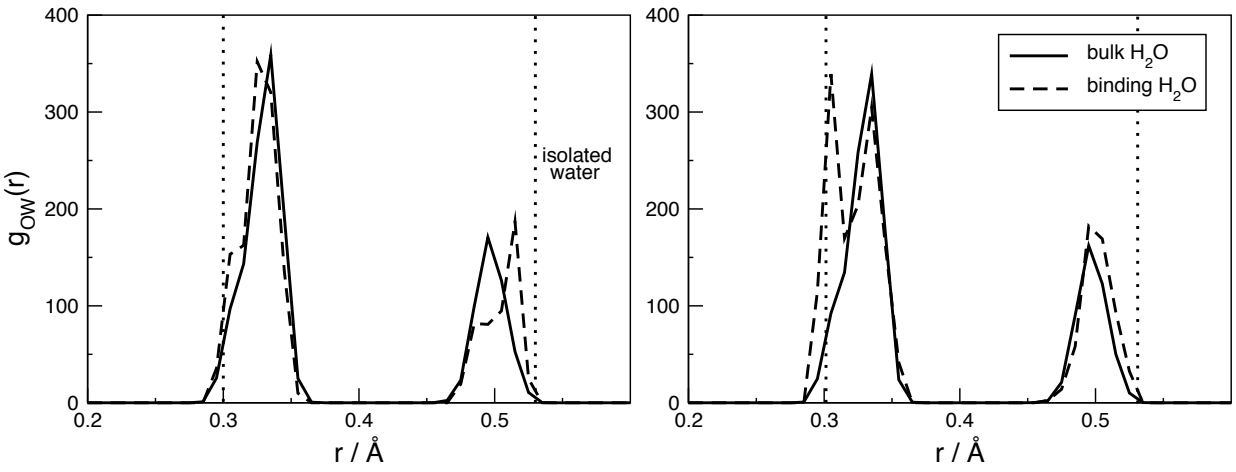

FIG. 13: Oxygen - WFC radial distribution function for water molecules binding to the π-electron system of benzene (left) and HFB (right) compared to H_2O molecules in the bulk. Dotted lines represent the O-W distance for an isolated water molecule.

stronger localization both in terms of their MLWF spreads and WFC position; this can be understood in terms of the strong electronegativity of fluorine atoms. The effects of fluorination on the interaction of benzene dimer compounds has also been studied recently [72]. As expected, the substitution of fluorine onto the benzene molecule diminishes the partial negative character of the π-cloud above the ring and ultimately leads to a quadrupole moment which is similar in strength but opposite in sign. In Fig. 11 we have identified the predominant orientation of water molecules that interact with the faces of benzene. We now analyze the corresponding changes that occur in the electronic structure of these interfacial H_2O molecules. To shed light on the nature of this specific interaction which "binds" one H_2O to the π-electron system of benzene and, to a lesser extent, to that of HFB we have compared the Wannier function centers (WFC) of binding H_2O molecules to those of bulk water molecules.

Figure 13 shows the oxygen-Wannier function center RDF, denoted as $g_{OW}(r)$, of the interacting H_2O molecule (dashed line) on the faces of benzene (left) and HFB (right) as well as the $g_{OW}(r)$ of bulk water (solid line) for comparison. The reference curves of bulk water display two main peaks. The stronger peak at r$\sim$0.33 Å corresponds to the two oxygen lone pairs on each of the water molecules, whereas the smaller one centered at r$\sim$0.49 Å comes from the $O-H$ covalent bonds. The gas phase values are denoted as dotted lines. Comparing the reference distribution with $g_{OW}(r)$ of the binding H_2O molecules on the faces

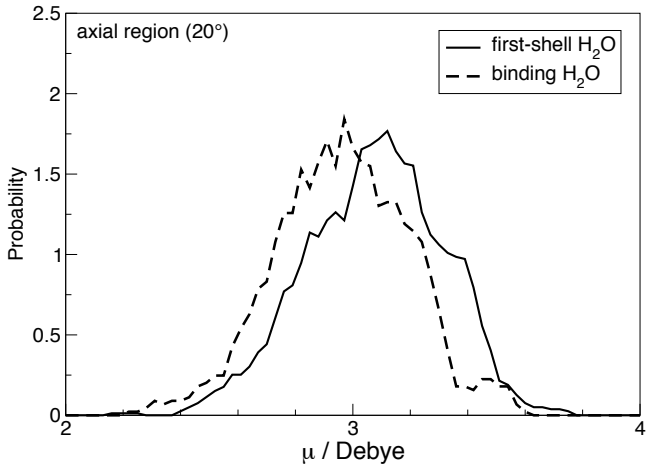

FIG. 14: Calculated dipole moments of water in the axial region around benzene for two different radius intervals capturing the binding water molecules and the bulk water in the axial direction.

of benzene (left graph in Fig. 13) a strong shift of one binding $O-H$ orbital centers towards the gas phase value can be observed. In terms of conventional H-bonds Figure 13, suggests that the H_2O molecule donates a weak H-bond to the π-electron system of benzene.

For HFB (right graph in Fig. 13) the binding water molecules also yield a different $g_{OW}(r)$ than the reference bulk data, but in this case one of the lone pairs is affected, with its WFC shifted considerably closer to oxygen, essentially assuming its gas phase value. This corresponds to the picture of a broken H-bond acceptor. We have also compared the dipole moments of the "binding" water molecules on the faces of benzene to those of all other water molecules in the axial region. The dipole moments are calculated in an approximative manner from static configurations by assigning the total charge of the MLWF to a point charge at its center [63]. Figure 14 shows the dipole moment distribution of "binding" H_2O molecules compared to that of other axial first shell water molecules around benzene. Most notably the π-hydrogen interaction leads to a decrease in dipole moments by about 0.15 Debye, from 3.10 to 2.95 Debye. This behavior brings into question the suitability of classical non-polarizable water models for MD simulations of solvated benzene [61].

2. Total charge density

Another qualitative view on the changes in electronic structure caused by fluorination and upon binding to solvent molecules can be obtained by comparing the total charge densities

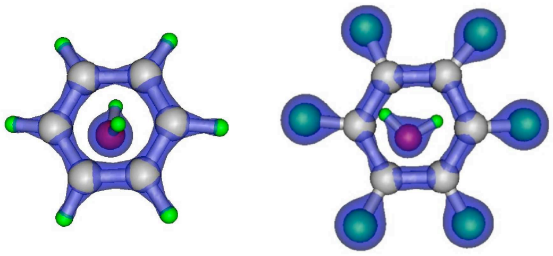

FIG. 15: Total charge density plots for the unoptimized benzene-water and HFB-water dimer. Close inspection reveals the more localized charge distribution in the π-electron system of HFB which is a result of the electron-withdrawing fluorine atoms.

of benzene-water and HFB-water dimers. These unoptimized dimers were cut out during the simulation from the full simulation cell and exhibit characteristic binding orientations (which were also shown in Fig. 11). Figure 15 shows the slightly more localized charge density in the π-electron region of HFB caused by the substitution of fluorine (similar to Fig. 12). It is important to note that in our electronic structure calculations utilizing pseudopotentials one electron for hydrogen is treated explicitly but four for each fluorine atom.

As noted earlier, fluorine substitution withdraws charge from the π-electron system leading to a more localized charge distribution in the π-plane and increases the partial charge on the fluorine atoms of HFB compared to the hydrogen atoms on benzene [72, 73].

Despite its usefulness for gaining a better understanding of the overall electronic structure of the dimers the total charge density does not clearly illustrate the subtle changes in electronic structure that occur upon formation of the respective dimers. Charge density difference plots of the benzene-water and HFB-water dimers point out regions with increased or decreased charge density compared to isolated solute and solvent molecules. We have also calculated charge density difference plots of the whole simulation cell, however, for clarity the results for the dimer are shown since it better allows one to inspect the important changes visually.

Figure 16 illustrates the transfer of charge from the π-system towards the hydrogen atom of H_2O which points at the face of benzene and a loss of charge at the H atom accordingly. An opposite but smaller effect is found in the case of HFB where the π-system facing the water molecule shows charge depletion and the closest lone pair extends further, showing additional charge density closer to the π-system. A type of π-lone pair interaction in the

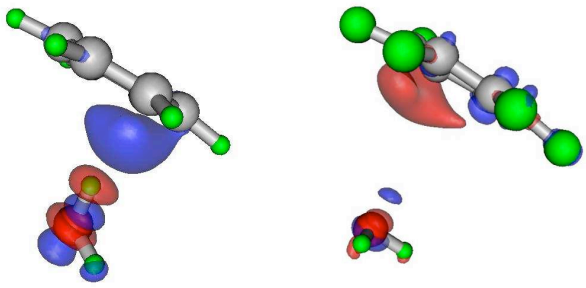

FIG. 16: A qualitative comparison of charge density differences for the unoptimized benzene-water (left) and HFB-water dimer (right). Red indicates areas where the combined system contains less charge, blue where the charge density of the combined system is higher.

case of solvated HFB can be inferred from this analysis. The same type of interaction but in a qualitatively different orientation has been observed for the gas phase HFB-water dimer where both lone pairs symmetrically point towards the π-system.

Note that the charge density of an isolated (gas phase) water molecule is subtracted from the dimer and not the charge density of a bulk water molecule. Therefore, the charge density difference around water pointed out in Figure 16 refers to a gas phase H_2O as a reference and not a bulk molecule (like previous comparisons in this chapter). The picture obtained from charge density difference plots here is consistent with Figure 13, which compares only the WFC of binding and bulk water molecules. But while the lone pair distribution of water around HFB in Figure 13 suggests a broken H-bond, the analysis here shows that there is a notable transfer of charge towards the π-system although small compared to the case of benzene.

IV. CONCLUSION

In summary, we have reported the results of extensive *ab initio* simulations aimed at a microscopic description of the hydration structure of benzene and HFB. Our study represents the first investigation of these solutes in liquid water, obtained from first principles. Benzene and HFB are prototypical examples of solvated aromatic molecules that exhibit π-hydrogen and π-lone pair interactions, respectively. We have shown that both benzene and HFB are composed of two distinct regions: one equatorial and the other axial. The former behaves

like an ordinary hydrophobic solute in the two aromatic molecules, although the cage-like structure shown in spatial distribution functions and characteristic of hydrophobic solutes is more pronounced in HFB than in benzene. The solvation of the axial region depends on how the π-electrons of the solute interact with interfacial water molecules. The axial region of benzene acts like an acceptor and forms a weak hydrogen bond with water (as shown, e.g. by our MLWF analysis), while HFB acts as a much weaker donor interacting with an oxygen lone pair. This specific behavior leads to different orientations of water on the faces of these solutes. The preferential tilt angle of water in the equatorial regions is about 120° for both benzene and HFB, while in the axial regions there is a strong preference for $\sim 46°$ in benzene and $\sim 123°$ in HFB. It is interesting to note that while the preferred orientation of water on the face of benzene is very similar in the gas-phase dimer and in liquid water, in the case of HFB the orientations found in the gas phase and in the liquid differ substantially. A similar difference in tilt angle distributions was found in recent cation solvation studies of Mg^{2+} and Ca^{2+} [56, 74].

The electronic structure of interfacial water molecules differs from that of bulk water, as a result of the interaction with the aromatic solute. In particular, we have found a decrease of the dipole moment by approximately 0.1 Debye in interfacial water molecules. These results indicate that the solvation of aromatic species is determined by subtle but important charge transfer and dipole redistributions effects, and cast some doubts on the validity of non-polarizable models for the study of these systems. Our findings also indicate that electronic structure information, as contained in *ab initio* MD simulations, is an important component in a microscopic description of aromatic hydration.

The authors would like to thank G.Cicero for many useful discussions. M.Allesch was supported by a DOC fellowship of the Austrian Academy of Sciences. This work was performed under the auspices of the U.S. Dept. of Energy at the University of California/Lawrence Livermore National Laboratory under contract no. W-7405-Eng-48.

---

[1] J. M. Sorenson, J. M. Gregory, and D. C. Clary, J. Chem. Phys. **106**, 849 (1997).

[2] B.-M. Cheng, J. R. Grover, and E. A. Walters, Chemical Physics Letters **232**, 364 (1995).

[3] J. Vrbancich and G. L. D. Ritchie, J. Chem. Soc., Faraday Trans.2 **76**, 648 (1980).

[4] P. I. Nagy, C. W. U. II, and D. A. Smith, J. Chem. Phys. **102**, 6812 (1995).

[5] I. Alkorta, I. Rozas, and J. Elguero, Chemical Society Reviews **27**, 163 (1998).

[6] G. Desiraju and T. Steiner, *The weak Hydrogen Bond* (Oxford University Press, Oxford, 2001).

[7] O. Hübner, A. Glöss, M. Fichtner, and W. Klopper, J.Phys. Chem. A **108**, 3019 (2004).

[8] K. S. Kim, P. Tarakeshwar, and J. Y. Lee, Chem. Rev. **100**, 4145 (2000).

[9] W. H. Thompson and J. R. Snyder, J. Chem. Eng. Data **9**, 516 (1964).

[10] J. F. Connolly, J. Chem. Eng. Data **11**, 13 (1966).

[11] Z. Alwani and G. Schneider, Ber. Bunsen-Ges. Phys. Chem. **71**, 633 (1967).

[12] S. Suzuki *et al.*, Science **257**, 942 (1992).

[13] M. Nakahara, C. Wakai, Y. Yoshimoto, and N. Matubayashi, J. Phys. Chem. **100**, 1345 (1996).

[14] T. S. Zwier, Annu. Rev. Phys. Chem. **47**, 205 (1996).

[15] S. Furutaka and S. ichi Ikawa, The Journal of Chemical Physics **108**, 5159 (1998).

[16] S. Furutaka and S. ichi Ikawa, The Journal of Chemical Physics **108**, 1347 (1998).

[17] S. Furutaka and S. ichi Ikawa, The Journal of Chemical Physics **113**, 1942 (2000).

[18] S. Furutaka and S. Ikawa, J. Chem. Phys. **117**, 751 (2002).

[19] R. Bruant and M. Conklin, Journal of Physical Chemistry B **104**, 11146 (2000).

[20] Y. Jin and S. ichi Ikawa, The Journal of Chemical Physics **122**, 024509 (2005).

[21] C. J. Gruenloh *et al.*, Science **276**, 1678 (1997).

[22] C. J. Gruenloh *et al.*, J. Chem. Phys. **113**, 2290 (2000).

[23] C. J. Gruenloh *et al.*, J. Chem. Phys. **109**, 6601 (1998).

[24] J. Y. Lee *et al.*, J. Chem. Phys. **113**, 6160 (2000).

[25] D. Feller, J. Phys. Chem. A **103**, 7558 (1999).

[26] J. Augspurger, C. E. Dykstra, and T. S. Zwier, J. Phys. Chem. **96**, 7252 (1992).

[27] S. Y. Fredericks, K. D. Jordan, and T. S. Zwier, J. Phys. Chem. **100**, 7810 (1996).

[28] D. M. Upadhyay and P. C. Mishra, J. Mol. Structure (Theochem) **584**, 113 (2002).

[29] G. Ravishanker, P. K. Mehrotra, M. Mezei, and D. L. Beveridge, J. Am. Chem. Soc. **106**, 4102 (1984).

[30] P. Linse, G. Karlström, and B. Jnsson, J. Am. Chem. Soc. **106**, 4096 (1984).

[31] P. Linse, J. Am. Chem. Soc. **112**, 1744 (1990).

[32] W. L. Jorgensen and D. L. Severance, J. Am. Chem. Soc. **112**, 4768 (1990).

[33] S. Urahata, K. Coutinho, and S. Canuto, Chem. Phys. Lett. **274**, 269 (1997).

[34] S. Urahata and S. Canuto, Chem. Phys. Lett. **313**, 235 (1999).

[35] A. Laaksonen, P. Stilbs, and R. E. Wasylishen, J. Chem. Phys. **108**, 455 (1998).

[36] T. M. Raschke and M. Levitt, J. Phys. Chem. B **108**, 13492 (2004).

[37] T. M. Raschke and M. Levitt, PNAS **102**, 6777 (2005).

[38] P. Schravendijk and N. F. A. van der Vegt, J. Chem. Theory Comput. **1**, 643 (2005).

[39] M. Besnard, Y. Danten, and T. Tassaing, J. Chem. Phys. **113**, 3741 (2000).

[40] Y. Danten, T. Tassaing, and M. Besnard, J. Phys. Chem. A **103**, 3530 (1999).

[41] I. Alkorta, I. Rozas, M. L. Jimeno, and J. Elguero, Structural Chemistry **12**, 459 (2001).

[42] M. Raimondi *et al.*, J. Phys. Chem. A **107**, 772 (2003).

[43] J. P. Gallivan and D. A. Dougherty, Organic Letters **1**, 103 (1999).

[44] M. Allesch, E. Schwegler, F. Gygi, and G. Galli, J. Chem. Phys. **120**, 5192 (2004).

[45] F. Gygi, *GP 1.24.0: A general ab initio molecular dynamics program*, Lawrence Livermore National Laboratory, 2003.

[46] F. Gygi, *The Qbox code*, Lawrence Livermore National Laboratory, 2005.

[47] M. K. Dutta-Choudhury, N. Miljevic, and W. A. van Hook, J. Phys. Chem. **86**, 1711 (1982).

[48] E. E. Tucker and S. D. Christian, J. Chem. Phys. **83**, 426 (1979).

[49] R. Car and M. Parrinello, Phys. Rev. Lett. **55**, 2471 (1985).

[50] G. Galli and M. Parrinello, in *Computer Simulation in Materials Science*, edited by M. Meyer and V. Pontikis (Kluwer Academic Publishers, Netherlands, 1991), pp. 283–304.

[51] P. Hohenberg and W. Kohn, Phys. Rev. B **136**, 864 (1964).

[52] W. Kohn and L. J. Sham, Phys. Rev. A **140**, 1133 (1965).

[53] J. P. Perdew, K. Burke, and M. Ernzerhof, Phys. Rev. Lett. **80**, 891 (1998).

[54] D. R. Hamann, Phys. Rev. B **40**, 2980 (1989).

[55] L. Kleinman and D. M. Bylander, Phys. Rev. Lett. **48**, 1425 (1982).

[56] F. C. Lightstone *et al.*, ChemPhysChem **6**, 1745 (2005).

[57] *TINKER - Software Tools for Molecular Design, Version 3.9.*

[58] E. Lindahl, B. Hess, and D. van der Spoel, J. Mol. Mod **7**, 306 (2001).

[59] G. Kaminski, E. Duffy, T. Matsui, and W. Jorgensen, J. Phys. Chem. **98**, 13077 (1994).

[60] W. L. Jorgensen and J. D. Madura, Mol. Phys. **56**, 1381 (1985).

[61] M. Allesch, F. C. Lightstone, E. Schwegler, and G. Galli, in preparation, 2006.

[62] F. Gygi, J.-L. Fattebert, and E. Schwegler, Computer Physics Communications **155**, 1 (2003).

[63] P. L. Silvestrelli and M. Parrinello, Phys. Rev. Lett. **82**, 3308 (1999).

[64] D. C. Liu and J. Nocedal, Math. Programming **45**, 503 (1989).

[65] A. Courty *et al.*, J. Phys. Chem. A **102**, 6590 (1998).

[66] I. M. Svishchev, A. Y. Zassetsky, and P. G. Kusalik, Chemical Physics **258**, 181 (2000).

[67] J. C. Grossman *et al.*, J. Chem. Phys. **120**, 300 (2004).

[68] J. C. Grossman, E. Schwegler, and G. Galli, J. Phys. Chem. B **108**, 15865 (2004).

[69] C. A. Koh *et al.*, J. Chem. Phys. **113**, 6390 (2000).

[70] G. Hummer, S. Garde, A. Garcia, and L. Pratt, Chemical Physics **258**, 349 (2000).

[71] A. Kereszturi and P. Jedlovszky, J. Chem. Phys. B **109**, 16782 (2005).

[72] K. Riley and K. M. Merz, J. Phys. Chem. B **109**, 17752 (2005).

[73] P. W. Fowler and E. Steiner, J. Phys. Chem. **101**, 1409 (1997).

[74] F. C. Lightstone *et al.*, Chem. Phys. Lett. **343**, 549 (2001).

LAWRENCE
LIVERMORE
NATIONAL
LABORATORY

UCRL-JRNL-234592

First Principals & Classic Molecular Dynamics Simulation/Solvated Benzene

M. Allesch, F. Lightstone, E. Schwegler, G. Galli

September 13, 2007

Journal of Chemical Physics

First principles and classical molecular dynamics simulations of solvated benzene

Markus Allesch,[1,2] Felice C. Lightstone,[2] Eric Schwegler,[2] and Giulia Galli[2,3]

[1]*Department of Theoretical and Computational Physics, Graz University of Technology, Austria*

[2]*Lawrence Livermore National Laboratory, 7000 East Ave., Livermore, CA 94550*

[3]*University of California, Davis, CA 95616*

(Dated: October 15, 2007)

Abstract

We have performed extensive *ab initio* and classical MD simulations of benzene in water in order to examine the unique solvation structures that are formed. Qualitative differences between classical and *ab initio* MD simulations are found and the importance of various technical simulation parameters is examined. Our comparison indicates that non-polarizable classical models are not capable of describing the solute-water interface correctly if local interactions become energetically comparable to water hydrogen bonds. In addition, a comparison is made between a rigid water model and fully flexible water within *ab initio* MD simulations which shows that both models agree qualitatively for this challenging system.

I. INTRODUCTION

The accurate description of the interaction between hydrophobic solutes and interfaces with water play a key role in understanding many different processes, such as protein folding and stability[1]. However, the description of these complex interfacial systems has proven to be particularly difficult since properties cannot be simply extrapolated from the bulk and the behavior at the interface strongly depends on subtle details of the solute-solvent interaction and external conditions[2].

For the different types of MD simulation techniques developed over the last decades the hydrophobic hydration of benzene (B) represents a challenging test case. It can serve as a model for many biological systems containing delocalized π-electron systems, it is a small enough system for extensive *ab initio* simulations and it contains two distinct regions that interact differently with water[3]. Solvated benzene also has significantly different properties than comparable solvated aliphatic hydrocarbons (e.g. a much higher solubility) and has been the subject of several computational studies using classical MD techniques[4–14]. Most recently two studies of solvated benzene based on empirical potentials[12,13] showed qualitative differences for computed radial distribution functions, one of the basic properties that is usually employed to compare empirical potentials with experimental results. These two sets of classical simulations used different empirical models for water and for benzene leading to a qualitatively different description of the weak π-hydrogen bond which is characteristic for this system[15]. Since this important feature contributes significantly to the special solvation properties of benzene[13] and also occurs in many other biological systems, it deems necessary to resolve these existing discrepancies between MD simulations and to obtain an accurate description of this system by systematically investigating the different methods and approximations used.

In a previous study dealing with the hydrophobic hydration of benzene, the structural and electronic properties of solvated benzene were examined with a rigid water model in *ab initio* MD simulations[3]. Figure 1 gives an overview of the hydrophobic solvation of benzene by showing spatial distribution functions (SDF) of oxygen for two different isosurfaces (1 and 2.6). Clearly visible are the first and parts of the second solvation shell in the left graph. At a higher level of the isosuface, cage-like solvation structures can be seen around the equatorial region, which closely resembles other small hydrophobic solutes[16]. In contrast,

due to the formation of weak π-hydrogen bonds, distinct disk-like distributions are found near the axial regions of the solute.

These results for benzene have been compared with analogous data for solvated hexafluorobenzene (HFB) to highlight the different nature of the solvent interaction with the π-electron systems. Due to a reversed quadrupole moment, it was found that solvated HFB prefers a π-lone pair interaction with water in the axial region, whereas benzene displays a weak π-hydrogen bond. In both cases, the equatorial regions around the aromatic molecules behaves like an ordinary hydrophobic solute leading to the typical water tilt angle of about 120°.

In this study we have continued to examine the solvation properties of benzene in water by carrying out an *ab initio* MD simulation using fully flexible water molecules and extensive classical MD simulations. The comparison and evaluation of these different types of simulation methods and the approximations contained within are the main goal of the present study.

The rest of the paper is structured as follows: First we compare the structural properties obtained from two sets of *ab initio* simulations using rigid and flexible water models. In section III.B we contrast these results with analogous data obtained from extensive classical MD simulations. Finally, we investigate the role of several technical simulation parameters which could be responsible, in part, for some of the observed differences between results from different MD methods.

II. METHOD

A. *Ab initio* MD technique

Our *ab initio* MD simulations[17,18] of solvated benzene are based on electronic structure calculations within density functional theory (DFT)[19,20] utilizing the PBE generalized gradient approximation (GGA)[21]. Plane wave basis sets were used to represent the valence wavefunctions and charge density and were truncated in reciprocal space at 85 and 340 Ry, respectively. Valence-core interactions were described by Hamann type norm-conserving pseudopotentials[22,23]. We note that binding energy calculations for the benzene-water dimer at this level of theory yield good agreement compared with quantum chemical studies[3].

All of our *ab initio* simulations consisted of 73 water molecules surrounding a benzene molecule in a cubic cell with a lateral dimension of 13.25 Å and periodic boundary conditions. The system included the first and most of the second solvation cell at a density of 0.994 g/cc and ambient pressure and temperature conditions. A weakly coupled velocity scaling thermostat was initially used as previously described[3] before statistics were collected within the NVE ensemble. The total simulation times and parameters of all MD simulations are reported in Table I.

The propagation of electrons and ionic cores in the simulations was performed following the Car-Parrinello (CP) technique, which is based on the use of a Lagrangian that couples together the system's electronic and ionic degrees of freedom[24,25]. A central parameter in the CP scheme is the fictitious electron mass, μ, which has to be chosen very carefully to avoid overlapping of ionic and electronic degrees of freedom and ensure adiabaticity[26,27]. If water molecules in CP simulations are fully flexible it has been shown that μ can be safely set to 340 a.u.[26], whereas in the case of a fully constrained (rigid) water model larger values for μ become feasible, allowing the use of a larger MD timesteps dt[28].

Despite the rapidly increasing capability of modern supercomputers, it is still very difficult for normal *ab initio* MD (which includes all intramolecular modes) to reach statistically significant timescales for hydrophobic systems. In addition, we note that at a temperature of 300 K, $k_BT \sim 200$ cm^{-1}, whereas the high frequency intramolecular modes in water range from ∼1000 to 3500 cm^{-1}. In other words, the amount of thermal energy available to excite vibrational modes is much smaller than the lowest possible intramolecular vibrational excitations,

$$\hbar\omega \gg k_BT. \tag{1}$$

As such, a real quantum system will essentially be restricted to its vibrational ground state at 300 K. Therefore, one could argue that a rigid water model is a closer representation of the quantum system than a classical flexible model. The use of a fully constrained (rigid) water model[28] also offers the advantage of using timesteps up to 10 a.u. This extension of simulation timescales by a factor of three opens up the possibility to carry out *ab initio* trajectories beyond 100 ps at reasonable computational costs.

Since the geometry of water molecules is not expected to be significantly different in the vicinity of the solute at ambient conditions[29] compared to its bulk values, we were able to utilize the geometry of our recently developed rigid water model[28] for some of our calculations

presented in this study (simulation B in Table I). This model has been originally developed for simulations of pure water[28] and has been successfully applied to solvated Ca^{2+} [30]. Despite the success of the model and similar encouraging results from other authors[31], we have verified the results against data obtained from simulations using a fully flexible model for water. It is important to note that despite the rigid geometry that is enforced, the electronic wavefunctions are still computed from first principles and electronic charges can distribute freely - in contrast to rigid classical water models like TIP4P.

Spectroscopic studies on benzene - water clusters have shown carbon-hydrogen stretch fundamentals of benzene to be on the order of $3100cm^{-1}$ for a $benzene - water_8$ cluster[32]. To utilize the advantages of the rigid approximation, i.e. its possibility of longer timesteps, we have also constrained the C-H bonds of benzene to their optimized gas phase values.

B. Classical MD technique

For our classical MD simulations we have used the GROMACS 3.2.1 program[33] with the OPLS-AA (optimized potential for liquid simulation - all atom) force field[34,35] and the (rigid) TIP4P model for water[36,37]. Non-bonded interactions in classical simulations are typically composed of Lennard-Jones (LJ) and Coulomb potential contributions:

$$V_{LJ}(\boldsymbol{r}_{ij}) \;=\; 4\varepsilon_{ij}\Big((\frac{\sigma_{ij}}{r_{ij}})^{12} - (\frac{\sigma_{ij}}{r_{ij}})^{6}\Big). \tag{2}$$

$$V_C(r_{ij}) \;=\; \frac{1}{4\pi\varepsilon_0}\frac{q_i q_j}{\varepsilon_r r_{ij}}. \tag{3}$$

The parameters for non-bonded LJ interactions have been constructed according to the following combination rule,

$$C_{ij}^{(6)} \;=\; \Big(C_i^{(6)}\; C_j^{(6)}\Big)^{\frac{1}{2}} \tag{4}$$

$$C_{ij}^{(12)} \;=\; \Big(C_i^{(12)}\; C_j^{(12)}\Big)^{\frac{1}{2}}, \tag{5}$$

representing the geometric mean of the atom type specific σ_i- and ε_i-parameters. The empirical parameters for benzene in the classical simulations, taken from the OPLS-AA force field, are listed in Table II. The non-bonded parameters for benzene were originally developed by W.L. Jorgensen and D.L. Severance in Ref. 7. Among the five adjustable

parameters for benzene (four Lennard-Jones and one Coulomb parameter) the two σ and ϵ for O and H had to be chosen consistent with earlier force field parameters[38]. The remaining charge parameter, $q^C = -q^H$, was fitted to results of Monte Carlo simulations for liquid benzene primarily to the observed heat of vaporization and density. For comparison with the existing literature dealing with solvated benzene[11–13] we have also included one other empirical force fields for benzene[39,40] in Table II. Bonded interactions did not play a role for the dynamics since all molecules were constrained to rigid geometries, i.e. TIP4P geometry for water and experimental bond lengths for benzene as specified in Ref. 7.

The simulation box contained one benzene molecule surrounded by either 73 or 512 water molecules using periodic boundary conditions. Both NPT and NVT ensembles were simulated (T=300K; P=1atm) for up to 100 ns in the smaller simulation cell and 10 ns in the larger cell at ambient conditions. An overview of all classical and *ab initio* simulations is given in Table I.

For all systems an initial energy minimization was performed by running 500 steps of the steepest descent (SD) energy minimization method followed by 100 ps of initial MD equilibration, which were discarded and not used to collect statistics. The timestep used for the numerical integration of the equations of motion was 2 fs. Coordinates were recorded every 100 steps (0.2 ps). The list of neighboring non-bonded atoms, which is the basis for evaluating non-bonded interactions, was updated after every step using a simple search during the energy minimization and every two steps using a grid search during the MD runs. Electrostatic interactions were treated using the Particle Mesh Ewald (PME) summation[41] with cubic interpolation and van der Waals interactions were handled using twin range cut-offs[33]. All cut-offs (Coulomb, van der Waals, short range neighbor list) were chosen to be as large as possible, i.e. half of the cell size. Long range dispersion corrections were used for energy and pressure.

The rigid intramolecular geometry of all molecules in the simulation box was enforced by a SHAKE algorithm[42] with a relative geometrical tolerance of 0.001. Different initial temperature distributions were realized for classical MD simulations by randomly assigning statistical velocity distributions to all particles in the box. Temperature control was achieved with a Berendsen thermostat[43] set to a target temperature of 300K and with a time constant of 1 ps. Barostats used for isotropic pressure coupling for NPT ensembles were also of the Berendsen type using the same time constant of 1 ps.

III. RESULTS AND DISCUSSION

A. Comparison of rigid and flexible water models in *ab initio* MD simulations of solvated benzene

The most commonly calculated quantities to investigate solvation structures are radial distribution functions (RDF, or $g(r)$)[44]. In the case of benzene the mirror plane symmetry of the solute molecule can be exploited to improve statistics for the reported RDFs. To get a clearer picture of the solvation structure we have divided the space around the solute into an axial region, which is defined as the space within 20° of the axis perpendicular to the plane of the solute (z-axis), and an equatorial region, which consists of the space within 20° on both sides of the symmetry plane.

In Figures 2 and 3 we compare the RDFs for benzene-oxygen (B-O) and benzene-hydrogen (B-H) calculated for the equatorial and axial region around benzene using flexible and rigid water models (simulations A and B). In the equatorial region (Figure 2) both models agree very well with differences in peak heights around 0.2 units and in peak positions of about 0.1 Å. For both g(r)s in this region the flexible models shows slightly more structure than obtained from the rigid approximation - an observation which is consistent with results for pure water[28].

In the axial region (see Figure 3) this trend is reversed and differences between both models are far more pronounced. For $g_{B-H}(r)$ first peaks differ by 0.6 units, second peaks by only 0.05 units but with a 0.2 Å outward shift. For the sharpest peak in the system, $g_{B-O}(r)$, the rigid model gives a maximum of 3.58 whereas the flexible model yields a much softer structure with a peak height of only 2.25. However, the overall agreement is still satisfactory in the axial region since the same qualitative relation between $g_{B-H}(r)$ peaks has been established and quantitative differences are within the estimated error bars considering the relatively short simulation time (simulation A: 81 ps). A more detailed discussion of simulation times and statistical errors can be found in Section III.C. It should be noted that these differences in the axial region appear much smaller when a slightly larger definition of the axial region is chosen.

In Ref. 11 a similar comparison between structural properties of solvated benzene obtained from classical models also includes results from a flexible empirical water model (F3C/ENCAD)[45]. While this flexible model yields the softest structure among all tested classical models in both regions, our *ab initio* results for flexible water show a different trend, i.e. comparable structures in the equatorial but far less structure in the axial region. Despite the uncertainty due to the large statistical error bars for data obtained for the axial region (see Section III.C), this difference between the axial and equatorial g(r)s obtained from rigid and flexible models is significant and, again, points at the very different type of interactions in the two regions of this hydrophobic solute[3].

Since geometric constraints can alter the dynamics of some molecular systems (e.g. angular constraints in the case of macromolecules[46]), we have also calculated preferred orientations of water molecules with and without intramolecular flexibility. Measurements of such angular distribution functions are commonly performed by calculating tilt angles of water molecules which are defined as the smaller angles between the bisecting vector of the H_2O molecule and the radial vector between oxygen and the center of the solute. To resolve possible orientational effects in the equatorial and the axial region separately, we have chosen to plot the cosine of the tilt angle against the cosine of the polar angle (Θ) which is measured from the z-axis defined by the normal of the molecular plane. As a consequence the upper region close to $\cos\Theta = 1$ in Figure 4 corresponds to the axial region, while the lower end of the y-axis shows the equatorial region. Figure 4 shows the tilt angle distributions within the first solvation shell computed for the two *ab initio* simulations A (left graph) and B (center graph). Both distributions display two separate maxima, one in the axial region at a tilt angle of $\sim 46\,^\circ$ and broader distribution in the equatorial region around $120\,^\circ$. The dominant axial peak is a result of the π-H bond, whereas the orientational preference in the equatorial region is typical for small hydrophobic solutes which do not interact strongly with water. Most notable is the different relation between the two peaks in both graphs. While both tilt angle distributions agree qualitatively, the flexible model yields orientational effects of similar magnitude in both the equatorial and the axial region - an effect which can also be inferred from g(r)s in Figures 2 and 3. In contrast to that the rigid model shows a significantly stronger and sharper orientational preference for the π-H bond in the axial region while the broad peak in its equatorial region around 120° is less pronounced than for the flexible model.

B. Comparison of classical and *ab initio* MD results

Figure 5 shows the characteristic solvation structure of benzene from classical MD. Clearly visible are the first solvation shell and the difference between oxygen and hydrogen SDFs in the axial region coming from the weak π-H bond. If these classical SDFs are plotted using the same representation as for the *ab initio* data in Figure 1, both distributions become almost identical on the chosen scale. Despite these similarities in terms of SDFs, significant differences occur when RDFs of classical and *ab initio* simulations are compared. In Figure 6 we have added the g(r) from a comparable classical simulation (simulation C) to the two *ab initio* results. The large overstructuring in classical results is immediately obvious with peak heights more than twice as high. Peak positions agree somewhat better but maxima obtained from classical MD are shifted inward on average by about 0.2 Å. Even more notable is the different relation between the two axial $g_{B-H}(r)$ peaks. Both *ab initio* simulations shows a first $g_{B-H}(r)$ peak, coming from one hydrogen atom which is pointed towards the π-system, which is about half of the second peak. In contrast, classical data yields the opposite relation, where the first peak is twice as pronounced as the second one and at the same time several times stronger in magnitude. In terms of solvent orientation this corresponds to a more favorable benzene-water interaction (through a weak π-H bond) in classical MD. As mentioned earlier, it should be noted that the differences between classical and *ab initio* MD results are far less obvious if the axial region is defined as a 45° cone around the z-axis.

In the equatorial region differences between classical and *ab initio* g(r) are relatively small with classical peak maxima about 0.15 units smaller than the corresponding values from the rigid *ab initio* model and peak positions shifted outward by about 0.1 Å.

Analogous to the two *ab initio* simulations we have also computed tilt angle distributions for a classical NVT simulation (Simulation C). The right graph in Figure 4 displays the two characteristic peaks for the two regions of the system which have been found before and shows good qualitative agreement with the *ab initio* data, in particular with the rigid model. However, a close comparison reveals that classical MD gives a significantly stronger axial peak (tilt angle $\sim 46^\circ$) than the *ab initio* results but a slightly softer distribution in the equatorial region around tilt angles of about 120° (as stated before from RDFs). The

smoother distribution for the classical MD data shown in Figure 4 is due to better statistics from a longer trajectory.

The similarities between the classical models and the *ab initio* simulations for the equatorial regions, and the significant differences near the axial regions is perhaps not too surprising. Typically, empirical parameters of classical water force fields are chosen to reproduce bulk liquid properties. In the case of small hydrophobic solutes it has been shown that the hydrogen bond network mostly persists - although in a rearranged form[47,48]. Because the local hydrogen bonds are not broken, the water molecules near the solute see a environment that looks similar to the bulk and the classical models work well. However, in cases such as the axial regions around benzene where solute-water interactions become significant, the local environment changes when the water-water hydrogen bonding is no longer preserved. We note that a similar breakdown of simple classical water models should occur around large hydrophobic solutes and surface as it is not possible to preserve the water-water hydrogen bonding around an extended interface[47,48].

In the case of solvated benzene, the interfacial water molecules in the axial region are weakly bound to the π-electron system of benzene instead of forming water-water hydrogen bonds, which leads to smaller water molecule dipole moments by about 0.15 Debye when compared to the bulk as shown in Figure 8. A similar decrease in the dipole moment of the interfacial waters near the equatorial region of the solute does not occur because water-water hydrogen bonding persists in this region.

We therefore speculate that the classical water models do not properly describe the interface when solute-water interactions become large enough to disrupt the local hydrogen bond network around the solute. Similar conclusions were also inferred from studies of solvated cations where classical water models were shown to coordinate stronger to the ion and form a more rigid solvation cage[49].

C. Convergence of simulation results

In this section we use a series of long time-scale classical MD simulations to investigate the sensitivity of the computed structural properties to the choice of certain parameters and approximations that are often used. This is done in an effort to understand the differences between published results for the hydrophobic solvation of benzene, to increase the repro-

ducibility of results obtained from MD simulations and to estimate realistic error bars for our relatively short *ab initio* MD simulations.

First, we have compared the influence of different bin sizes, Δr, used for collecting statistics on the obtained RDFs. By comparing the obtained peak heights for the axial g(r) for B-O (which is the "sharpest" peak requiring the best sampling) from simulation C using bin sizes of 0.03, 0.05, 0.07, 0.09, 0.11, 0.13 and 0.2 Å it can be shown that a bin size of 0.07 Å or smaller is required to resolve correct peak heights for this most sensitive peak of our system.

Another factor which is often not reported but which quantitatively influences peak heights is the normalization of the obtained "bined" data for the g(r). In many cases the raw data is simply normalized with respect to the average particle density in the simulation box. If one is interested in the g(r) of solvent atoms around a solute in a rather small simulation cell then this "relative" normalization leads to a cell size dependency which can be misleading if comparisons are made with data from larger cells where the volume occupied by the solute becomes less relevant. Instead, normalization with respect to the ambient particle density of the pure solvent gives RDFs independent of the simulation size.

Despite ever more powerful supercomputers *ab initio* MD simulations are still limited to relatively small system sizes containing 500 - 1000 atoms and total simulation times around 100 ps[50]. To obtain an estimate for possible finite size effects we have compared classical MD simulations of solvated benzene containing 73 and 512 solvent molecules. Figure 9 shows the most sensitive RDFs, $g_{B-H}(r)$ and $g_{B-O}(r)$ in the axial region of the solute, for the NVT ensemble with 73 and 512 solvent molecules (simulations C, D). Peak heights for these NVT simulations are in almost perfect agreement with differences below 0.1, demonstrating no significant size effects on obtained RDFs despite the relatively small number of solvent molecules. Size effects on RDFs obtained from the equatorial region around benzene are not visible on the reported scale.

Another test examining finite size effects was performed for tilt angle distributions of water around the hydrophobic solute. Both distributions obtained from simulations C and D show the two preferred orientations (as in the right plot of Fig. 4) and agree quantitatively. The only notable difference is a coarser resolution of the distribution obtained from the shorter trajectory (simulation D).

Limited total simulation times constitute another serious limitation of *ab initio* MD.

While a recent study[26] has investigated the time scales required to obtain well converged structural properties in simulations of pure water, we have obtained a similar estimate for the error bars (of RDFs) in simulations of hydrophobic solutes. Since a rigorous determination of the error bars for the *ab initio* MD simulations is out of reach we obtained an estimate from our classical MD simulations. Again, we have used the g(r)s for benzene-oxygen and benzene-hydrogen in the axial region since they are the most sensitive and characteristic peaks stemming from the π-hydrogen bond in this system. Figure 10 shows ten uncorrelated g(r)s obtained from 100 ps trajectories (NVT ensemble, 73 solvent molecules, 300 K), which illustrates the magnitude of the expected variance for this structural property on a 100 ps timescale. The maxima of the first peaks of $g_{B-O}(r)$ and $g_{B-H}(r)$ both vary by about 1.2 units, whereas the second peaks of $g_{B-H}(r)$ differ by 0.6 units. The same type of analysis for ten 10 ns trajectories shows differences of 0.23 units for the first B-H peak and about 0.1 units for the second B-H peak.

A comparison of NVT vs. NPT ensembles with consistent average pressure and volume (simulations D and F) is shown in Figure 11. The small difference of the $g_{B-O}(r)$ RDFs is within the estimated statistical error bar for simulations of 10 ns.

D. Sensitivity with respect to empirical force field parameters

Recently two studies have investigated different aspects of the hydrophobic solvation of benzene[11,13]. In Ref. 11 (which was reanalyzed in Ref. 12) the authors have used different force fields and water models to investigate the hydration of benzene and compare it to cyclohexane. While shape and peak positions of comparable benzene RDFs are the same, peak heights of the B-O and B-H peaks in the axial region differ quantitatively when compared to our results. Results from simulation F, which are shown in Figure 11, display peak heights of 6.10 and 4.12 Å whereas Ref. 11 reports 5.44 and 3.60 Å for axial $g_{B-O}(r)$ and $g_{B-H}(r)$, as shown in Figure 12.

Schravendijk and van der Vegt (Ref. 13) have studied the effect of benzene-water hydrogen bonding on hydrophobic hydration compared to a "van der Waals model" of benzene which is not capable of forming such weak H-bonds. When comparing RDFs from different studies, it should be noted that the obtained axial distributions are highly sensitive with respect to the definition of this axial region. The definition of the axial region in Ref. 13 includes

a 90° cone (45° around the z-axis) which leads to far less structured RDFs for both B-O and B-H because it includes a significant amount of water molecules which do not bind to the π-electron system through a weak H-bond. Results from simulations C-F are almost indistinguishable if compared for this extended region (45° instead of 20°) and on this scale. After recalculating RDFs for this differently defined axial region we find differences in benzene-hydrogen first peak heights of about 0.2 and a somewhat different shape of the benzene-oxygen double peak (Figure 13). The first $g_{B-O}(r)$ peak consists of two maxima, one from H_2O molecules which take part in the weak hydrogen bond and one from ordinary solvent molecules of the first solvation shell. Analogous to the results for benzene-hydrogen our classical data shows a stronger first benzene-oxygen maximum corresponding to a more favorable π-hydrogen bond compared to the results from Ref. 13.

The most likely cause for the differences in Figure 13 is the use of different force fields (GROMOS43A1 vs. OPLS-AA, see Table II) and water models (SPC vs. TIP4P). In the GROMOS43A1 parameter set atomic charges on carbon and hydrogen of benzene are slightly smaller which could lead to the observed softer solvation structure around benzene.

From our extensive analysis of different classical simulation parameters for this system, only part of which is shown in this paper, we are able to draw two main conclusions: Firstly, the results from classical MD simulations vary quantitatively depending on the chosen force field, water model and on subtle technical details of the simulation and statistical analysis of the results. Secondly, despite those quantitative differences between classical results all of the empirical-model based simulations examined here as well as in other work[11] show systematic qualitative differences when compared to *ab initio* results for the interfacial region where solute-solvent interactions are significant, i.e. they yield a much stronger π-hydrogen bond between water and benzene.

IV. CONCLUSION

Solvated benzene constitutes a unique test case for molecular simulations because it presents two different interfaces to the solvent. The equatorial region resembles normal hydrophobic solvation of aliphatic hydrocarbons, whereas the axial region displays a weak π-hydrogen bond between solute and solvent molecules which alters the electronic structure at the interface. Both flexible and rigid *ab initio* water models represent the hydration

structure at both interfaces well and show good agreement. To make statistically meaningful comparisons between simulations we have carefully investigated the role of several simulation parameters such as finite size and time scale effects.

Commonly used (nonpolarizable) classical water models give a robust description of the equatorial region where strong water hydrogen-bonds persist and no significant solute-solvent interactions are present. In the axial region these simple water models cannot adapt to the altered environment and there is a tendency to "overbind" the π-hydrogen bond, which leads to qualitatively different solvation structures. We conclude that this limitation of simple (yet commonly used) classical models occurs when solute-solvent interactions become comparable in strength to regular water hydrogen-bonds, which in turn leads to a disruption of the water-water hydrogen bond network near the solute. Although the exact magnitude of the differences between *ab initio* and classical MD simulations for the axial region may be influenced by subtle effects, such as possible inaccuracies in the description of dispersion interactions, the overall trends due to the disruption of the hydrogen bond network should persist. Based on these findings we expect that simple classical models should provide a qualitatively correct description of small solvated aliphatic hydrocarbons, but may not adequately represent small solutes that involve significant solute-solvent interactions, such as the aromatic groups that are abundant in biochemistry.

The authors would like to thank Giancarlo Cicero and Edmond Y. Lau for helpful discussions. This work was performed under the auspices of the U.S. Dept. of Energy at the University of California/Lawrence Livermore National Laboratory under contract no. W-7405-Eng-48 and was supported in part by DOE grant DE-FG02-04ER25625.
UCRL-JRNL-234592

---

[1] H. A. Scheraga, M. Khalili, and A. Liwo, Annual Review of Physical Chemistry **58**, 57 (2007).

[2] A. Wallqvist, E. Gallicchio, and R. Levy, J. Phys. Chem. B **105**, 6745 (2001).

[3] M. Allesch, E. Schwegler, and G. Galli, J. Phys. Chem. B **111**, 1081 (2007).

[4] G. Ravishanker, P. K. Mehrotra, M. Mezei, and D. L. Beveridge, J. Am. Chem. Soc. **106**, 4102 (1984).

[5] P. Linse, G. Karlström, and B. Jönsson, J. Am. Chem. Soc. **106**, 4096 (1984).

[6] P. Linse, J. Am. Chem. Soc. **112**, 1744 (1990).

[7] W. L. Jorgensen and D. L. Severance, J. Am. Chem. Soc. **112**, 4768 (1990).

[8] S. Urahata, K. Coutinho, and S. Canuto, Chem. Phys. Lett. **274**, 269 (1997).

[9] S. Urahata and S. Canuto, Chem. Phys. Lett. **313**, 235 (1999).

[10] A. Laaksonen, P. Stilbs, and R. E. Wasylishen, J. Chem. Phys. **108**, 455 (1998).

[11] T. M. Raschke and M. Levitt, J. Phys. Chem. B **108**, 13492 (2004).

[12] T. M. Raschke and M. Levitt, PNAS **102**, 6777 (2005).

[13] P. Schravendijk and N. F. A. van der Vegt, J. Chem. Theory Comput. **1**, 643 (2005).

[14] S. Ikawa, J. Chem. Phys. **123**, 244507 (2005).

[15] S. Suzuki *et al.*, Science **257**, 942 (1992).

[16] J. C. Grossman, E. Schwegler, and G. Galli, J. Phys. Chem. B **108**, 15865 (2004).

[17] F. Gygi, *GP 1.24.0: A general ab initio molecular dynamics program*, Lawrence Livermore National Laboratory, 2003.

[18] F. Gygi, *The Qbox code*, Lawrence Livermore National Laboratory, 2005.

[19] P. Hohenberg and W. Kohn, Phys. Rev. B **136**, 864 (1964).

[20] W. Kohn and L. J. Sham, Phys. Rev. A **140**, 1133 (1965).

[21] J. P. Perdew, K. Burke, and M. Ernzerhof, Phys. Rev. Lett. **80**, 891 (1998).

[22] D. R. Hamann, Phys. Rev. B **40**, 2980 (1989).

[23] L. Kleinman and D. M. Bylander, Phys. Rev. Lett. **48**, 1425 (1982).

[24] R. Car and M. Parrinello, Phys. Rev. Lett. **55**, 2471 (1985).

[25] G. Galli and M. Parrinello, in *Computer Simulation in Materials Science*, edited by M. Meyer and V. Pontikis (Kluwer Academic Publishers, Netherlands, 1991), pp. 283–304.

[26] J. C. Grossman *et al.*, J. Chem. Phys. **120**, 300 (2004).

[27] E. Schwegler, J. C. Grossman, F. Gygi, and G. Galli, J. Chem. Phys. **121**, 5400 (2004).

[28] M. Allesch, E. Schwegler, F. Gygi, and G. Galli, J. Chem. Phys. **120**, 5192 (2004).

[29] Y. Danten, T. Tassaing, and M. Besnard, J. Phys. Chem. A **103**, 3530 (1999).

[30] F. C. Lightstone *et al.*, ChemPhysChem **6**, 1745 (2005).

[31] K. Leung and S. B. Rempe, Phys. Chem. Chem. Phys. **8**, 2153 (2006).

[32] C. J. Gruenloh *et al.*, Science **276**, 1678 (1997).

[33] E. Lindahl, B. Hess, and D. van der Spoel, J. Mol. Mod **7**, 306 (2001).

[34] G. Kaminski, F. A. Friesner, J. Tirado-Rives, and W. L. Jorgensen, J. Phys. Chem. B **105**, 6474 (2001).

[35] W. L. Jorgensen, D. S. Maxwell, and J. Tirado-Rives, J. Am. Chem. Soc. **118**, 11225 (1996).

[36] W. L. Jorgensen *et al.*, J. Chem. Phys. **79**, 926 (1983).

[37] W. L. Jorgensen and J. D. Madura, Mol. Phys. **56**, 1381 (1985).

[38] W. L. Jorgensen, J. Am. Chem. Soc. **110**, 1657 (1988).

[39] W. R. P. Scott *et al.*, J. Phys. Chem. A **103**, 3596 (1999).

[40] C. Oostenbrink, A. Villa, A. E. Mark, and W. F. V. Gunsteren, J. Comput. Chem. **25**, 1656 (2004).

[41] U. Essmann *et al.*, J. Chem. Phys. **103**, 8577 (1995).

[42] J. P. Ryckaert, G. Ciccotti, and H. J. C. Berendsen, J. Comput. Phys. **23**, 327 (1977).

[43] H. J. C. Berendsen *et al.*, J. Chem. Phys. **81**, 3684 (1984).

[44] M. P. Allen and D. J. Tildesley, *Computer Simulation of Liquids* (Clarendon Press, Oxford, 1987).

[45] M. Levitt *et al.*, J. Phys. Chem. B **101**, 5051 (1997).

[46] W. F. van Gunsteren and M. Karplus, Macromolecules **15**, 1528 (1982).

[47] D. Chandler, Nature **417**, 491 (2002).

[48] D. Chandler, Nature **437**, 640 (2005).

[49] J.White, E. Schwegler, G. Galli, and F. Gygi, J. Chem. Phys. **113**, 4668 (2000).

[50] F. Gygi *et al.*, in *SC '05: Proceedings of the 2005 ACM/IEEE conference on Supercomputing* (IEEE Computer Society, Washington, DC, USA, 2005), p. 24.

List of Figures

Figures

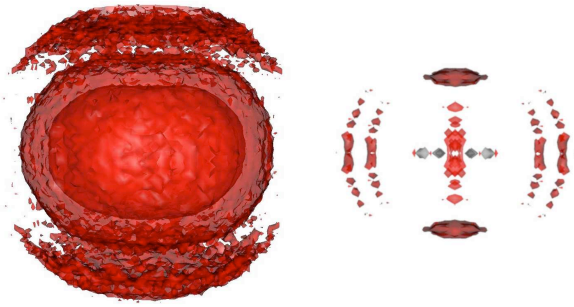

FIG. 1:

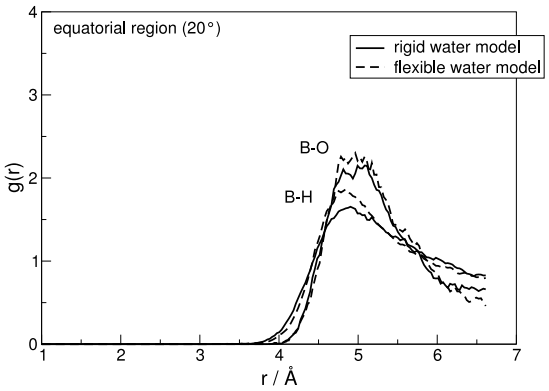
equatorial region (20°)
rigid water model
flexible water model
B-O
B-H
g(r)
r / Å
0
1
2
3
4
1
2
3
4
5
6
7

FIG. 2:

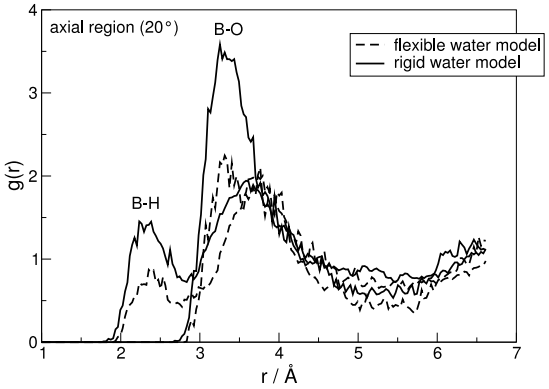
axial region (20°)
B-O
B-H
flexible water model
rigid water model
g(r)
r / Å
0
1
2
3
4
1
2
3
4
5
6
7

FIG. 3:

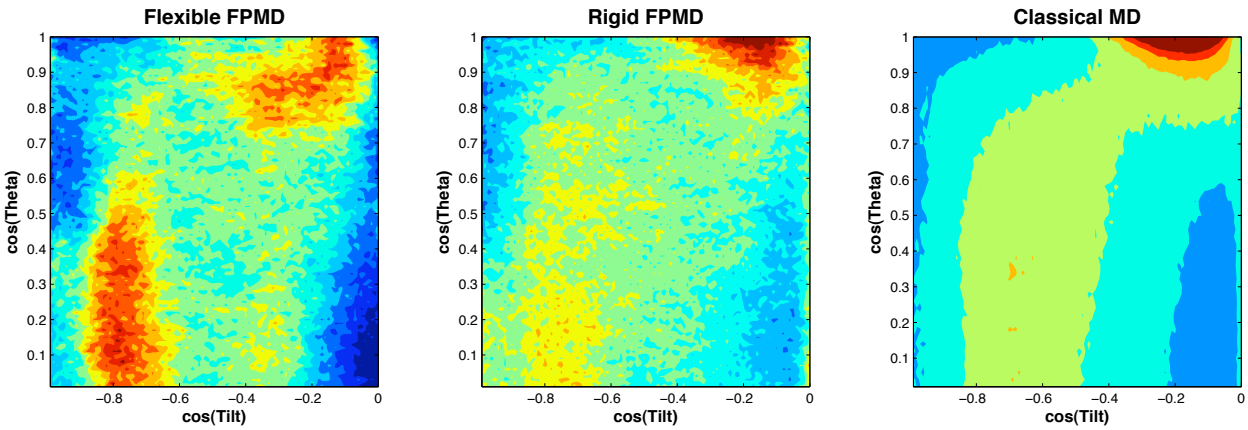
Flexible FPMD
Rigid FPMD
Classical MD
cos(Theta)
cos(Tilt)
1
0.9
0.8
0.7
0.6
0.5
0.4
0.3
0.2
0.1
−0.8
−0.6
−0.4
−0.2
0

FIG. 4:

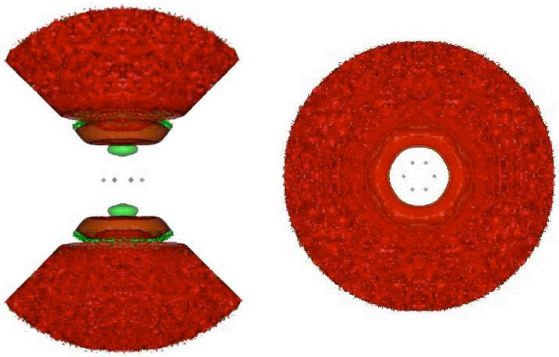

FIG. 5:

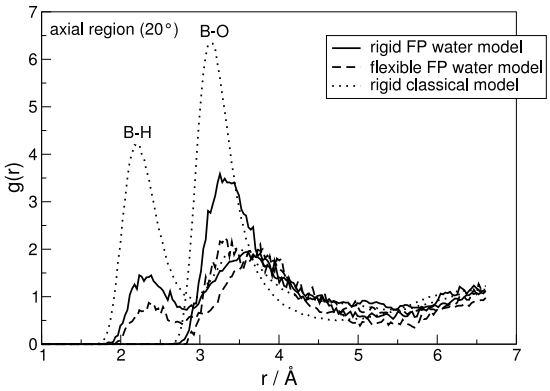
axial region (20°)
B-O
B-H
rigid FP water model
flexible FP water model
rigid classical model
g(r)
r / Å
0
1
2
3
4
5
6
7

FIG. 6:

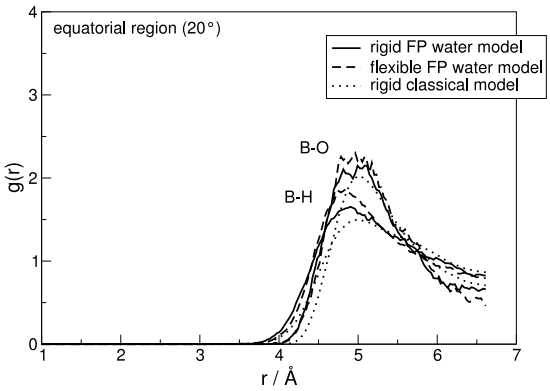
equatorial region (20°)
rigid FP water model
flexible FP water model
rigid classical model
B-O
B-H
g(r)
r / Å
0
1
2
3
4
1
2
3
4
5
6
7

FIG. 7:

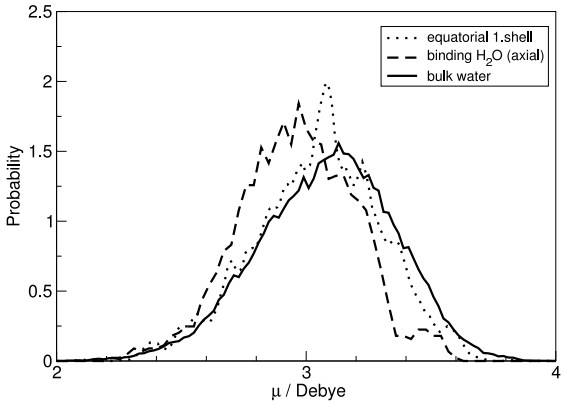
equatorial 1.shell
binding H_2O (axial)
bulk water
Probability
μ / Debye
2.5
2
1.5
1
0.5
0
2
3
4

FIG. 8:

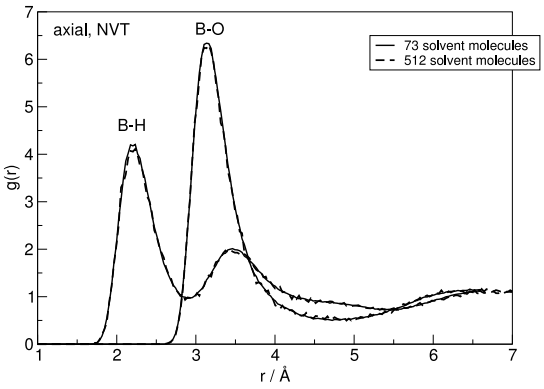
axial, NVT
B-O
B-H
73 solvent molecules
512 solvent molecules
g(r)
r / Å
0
1
2
3
4
5
6
7

FIG. 9:

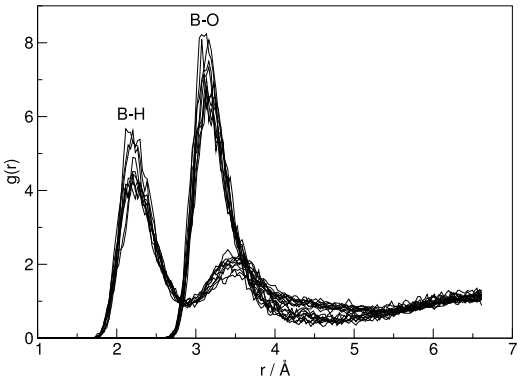

FIG. 10:

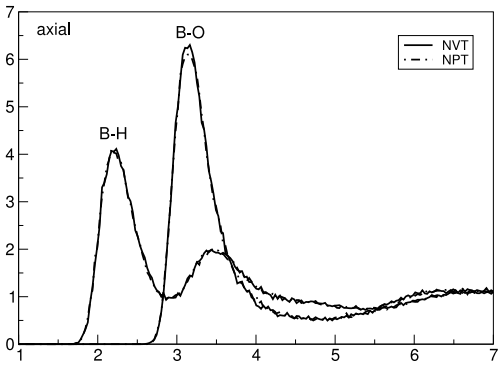

FIG. 11:

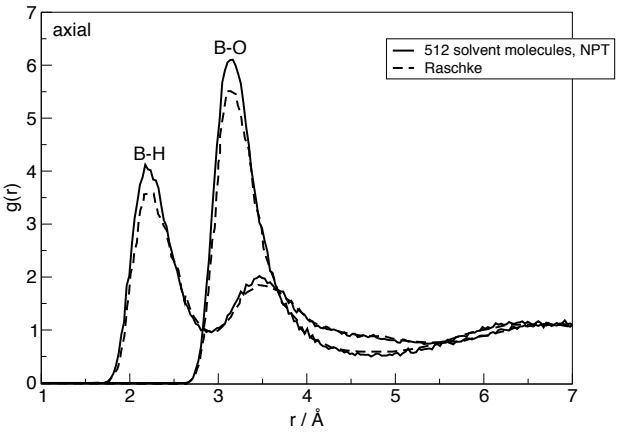
axial
B-O
B-H
512 solvent molecules, NPT
Raschke
g(r)
r / Å
0
1
2
3
4
5
6
7

FIG. 12:

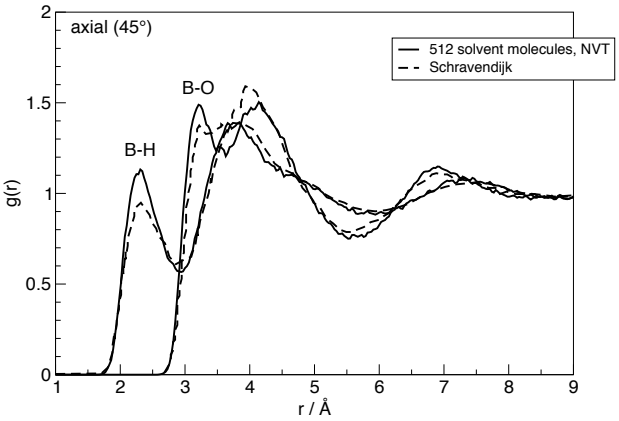
axial (45°)
512 solvent molecules, NVT
Schravendijk
B-O
B-H
g(r)
r / Å
0
0.5
1
1.5
2
1
2
3
4
5
6
7
8
9

FIG. 13:

Tables

TABLE I: Overview of the MD simulations: Size refers to the number of water molecules included in the simulation cell. In our rigid FP simulation a rigid water geometry was enforced and the carbon-hydrogen bonds of benzene were constrained to eliminate fast vibrational modes in the system.

Name	Method	Geometry	size	T (K)	dt (fs)	μ (a.u.)	time (ns)
A	FP	Flexible	73	297.5 (NVE)	0.07	340	0.081
B	FP	Rigid	73	303.3 (NVE)	0.24	1100	0.152
C	Classical	Rigid	73	(NVT)	2	-	100
D	Classical	Rigid	512	(NVT)	2	-	10
E	Classical	Rigid	73	(NPT)	2	-	30
F	Classical	Rigid	512	(NPT)	2	-	10

TABLE II: Empirical nonbonded interaction parameters for the benzene-water interactions used in classical MD simulations.

Force Field	$q^C(e)$	$q^H(e)$	σ^C (Å)	ϵ^C (kcal/mol)	$\sigma^H(\mathring{A})$	ϵ^H (kcal/mol)
OPLS-AA [a]	-0.115	0.115	3.5500	0.07	2.4200	0.03
GROMOS 43A1	-0.100	0.100	3.3611	0.09697	2.3734	0.02828

[a]OPLS-AA parameters for benzene were originally taken from Ref.[7]. The GROMOS43A1 force fields was used in Ref.[13], OPLS-AA was also used in Ref.[11].

LAWRENCE
LIVERMORE
NATIONAL
LABORATORY

LLNL-JRNL-407978

Water confined in nanotubes and between graphene sheets: A first principle study

G. Cicero, J. C. Grossman, E. Schwegler, F. Gygi, G. Galli

October 21, 2008

Journal of the American Chemical Society

Water confined in nanotubes and between graphene sheets: a first principle study

Giancarlo Cicero[1], Jeffrey C. Grossman[2], Eric Schwegler[3], Francois Gygi[4] and Giulia Galli[4]*

[1] Politecnico of Torino, Torino, Italy.

[2] Center of Integrated Nanomechanical Systems, University of California, Berkeley.

[3] LLNL, Livermore, CA.

[4] University of California, Davis, CA

Corresponding Author: G. Cicero, e-mail: giancarlo.cicero@polito.it

TITLE RUNNING HEAD. Water in hydrophobic confinement

ABSTRACT. Water confined at the nanoscale has been the focus of numerous experimental and theoretical investigations in recent years, yet there is no consensus on such basic properties as diffusion and the nature of hydrogen bonding (HB) under confinement. Unraveling these properties is important to understand fluid flow and transport at the nanoscale, and to shed light on the solvation of biomolecules. Here we report on a first principle, computational study focusing on water confined between prototypical non polar substrates, i.e. single wall carbon nanotubes and graphene sheets, 1 to

[*] Physics Department, Politecnico of Torino, C.so Duca degli Abruzzi 24, 10129 Torino, Italy. Tel. +39 011 5647370, Fax. +39 011 5647399, E-mail: giancarlo.cicero@polito.it

2.5 nm apart. The results of our molecular dynamics simulations show the presence of a thin, interfacial liquid layer (~ 5 Å) whose microscopic structure and thickness are independent of the distance between confining layers. The properties of the hydrogen bonded network are very similar to those of the bulk outside the interfacial region, even in the case of strong confinement. Our findings indicate that the perturbation induced by the presence of confining media is extremely local in liquid water, and we propose that many of the effects attributed to novel phases under confinement are determined by subtle electronic structure rearrangements occurring at the interface with the confining medium.

I. INTRODUCTION

Water confined in nanometer-sized channels or pores is expected to have structural and dynamical properties different from those of the bulk liquid[1-8]. In recent years a widespread effort has been dedicated to understand how the properties of water change upon nanoscale confinement and how these changes may influence a wide range of systems, e.g. biological systems, flow in organic and inorganic media, the properties of materials such as zeolites and cements, and nanoparticles in solution. An important question concerns the influence of the confining medium, in particular whether a confined phase of water exists that is independent of confining surfaces or whether interface properties represent the dominant influence on the nanoscale liquid. In the absence of confinement, many experimental results (see e.g. Ref 9-11) indicate that the perturbation of water at both hydrophilic and hydrophobic interfaces is local, however it is yet unclear whether such locality of the perturbation persists at the nanoscale. In addition, results on the diffusion properties of the confined liquid are rather controversial.

Several years ago fast transport of water in carbon nanotubes (CNT) was reported by Hummer *et al.*[1] who, using classical molecular dynamics (MD) simulations, found that for small diameter tubes (8.1 Å) diffusion occurs through a burst-like mechanism, stemming from the presence of single file water chains capable of moving with little resistance. These results were later rationalized with a simple coarse-grained model of a nanotube immersed in water[2] and similar findings were reported for model biological pores[3]. Exceptionally fast mass transport in CNT was also found by Holt *et al.*[4] and by

Majumder *et al*.[5] in very recent experiments, which were however conducted for tubes of larger diameter than those studied in Ref. 1-3 (~ 2nm and ~ 7 nm in Ref. 4 and 5, respectively). The TEM measurements of Naguib *et al*.[12] on water embedded in ultra thin CNT, indicated instead that the fluid mobility is greatly decreased. Similar conclusions, but for different confining surfaces, were reached by Major *et al*.[13] who observed a dramatic change in the mechanical properties of water at the nanometer scale. For confining hydrophilic surfaces with separation less than 1 nm, the viscosity of the fluid measured in Ref. 13 was 7 orders of magnitude greater than that of the bulk at room temperature. In contrast, studies of the viscosity of water confined between mica surfaces[14-15] (at distances equal to or smaller than 3.5 ±1 nm) do not point at fast transport, with measured viscosity values[14-15] within a factor of three of the bulk.

Several studies[7,16-17] have shown that confined water freezes at a lower temperature[18] than the bulk liquid, and that new ice-phases appear to be stabilized by confinement. In particular, Koga *et al*.[7,16] used classical MD simulations to show that in CNTs (with diameters ranging from 1.1 to 1.4 nm) water can exhibit structural and phase transitions under an axial pressure of 50 MPa to 500 MPa. Following this work, Kolesnikov *et al*.[17] performed neutron scattering experiments on water contained in CNT and identified an ice-shell plus a water chain structure that shows soft, "fluid-like" behavior even at temperatures as low as 50 K. Monolayer and bilayer ice structures were also reported for water confined between graphene sheets by Zangi *et al*.[19-20] when pressure was applied to the system. However, results of other classical simulations showed water freezing between graphene layers at ambient temperature[21], but pressure values were not determined in this case and thus a consistent comparison with other, similar works is not straightforward.

Building on the pioneering work of Rahman and Stillinger[22], classical MD simulations have been extensively used to study the properties of bulk water and recently also of confined water; various force fields have been employed, including simple point charge models (either rigid or flexible SPC) or other parameterizations such as TIP3P and TIP4P[23]. For example, using a flexible SPC model, Martì *et al*.[24-28] studied confinement in CNT and within graphene sheets, and they observed the presence of layered

structures, that exhibit a substantial number of broken H-bonds, and a self-diffusion along the tube axis that is faster than in the bulk. On the contrary, lower mobility was reported by Mashl *et al*.[6] who, using a rigid SPC model found that at ambient conditions water in (9x9) CNT undergoes a transition to a state with ice-like mobility. Similarly, Liu *et al*.[29,30] reported axial and radial diffusivities in CNTs much lower than those of the bulk, with diffusivity decreasing with the diameter of the tube. Hanasaky *et al*.[31] also observed slower diffusion under confinement and found that the dependence of water mobility (namely, H-bond lifetime) on the tube diameter is not monotonic. Finally, Choudhury *et al*.[32] reported that both the translational and re-orientational mobilities of water confined between graphene sheets are greatly decreased for separations below 1.3 nm. We note that in Ref. 29-32 a rigid SPC model was used, at variance from Refs. 24-28 where flexible models were adopted.

The brief (and incomplete) summary presented above clearly highlights inherent difficulties still present experimentally in probing the properties of confined water, and a dependence of results on the parametrization of force-fields, in classical MD simulations. A discussion of the sensitivity of confined water properties on force fields has been given, for example, in Ref. 33 where quantum chemistry calculations were used to benchmark some classical potential results. It is therefore of interest to study confined water with simulations that do not rely on any fitted parameters, in order to investigate microscopic properties not yet accessible to experiment (e.g. interfacial microscopic structure), including electronic structure effects.

In this paper we restrict our attention to hydrophobic confinement, and we report on a theoretical study based on *first principle* MD aimed at understanding structural and diffusion properties of water confined in single wall carbon nanotubes and between graphene sheets—systems that have received much experimental attention lately. We investigated the properties of the liquid as the separation between confining surfaces (CNT radius and distance between graphene sheets) is varied, with the goal of establishing the influence of the interface on structural and diffusion properties. The presence of a surface induces density oscillations in the liquid, with a thin region from which water molecules are excluded, followed by a layer with increased particle density. The structure of the liquid within this

interfacial layer is substantially different from that of the bulk, but it does not depend on surface separation, indicating that the nature of the perturbation induced by the surface is well localized, down to very small confinement separations. The electronic and mass density averaged over the interfacial layer are smaller than those of the bulk. However, even for very small separations, the HB network of the confined liquid is found to be similar to that of the bulk, outside the thin interfacial layer (~ 5 Å). We find that lateral diffusion and re-orientational motion of water molecules become faster under confinement, possibly due to a decrease of the dipole moment of interfacial molecules and thus weaker HBs at the interface.

II. METHOD

In this work, water was confined between graphene sheets (planar confinement) and within single wall CNT (cylindrical confinement) (see Table I). The starting configurations for the *first principle* simulations were obtained by performing MD simulations (NVT) with SPC/E classical potentials[34]. We chose the SPC/E model because tested parameters to describe the interaction between water and graphite surfaces and nanotubes were available in the literature[35]. In particular the carbon atoms were modeled as neutral particles interacting with the oxygen atoms through a Lennard-Jones potential determined by the parameters $\in_{co}$ = 0.3135 kJ/mol and σ_{co} = 0.319 kJ/mol[35]. In the graphene/water system the cell dimensions in the wall plane (x,y) were fixed and determined by the size of a relaxed graphene sheet containing 60 carbon atoms (12.4 Å / 12.1 Å). Carbon-carbon distances were fully optimized. In the z direction, the interlayer separation was varied, while keeping the number of water molecules constant, until the stress along this direction yielded a pressure equal to atmospheric pressure. Three confined water systems were considered with graphene layers at 10.09, 14.41 and 25.02 Å distance. From these calculations we estimated the thickness of the exclusion volume present at the graphene/water interface to be ~ 2 Å. This thickness was employed in the case of NT confinement to determine the number of molecules needed to fill up the tubes in order to obtain a density of ~ 1 g/cm^3. We used two semiconducting tubes to confine water, namely a (19×0) NT and a (14×0) NT, which have

a diameter of 15.0 Å and 11.1 Å respectively. The length of the tube (i.e. the number of minimal unit cell in the axial direction needed to accommodate more than 30 water molecules) was 17.065 Å for the (19×0) NT and 25.251 Å for the (14×0) NT. All samples were classically equilibrated for 100 ps and the final structure was then used as input for the *first principle* simulations.

We used Density Functional Theory (DFT)[36,37], in the generalized gradient corrected approximation (PBE)[38], and Born-Oppenheimer (BO) molecular dynamics (MD). We employed non-local pseudopotentials[39], the electronic wavefunctions (charge density) were expanded in plane waves, with energy cutoff up to 85 (340) Ry and the integration over the Brillouin zone was performed with the Γ point of the supercell. The numerical integration of the ion equations of motion was carried out with a time step of 20 a.u. (8 electronic steps using preconditioned steepest descent with Anderson extrapolation were performed to obtain the electronic ground state at each atomic step). In our *first principle* calculations, the atomic configuration obtained with a classical simulation run was first equilibrated with a velocity rescaling technique for about 3 ps at 400 K. Then the thermostat was removed and statistics was collected for the simulation time reported in Table I. All the calculations were done considering D_2O instead of H_2O; this allows one to employ larger MD time step and thus to simulate for longer times with the same amount of computer resources.

Since the purpose of the present investigation was to compare the properties of confined water with those of bulk water, we considered the temperature (400 K) at which, for bulk water, DFT using PBE and BO dynamics yields results in good agreement with experiment for structural and diffusion properties at ambient conditions[40,41]. There are several possible reasons why elevated simulation temperatures are required in the *first principle* simulations. For instance, van der Waals (vdW) dispersion interactions are not expected to be accurately reproduced by semi-local GGA functionals such as PBE or BLYP. However, we note that of the three contributions to vdW forces – induction, thermal orientation and dispersion – it is the dispersion forces that are not well described, and in liquid water, their strength is approximately one order of magnitude smaller than that of hydrogen bonding. As pointed out in Refs. 41-42, in addition to possible inaccuracies in the GGA functionals, it is possible

that a large fraction of the disagreement is due to the neglect of the quantum motion of hydrogen atoms in the simulations. All DFT based molecular dynamics simulations of water (except for one[43]) have been carried out using a classical description (Newtonian dynamics) of the proton dynamics. There is growing evidence based on empirical potentials fit to quantum chemical data that proton quantum effects in water may be more pronounced than previously thought (e.g. see Ref. 41); hence it is possible that commonly used GGA functionals such as PBE and BLYP yield a quite accurate description of hydrogen bonding in water, once proton quantum effects are taken into account. We also note that approximately accounting for quantum effects via temperature rescaling is a technique that has been used in a variety of materials other than water[44,45].

At 400K, the computed diffusion coefficient of bulk water is ~ 1 10^{-5}cm^2/sec. A statistical error bar on this number can be estimated from a convergence of the diffusion coefficient as a function of simulations time, carried out for a potential yielding very similar diffusion and structural properties for the liquid. We carried out such a convergence study in Ref. [40-41], where the error of the self-diffusion constant obtained over 20 ps simulations is found to be 20-30%.

In addition to studying liquid water in contact with graphene and carbon nanotubes, we also investigated the interaction of a single water molecule with a graphene plane, by considering both the equilibrium structure at T=0 and snapshots taken from our 400K MD trajectory. While at T=0 a water molecule is found to be barely bound to graphene (with a binding energy of ~ 0.25 kcal/mole), for configurations corresponding to finite T, we find a binding energy (defined as the difference between the energies of the interacting and non interacting graphene/water system) of 1-2 kcal/mole. In the high T configurations, thermal energy induces bond distortions in the graphene sheet and in the water molecule, resulting in local dipoles (charge transfer) that strengthen water/graphene interaction. In addition, at finite T, we find overlap between the carbon and water charge densities and electron-dynamical effects that are responsible for characteristic features detected in IR spectra (these are discussed in detail elsewhere[46]). A variety of values have been reported experimentally and theoretically for the interaction of gas phase water with graphite and these are summarized in Ref. 47.

Our *first principle* MD simulations were carried out using *Qbox*[48], while maximally localized Wannier functions, used to compute water molecular dipole for selected MD configuration, were obtained by using the *GP* code[49] following the scheme proposed by Gygi *et al*.[50]. Finally, classical simulations were performed with *GROMACS*[51].

III. RESULTS AND DISCUSSION

In this section we first describe the results of our simulations, then we present an interpretation of our findings. Table I summarizes the simulations carried out in the present study.

Structural Properties--The analysis of the water density in the direction perpendicular to the surface reported in the top panels of Fig. 1 reveals density oscillations typical of a liquid in contact with a hard wall[10,52-53]. In particular, in the case of graphene we found that water molecules are excluded from a region with thickness of ~ 2.5 Å; the particle density rises sharply outside this excluded volume, with a first peak extending up to 5 Å, similar to what found for water on hydrogenated diamond surfaces[46], that are much less polarizable than graphene sheets. The height of this peak increases with decreasing distance between the surfaces (from 2.38 g/cm^3 to 1.96 g/cm^3 in going from 10.09 Å to 25.02 Å), but its position is independent of the confining length. From a comparison of the top panels of Fig. 1 (a-e) it is clear that increased confinement results in enhanced density oscillations. This may be understood in terms of interfering effects of the two facing surfaces, and at extreme confinement the perturbation induced on water at the two interfaces is amplified. In panel (c) of Fig. 1, where the distance between graphene sheets is the largest (25.02 Å), density oscillations are nearly suppressed, indicating that the effect of the surface perturbation is highly localized. In this case, only the water layer close to the surface has density higher than the bulk; beyond ~ 5 Å from the surface the density curve becomes flatter and reaches the bulk value (1.0 g/cm^3). We note that in all of the deuterium density profiles reported in Fig. 1, a small shoulder is present in the first density peak, which indicates a slight preference for some interfacial water molecules to orient with an OD bond pointing towards the surface.

The middle panels of Fig. 1 show the variation of the electronic density (ρ_{el}) in the direction

perpendicular to the surface. In the region from which water molecules are excluded, we observe a sharp decrease of ρ_{el}, which vanishes at about 2 Å. These findings are consistent with the results on the electronic density as obtained from X-ray measurements by Poyron et al.[54]. In this region the contributions to ρ_{el} come almost entirely from the surface carbon atoms. Outside this layer of zero particle density, we observe oscillations of ρ_{el}; their intensity is slightly larger at the position of the first sharp peak in the particle density distribution than in the center of the slab. Very similar results were obtained also for *first principle* simulations of water confined by hydrogentated diamond surfaces.[46]

Interesting structural information about confined water is also obtained from an analysis of the bottom panels of Fig. 1, where the average number of hydrogen bonds (HBs) per water molecule is reported as a function of the distance from the surface. Interfacial molecules, although surrounded by only half of a bulk coordination shell, are still engaged in a relatively large number of HBs. In particular in the 5 Å interfacial layer, the number of HB (2.5) amounts to about 70% of the corresponding bulk value (recovered in the middle of the slab). This observation is consistent with the experimental finding on the structure of interfacial water as obtained through vibrational spectroscopy by sum-frequency generation (see e.g. Ref. 55), it also agrees with previous molecular dynamics simulations in which it was found that water in contact with solid surfaces[52,53,56] readily restores its liquid, bulk-like hydrogen bonded network, just outside the thin interfacial layer. The thickness of this layer is slightly larger than in the hydrophilic case where, e.g. for hydroxilated Si-SiC surfaces[56], we found values of ~ 3.5 Å. The dashed and dotted curves in the bottom panels of Fig. 1 represent, respectively, the number of HB acceptors and donors of each water molecule in our samples. When approaching the confining surface, a water molecule preferentially has a higher number of HB donors; thus, most of the time, one of its deuterium atoms is not engaged in HBs, consistent with features observed in the analysis of the OD tilt angle distribution (see Fig. 2). This property appears to be independent of the confinement distance, and it is rather determined by the water/surface interaction.

Similar results for the structure of the interfacial layer and their dependence on water-surface interaction were obtained in the case of the two CNTs. However layering effects are enhanced in the

tubes, and cylindrical water shells appear, instead of flat layers (only one shell for the smaller tube and two for the larger one). For both tubes (see Table I), we found a very pronounced peak in the density of water in proximity of the walls [the height reaches 3.6 g/cm^3 in the case of the (14×0) NT and 2.6 g/cm^3 for the (19×0)]. Remarkably, for the smallest tube the water density in the center is almost zero, and molecules appear to be densely packed at the interface; therefore one might expect a decrease in diffusion of the fluid relative to the bulk. As we will see, this is not the case.

In order to further investigate water restructuring at the interface, we have studied the orientation of the OD bonds with respect to the direction perpendicular to the interface (radial direction in the case of nanotubes). In Fig. 2, we report the OD tilt angle distribution for water confined between graphene layers. The color maps represent the probability of finding, at a certain distance from the surface, an OD bond forming a specific angle (θ) with the direction perpendicular to the substrate (see inset of Fig. 2 for the definition of tilt angle): for every molecule two tilt angles are calculated, one for each OD bond. The probability has been multiplied by the value of the water density, to enhance the signal of the denser layers. At the interface, molecules have strong preferential orientations. In particular at about 2.7 Å from the surface two angles are favored: 75° and 150°. This geometric configuration corresponds to water molecules having one of the OD bonds nearly parallel to the surface and the other pointing towards it. At 3.3 Å, the opposite orientation in found with an OD pointing away from the surface (25°) and the other nearly parallel (100°) to it. At about 3 Å, there is a strong peak at 90°, indicating that most of the molecules have both OD bonds roughly parallel to the surface. In the high density layer, the planar orientation is preferred in order to maximize in-plane HBs. The most remarkable feature of the three maps reported in Fig. 2 is that the orientation of water bonds in the interfacial layer does not depend on surface separation. At a graphene distance of 10.09 Å, the system consists of only two water layers, yet these appear to be equivalent to the two interfacial layers observed for the 25.02 Å separation. A similar behaviour was found in the case of water confined in CNT when calculating the orientation of the OD bonds with respect to the radial direction. Although the preferential angles are slightly different because the surface is curved, the qualitative features of the angular distribution are

very similar, and the interfacial layer structuring appears to be independent on the confining distance (i.e. tube diameter). In the case of the smallest nanotube, water molecules arrange in one cylindrical shell, thus no water molecules show bonds oriented towards the centre of the cylinder, as hardly any H-bonds can be formed in that direction (the peak at ~25° in the angular distribution is not observed in this case). These results appear to be at variance from those of Hummer, *et al.*[1], that find a linear chain localised in the center of a smaller nanotube.

Fig. 3a shows the calculated oxygen (red) and deuterium (blue) spatial distribution functions (SDF) in a water layer within 5 Å from the surface for the case of water confined between graphene layers separated by 14.41 Å. A representative HB ring structure found in the first interfacial layer is shown in Fig. 3b. The SDFs represent the density distribution of oxygen and deuterium atomic positions; thus they reveal how water fills the space close to the surface. Deuterium and oxygen atoms are not uniformly distributed on top of the surface. Oxygen preferentially resides on top of the center of the hexagonal carbon rings (red isosurface). Some deuterium atoms tend to point towards the surface, as indicated in Fig. 1a-c. However, at variance with the case of a benzene molecule[42] in solution, the computed SDFs do not show any preference for the "dangling" H-bond to point towards the center of the carbon hexagons.

We note that the structural properties of interfacial water found in our *first principle* simulations are rather different from those obtained in the classical simulations we used to prepare the initial configurations for the first principle simulations. The water density oscillations are qualitatively similar in the two cases, but they are more pronounced in the first principle calculations. In particular, when a Lennard-Jones parameter of $\in_{CO}$ = 0.3135 kJ/mol (same as in Ref. 35) is used to describe the carbon-water interaction, the first interfacial layer of water in the classical simulations is less intense than in the first principle simulations. In order to have similar peak heights as in the first principles simulations, we found that much larger $\in_{CO}$ (~ 0.78 kJ/mol) are needed in the classical simulations. Subtle but important differences between the classical and first principle simulations can also be found in the spatial

arrangement of water molecules in the interfacial layer. Specifically, in the classical case we did not find a strong preference to orient OH bond towards the surface, as in the first principle simulations. More interestingly, we found that the SDFs of the interfacial layer are uniform in classical simulations and do not exhibit the peculiar structuring shown in Fig. 3.

Dynamical properties **---**We first analyze the Fourier transform of the deuterium atoms velocity autocorrelation function (Fig. 4), which is related to the vibrational spectra of our samples. Calculations of IR spectra will be reported elsewhere[46]. As shown in Fig. 4, for both graphene sheets and CNTs, a peak appears at frequencies higher than in the bulk spectrum (2600 cm^{-1}), in the region of the OD stretching mode. This signal is related to OD groups not involved in HBs; these OD bonds are likely to vibrate at a frequency higher than OD groups in a bulk environment and in early experimental work on the characterization of interfacial water their presence has been interpreted as a signal of surface hydrophobicity[55]. A similar feature in the power spectrum of confined water was observed by Martì *et al*.[26] and it was ascribed exclusively to confinement effects. In particular, it was interpreted as arising from the splitting of the symmetric and antisymmetric components of the OH stretching mode, accompanied by a shift of the stretching frequency to gas phase values (higher than in the bulk). With the aim of discerning between confinement and surface effects, we artificially cut our water samples in layers of increasing distance from the interface, and we calculated the power spectra of each layer. We found that the peak at 2600 cm^{-1} is mainly related to water molecules in close proximity with the surface, with non hydrogen-bonded OD bonds likely pointing towards the graphene layer. The water layer in the middle of the slab shows instead a power spectrum similar to that of the bulk liquid. This suggests that the peak at 2600 cm^{-1} is mainly due to a surface effect and confirms the locality of the perturbation induced by the surface on water, as observed in our structural analysis. We note that confinement enhances the high frequency power spectrum signal, as it increases the surface to volume ratio of the liquid. We believe this is the reason why the high frequency peak is more pronounced in the power spectra of CNT than in that of graphene sheets.

Another interesting region of the power spectrum of Fig. 4 is the band at low frequencies (120-800

cm^{-1}) that is usually assigned to librational modes, and thus related to inter-molecular hydrogen bonds. This band appears to undergo a red shift in the most confined samples, indicating a weakening of the HB strength in the interfacial region. However the simulation times available here do not permit quantitative conclusions on the shifts observed in the low frequency part of the spectrum. The band at 1178 cm^{-1}, related to the water molecule bending mode, is mostly unchanged in all of our samples.

In order to investigate molecular self-diffusion, we calculated the mean square displacement (MSD) of the oxygen in the direction parallel to the interface in the case of graphene and along the CNT axes. The MSD is related to the self-diffusion coefficient (D) through the Einstein relation, using the appropriate normalization factor for mono and two dimensional diffusion processes. Our results show that the lateral diffusion constant of water increases at extreme confinement. In particular, in the case of flat surfaces (graphene), diffusion increases with decreasing interlayer separation, becoming almost three times larger than that calculated for the bulk (1.0×10^{-5} cm^2/s), for a distance of 10.09 Å. This increase is significant and well outside the error bar on our diffusion constants, estimated to be 20-30% (see Method Section). In the case of CNTs, this effect appears to be enhanced, although it is not possible to establish a trend as a function of the tube radius from only two systems. At a diameter of 15.00 Å the diffusion constant reaches about 3×10^{-5} cm^2/s, which again is significantly different from that of bulk deuterated water. When decreasing the CNT radius to 11.10 Å, the diffusion constant slightly decreases, however remaining larger than the bulk value. In the case of two-dimensional confinement, for a CNT diameter smaller than an optimal value, the translational motion of water molecules may become so constrained that the diffusion constant does not increase as the radius decreases, unlike the case of graphene sheets.

Additional information on dynamical properties can be extracted from the re-orientational dynamics of the molecular dipole vector ($\boldsymbol{\mu}$), obtained from the correlation function $\Gamma = \langle \boldsymbol{\mu}(0) \cdot \boldsymbol{\mu}(t) \rangle$. The dipole vector of each molecule ($\boldsymbol{\mu}$) was calculated by assigning a charge of –2 to the oxygen atoms and charges of +1 to the deuterium atoms (geometrical dipole). This function, reported in Fig. 5, is characterized by an exponential decay (faster decay is associated with faster reorientation). Interestingly, we found that

the rotational motion of confined water molecules is faster than in the bulk phase, indicating that HBs are formed and broken at an increased rate. Indeed, H-bond lifetime calculated for the confined water samples show decay faster than bulk water, at variance with the results of Ref. 1 where HB lifetime under confinement where found to be substantially larger than in the bulk. Our results are consistent with weaker intermolecular HBs found in the interfacial regions. In particular, from Fig. 5 it appears that for both the CNTs and graphene layers separated by 14.41 Å, the relaxation time is almost identical, while it substantially decreases, becoming very close to that in the bulk, in the case of graphene at 25.02 Å. We repeated a similar analysis on the trajectories obtained with a classical potential (rigid SPC/E water model, see method section) and obtained the opposite result: water molecule reorientation appears hindered at increasing confinement. However we note that Marti, *et al*.[25] using a flexible SPC model did find an increased lateral diffusion of water under confinement, consistent with our results.

The faster dynamics obtained in our *first principle* simulations may be related to the magnitudes of the dipoles associated with the water molecules. These significantly decrease in the interfacial regions. The dipole moments were calculated using maximally localized Wannier function centers[57], by averaging over configurations extracted from our MD trajectories, and equally spaced in time. In the case of the bulk liquid the average molecular dipole moment calculated from MD trajectories is about 3.10 D. For graphene sheets and CNT, we found that the average dipole moment is always lower than in the bulk except for the 2.5 nm separation case where it has about the same value. Interestingly, the dipole significantly decreases within the interfacial layer assuming values of about 2.6-2.7 D for water molecules closer to the surface, while it is close to the bulk value in the liquid outside the interfacial regions. For the two CNT considered here the dipole moment remains lower than in the bulk in the whole confined sample, and the average dipole moment of the two confined systems is 2.87 and 2.93 D for the (14x0) and (19x0) CNT, respectively. In the case of a previously studied hydrophilic substrate (hydroxilated silicon carbide[56]) the lateral diffusion of water in the interfacial layer was substantially unmodified, with respect to the bulk, and correspondingly the average dipole moment of interfacial water molecules was very close to that of the bulk. On the other hand, in our study of water confined

between deuterated diamond surfaces[46], we observed a lateral diffusion enhanced, with respect to that found for the graphene case, and a smaller dipole moment of interfacial water molecules.

The variation of dipole moment magnitudes within the confined sample and with respect to the bulk may explain why rigid, non-polarizable classical models (e.g. SPC/E) do not predict fast molecular reorientation. The parameters of these models (like many others) are fitted to reproduce bulk liquid properties and it is thus not surprising that they do not account for the subtle interfacial rearrangement observed in our *first principle* simulations. Flexible and polarizable models may improve the description of the structural and dynamical properties of confined water, however the parameters entering the models may need fine tuning to describe how the strength of HB varies within a specific confined environment.

IV. SUMMARY AND CONCLUSIONS

The structural and dynamical properties reported in the previous section all consistently show that the perturbation of the confining surfaces on liquid water is localized within a 5 Å interfacial layer, whose thickness and microscopic structure do not depend on surface separation. The local nature of the perturbation found here is consistent with many results reported in the literature for bulk water in contact with both hydrophilic and hydrophobic surfaces and for complex surfaces, such as proteins[11].

This locality of the perturbation is also in agreement with the results of ultra fast optical Kerr spectroscopy reported by Scodinu *et al.*[58] for water confined in hydrophilic and hydrophobic nanopores. However Kim *et al.*[59] reported that for water in contact with organic monolayers, they find an interface layer extending up to 5 nm.

The interfacial layer found in our simulations is composed of a region of about 2.5 Å of zero particle density, followed by a region with particle density higher than in the bulk. Overall, the average density in the 5 Å interfacial layer is lower than in the bulk. In spite of an increased density of molecules outside the excluded volume, in proximity of the surface, water mobility is increased with respect to that

of the bulk. This appears to be related to a decrease of the molecular dipole moment and a weakening of HBs at the interface. These results are consistent with those reported in the case of water in the cavities of a hydrophobic zeolite[60], although the simulation time reported in Ref. 60 was rather short (3 ps) and an analysis of interfacial properties was not provided. The model of confined water emerging from our simulations –highly inhomogeneous, mobile interfacial layer surrounding a liquid which recovers bulk-like characteristic just outside a thin, ~ 0.5 nm, surface region-- is rather different from that proposed by Kolesnikov *et al.*[17]. However this study was conducted at much lower temperatures. These authors reported molecules frozen along the interior of a CNT wall in a four-fold coordinated square-ice pattern. These results were obtained using MD with classical potentials for CNTs very similar to the (19x0) case considered here, and they were used to interpret neutron scattering experiments. While our *first principle* MD results differ from the ones of Ref. 17, we note that our computed power spectrum is consistent with the generalized vibrational density of states obtained experimentally by the same authors, showing a blue shifted stretching band and a red shifted librational band. The structural model of confined water found here also differs from that obtained in another classical simulation by Byl *et al.*[61] The authors attribute their measured high-frequency infrared active mode to inter-ring OH groups different from those present in bulk water, and they propose the existence of a novel confined water phase with unusual HBs. According to our simulations the difference in HB between confined and bulk water mainly pertains to molecules within a thin interfacial layer and it does not stem from novel, liquid phases.

As mentioned in the Introduction, the mobility and in general the dynamics of confined water have received controversial interpretations in the literature. Recent flow experiments in CNTs with diameter of 2 nm or less reported by Holt *et al.*[4] showed enhanced flow at the nanoscale; these results are consistent with the enhanced lateral diffusion suggested by our simulations. However, the enhancement by orders of magnitude found in Ref. 4 is difficult to explain based on our finding of a moderate increase in the liquid self-diffusion coefficient, and viscosity calculations would be necessary to reach

firm conclusions on flow rates. Other experiments reported instead a slower dynamics in nanotubes. Naguib *et al*.[12] interpreted some of their TEM results on water confined in multi-wall CNTs as showing a decreased mobility of the liquid inside the tubes.

In the field of classical MD simulations, recent results obtained on mica by Leng *et al*.[62] for water dynamics are consistent with ours, while several other authors have reported a decreased mobility (e.g. Mashl *et al*.[6]) for water in nanotubes. Faster diffusion has been predicted in the case of very small nanotubes in Refs. 1-3, where one chain of water molecules was present and, for larger tube diamaters, by Martì *et al*.[25] who employed a flexible SPC model to describe confined water. When using classical potentials, water-water and water-surface interactions are not usually treated on the same footings. For example, Pertsin *et al*.[33] have shown that different water-graphite potentials may yield rather different structures in the interfacial region, although thermodynamic properties may be less affected by the presence of confining surfaces, as discussed in Ref. 63. In addition, classical potentials are usually fitted to bulk properties and they are thus unlikely to account for subtle but important effects, such as the decrease of interfacial water molecule dipole moments and electronic structure re-arrangements at the surface. Our results point at the need for at least flexible and possibly polarizable models, in order to describe water confinement effects in a realistic manner.

ACKNOWLEDGMENT

We thank D. Prendergast, T. Ogitsu and M.Sharma for many useful discussions. Part of this work was performed under the auspices of the U.S. Department of Energy by Lawrence Livermore National Laboratory under contract No. DE-AC52-07NA27344. Use of the computing facilities at the Lawrence Livermore National Laboratory (LLNL) is gratefully acknowledged.

FIGURES

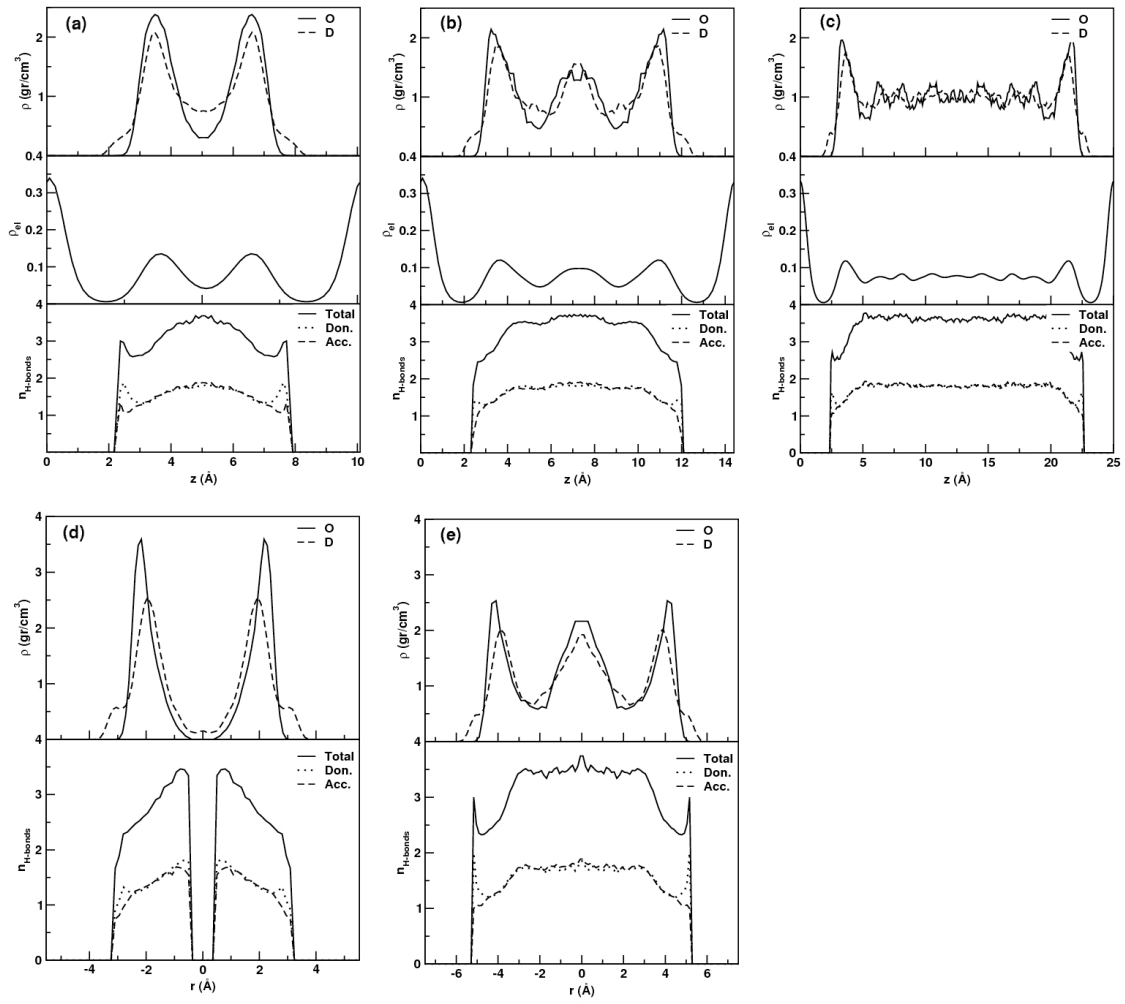

Figure 1. The top panels of a), b) and c) show the density of water molecules computed along the direction perpendicular to graphene confining surfaces (the continuous and dashed curves represent oxygen and deuterium atoms, respectively) for three confining lengths [a), 10.09 Å; b), 14.41 Å and c) 25.02 Å; see text]. The middle and bottom panels show the valence electronic charge density and the average number of water-water hydrogen bonds, respectively, corresponding to the three confining lengths. The curves in the bottom panels display the number of H-bond donor (dotted line) and acceptor (dashed line) for each water molecule; the total number of hydrogen bonds per molecule is also reported as a continuous black line. We choose the following geometric criterion to define a hydrogen bond:

O···O distance shorter than 3.5 Å and O···HO angle larger than 140°. The top and bottom panels of d) and e) show the water density and number of hydrogen bonds in the case of carbon nanotubes with diameter of 11.10 and 15.00 Å, respectively.

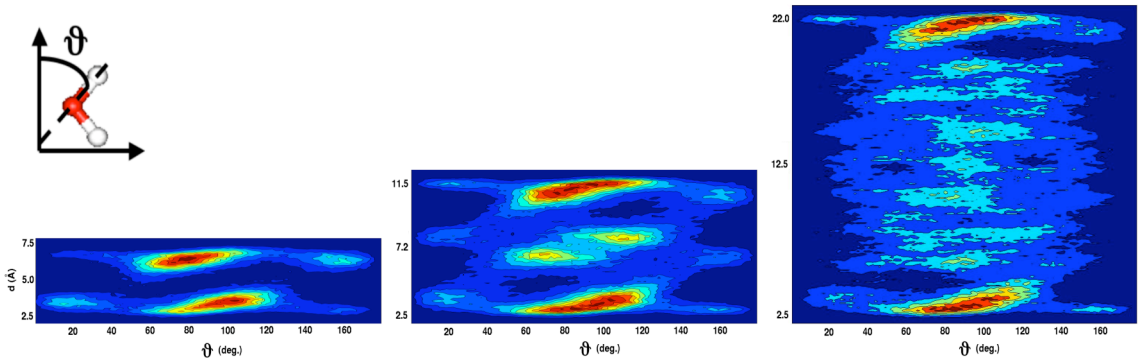

Figure 2. Tilt angle distribution for water molecules confined within graphene sheets, for the three confining lengths defined in Fig. 1. The tilt angle is defined with respect to the direction perpendicular to the surface. See inset for the definition of the tilt angle.

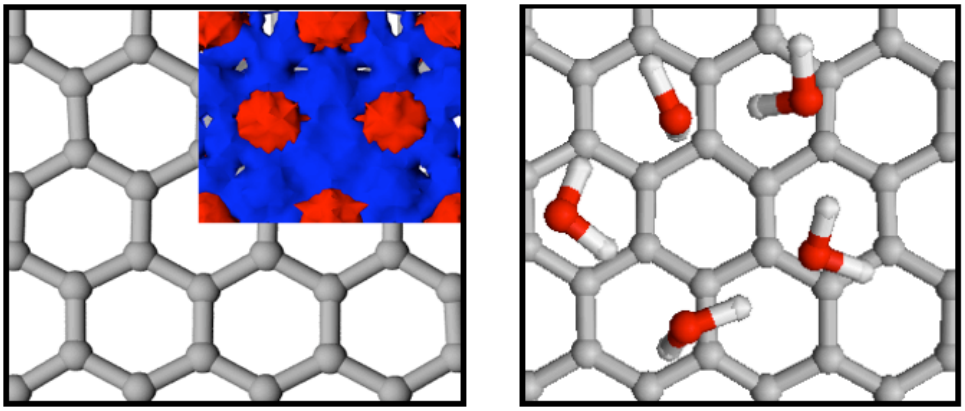

Figure 3. The left panel shows the oxygen (red isosurface) and deuterium (blue isosurface) spatial distribution function (SDF) of water molecules confined within graphene sheets at a distance of 14.41 Å (see also Fig.1b). These SDFs represent the density distribution of oxygen and deuterium atom positions in a layer within 5 Å from the graphene surface. The right panel contains a ball and stick representation of the water molecules at the interface for a representative snapshot of our MD trajectories. Red, white

and grey spheres represent oxygen, deuterium and carbon atoms, respectively. The restructuring of water close to the interface is responsible for the appearance of novel ring structures under confinement. In particular, the probability of finding 4-fold and 5-fold rings increases and that of finding 6-fold ones decreases, with respect to the bulk. [For a discussion of ring statistics around hydrophobic groups see, e.g. Ref. 64].

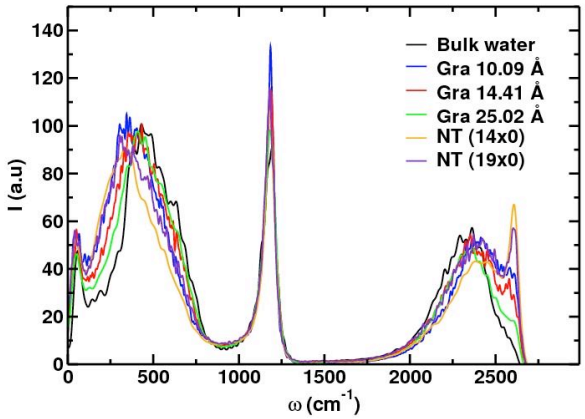

Figure 4. Comparison of the power spectra of the velocity-velocity autocorrelation function for all the confined water samples considered in this work. The power spectrum of bulk water is also reported for comparison.

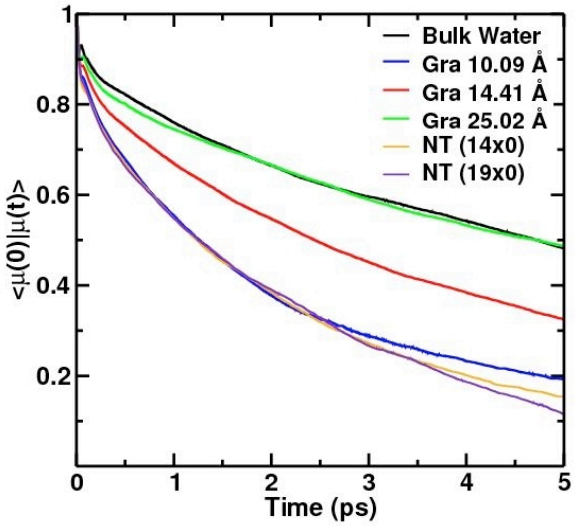

Figure 5. Water dipole rotational autocorrelation function for all the water samples considered here (see text), as obtained from *first principle* MD simulations. The relative dipole rotational autocorrelation functions of bulk water are also reported for comparison. Given the statistical error bars of our simulations (over ~ 20 ps runs), we can only make the observation that the autocorrelation functions for the 2.5 nm separation case is similar to the bulk case, but not exactly establish whether it has already reached the bulk value. It is instead clear that the correlation functions for smaller separations are decaying faster than in the bulk case (see text).

TABLES

System	d (Å)	N(D_2O)	t (ps)
Graphene	10.09	32	25
Graphene	14.41	54	20
Graphene	25.02	108	10
NT (14x0)	11.10	34	20
NT (19x0)	15.00	54	20

Table 1. For each simulation performed in this work, the confining length (d), the number of D_2O molecules (N) and the total simulation time t (ps) are given. In the case of graphene d represents the distance between the confining sheet, and in the case of nanotubes, it represents the diameter. All simulations are Born-Oppenheimer molecular dynamics simulations carried out using Density Functional Theory, with the PBE functional.

REFERENCES.

1. Hummer, G.; Rasaiah, J. C.; Noworyta, J. P. *Science* **2001**, *414*, 188.

2. Maibaum, L.; Chandler, D. *J. Phys. Chem. B* **2003**, *107*, 1189.

3. Beckstein, O; Sansom, M. S. P. *Proc. Nat'l Acad. Science* **2003**, *100*, 7063.

4. Holt, J. K.; Park, H. P.; Waang, Y.; Stadermann, M.; Artyukhin A-B.; Grigopoupulos, C. P.; Noy, A.; Bakajin, O. *Science* **2006**, *312*, 1034.

5. Majumder, M.; Chopra, N.; Andrews, R.; Hinds, B. J. *Nature* **2005**, *438*, 44.

6. Mashl, R-J.; Joseph, S.; Aluru, N-R.; Jakobsson, E. *Nano Lett.* **2003**, *3*, 589.

7. Koga, K.; Gao, G-T.; Tanaka, H.; Zeng, X. C. *Science* **2001**, *412*, 802.

8. Chandler, D. *Nature* **2005**, *437*, 640, and references therein.

9. Bellissent M.-C. *J. Mol. Liq.* **2002**, *96-97*, 287.

10. Cheng, L.; Fenter, P.; Nagy, K. L.; Schlegel, M. L.; Sturchio, N. C. *Phys. Rev. Lett.* **2001**, *87*, 156103.

11. Bagchi B. *Chem. Rev.* **2005**, *105*, 3197.

12. Naguib, N.; Ye, H.; Gogotsi, Y.; Yazicioglu, A. G.; Megaridis, C. M.; Yoshimura, M. *Nano Lett.* **2004**, *4*, 2237.

13. Major, R. C.; Houston, J. E.; McGrath, M. J.; Siepmann, J. I.; Zhu, X. Y. *Phys. Rev. Lett.* **2006**, *96*, 177803.

14. Raviv, U.; Laurat, P.; Klein, J. *Nature* **2001**, *413*, 51.

15. Raviv, U.; Klein, J. *Science* **2002**, 297, 1540.

16. Koga, K.; Gao, G. T.; Tanaka, H.; Zeng, X. C. *Physica A* **2002**, *314*, 462.

17. Kolesnikov, A. I.; Zanotti, J. M.; Loong, C. K.; Thiyagarajan, P.; Moravsky, A. P.; Loutfy R. O.; Burham, C. J. *Phys. Rev. Lett.* **2004**, *93*, 035503.

18. Ghosh, S.; Ramanathan K. V.; Sood, A. K. *Europhys. Lett.* **2004**, *65*, 678.

19. Zangi, R.; Mark, A. E. *Phys Rev. Lett.* **2003**, *91*, 025502.

20. Zangi, R.; Mark, A. E. *J. Chem. Phys.* **2003**, *119*, 1694.

21. Hirunsit, P.; Balbuena, P. B. *J. Phys. Chem. C* **2007**, *111*, 1709.

22. Rahman, A.; Stillinger, F. H. *J. Chem. Phys.* **1971**, *55*, 3336.

23. Jorgensen, W. L.; Chandrasekhar, J.; Madura, J. *J. Chem. Phys.* **1983**, 79, 926.

24. Martì, J.; Gordillo, M. C. *Chem. Phys. Lett.* **2000**, *329*, 341.

25. Martì, J.; Gordillo, M. C. *Phys. Rev. E* **2000**, *64*, 021504.

26. Martì, J.; Gordillo, M. C. *Phys. Rev. B* **2001**, *63*, 165430.

27. Gordillo, M. C.; Nagy, G.; Martì, J. *J. Chem. Phys.* **2005**, *123*, 054707.

28. Martì, J.; Nagy, G.; Gordillo, M. C.; Guardia, E. *J. Chem. Phys.* **2006**, *124*, 094703.

29. Liu, Y.; Wang, Q.; Wu, T.; Zhang, L. *J. Chem. Phys.* **2005**, *123*, 234701.

30. Liu, Y.; Wang, Q. *Phys. Rev. B* **2005**, *72*, 085420.

31. Hanasaki, I.; Nakatani, A. *J. Chem. Phys.* **2006**, *124*, 174714.

32. Choudhury, N.; Pettitt, B. M. *J. Phys. Chem. B* **2005**, *109*, 6422.

33. Pertsin, A. ; Grunze, M. *J. Phys. Chem B* **2004**, *108*, 1357.

34. Berendsen, J. C.; Grigera, J. R.; Straatsma, T. P. *J. Phys. Chem.* **1987**, *91*, 6269.

35. Werder, T.; Walther, J. H.; Jaffe R. L.; Halicioglu, T.; Noca, F.; Koumoutsakos, P. *Nano Lett.* **2001**, *1*, 697.

36. Hohenberg, P.; Kohn, W. *Phys. Rev.* **1964**, *136*, B864.

37. Kohn, W.; Sham, L. J. *Phys. Rev.* **1965**, *140*, A1133.

38. Perdew, J. P.; Burke, K. ; Ernzerhof, M. *Phys. Rev. Lett.* **1996**, *77*, 3865.

39. Hamann, D. *Phys. Rev. B* **1989**, *40*, 2980.

40. Grossman, J. C.; Schwegler, E.; Gygi, F.; Galli, G. *J. Chem. Phys.* **2004**, *120*, 300.

41. Schwegler, E.; Grossman, J. C.; Gygi, F.; Galli, G. *J. Chem. Phys.* **2004**, *121*, 5400.

42. Allesch, M.; Schwegler, E.; Galli, G. *J. Phys. Chem. B* **2007**, *111*, 1081.

43. Chen, B.; Ivanov, I.; Klein, M. L.; Parrinello M. *Phys. Rev. Lett.* **2003**, *91*, 215503.

44. Wang, C. Z.; Chan C. T.; Ho K. M. *Phys Rev. B* **1990**, *42*, 11276.

45. Porter, L. J.; Li J., Yip S. *Nucl. Mater.* **1997**, *246*, 53.

46. M. Sharma, *private communication*.

47. Birkett, G. R.; Do, D. D. *J. Phys. Chem. C* **2007**, *111*, 5735.

48. A general purpose *first principle* Molecular Dynamics code, F. Gygi, 1998-2007 (UCD).

49. A *first principle* Molecular Dynamics code, F.Gygi, 1998-2003 (LLNL).

50. Gygi, F.; Fattebert J. L.; Schwegler, E. *Comput. Phys. Commun.* **2003**, *155*, 1.

51. See: www.gromacs.org

52. Lee, S. H.; Rossky, P. J. *J. Chem. Phys.* **1994**, *100*, 3334.

53. Lee, C. Y.; McCammon J. A.; Rossky P. J. *J. Chem. Phys.* **1984**, *80*, 4448.

54. Poyron, A.; Hong, L.; Robinsin, I. K.; Granick S.; Zhang, Z.; P. A. Fenter *Phys. Rev. Lett.* **2006**, *97*, 266101.

55. Du, Q.; Freysz, Y.; Shen Y. R. *Science* **1994**, *264*, 826.

56. Cicero, G.; Grossman, J. C.; Catellani, A.; Galli, G. *J. Am. Chem. Soc.* **2005**, *127*, 6830.

57. Marzari, N.; Vanderbilt, D. *Phys. Rev. B* **1997**, *56*, 12847.

58. Scodinu, A.; Fourkas, J. T. J. *Chem. Phys. B* **2002**, *106*, 10292.

59. Kim, H. I.; Kushmmerick, J. G.; Houston, J. E.; Bunker, B. C. *Langmuir* **2003**, *19*, 9271.

60. Coudert, F. X.; Vuilleumier, R.; Boutin, A. *Chem. Phys. Chem.* **2006**, *7*, 2464.

61. Byl, O.; Liu, J. C.; Wang, Y.; Yim, W. L.; Johnson, J. K.; Yates, J. T. *J. Am. Chem. Soc.* **2006**, *128*, 12090.

62. Leng, Y.; Cummings, P. T. *Phys. Rev. Lett.* **2005**, 94, 026101.

63. Kumar, P.; Starr, F. W.; Buldyrev, S. V.; Stanley, H. E. *Phys. Rev. E.* **2007**, *75*, 011202.

64. Head-Gordon, T. *Proc. Nat'l. Acad. Soc.* **1995**, *92*, 8308.

TOC grafic:

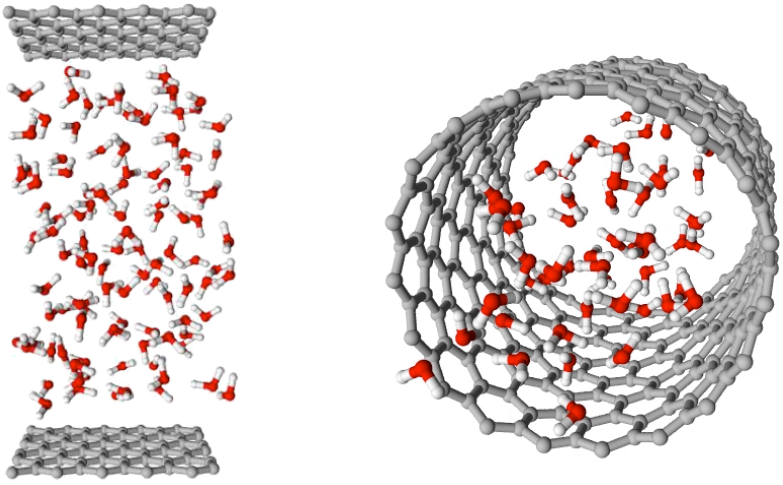

LLNL-JRNL-408883

LAWRENCE
LIVERMORE
NATIONAL
LABORATORY

Water confined in carbon nanotubes: Magnetic response and proton chemical shieldings

P. Huang, E. Schwegler, G. Galli

November 14, 2008

Journal of Physical Chemistry

Disclaimer

Auspices Statement

This work performed under the auspices of the U.S. Department of Energy by Lawrence Livermore National Laboratory under Contract DE-AC52-07NA27344. This work was funded by the Laboratory Directed Research and Development Program at LLNL under project tracking code 06-ERD-039.

Water confined in carbon nanotubes: Magnetic response and proton chemical shieldings

Patrick Huang,[*,†] Eric Schwegler,[†] and Giulia Galli[‡]

Physics and Life Sciences Directorate, Lawrence Livermore National Laboratory, 7000 East Ave., Livermore, CA 94551, and Department of Chemistry, University of California, One Shields Ave., Davis, CA 95616

E-mail: huang26@llnl.gov

February 25, 2009

Abstract

We study the proton nuclear magnetic resonance (^{1}H-NMR) of a model system consisting of liquid water confined in carbon nanotubes (CNT). Chemical shieldings are evaluated from linear response theory, where the electronic structure is derived from density functional theory (DFT) with plane-wave basis sets and periodic boundary conditions. The shieldings are sampled from trajectories generated via first-principles molecular dynamics simulations at ambient conditions, for water confined in (14,0) and (19,0) CNTs with diameters $d = 11$ Å and 14.9 Å, respectively. We find that confinement within the CNT leads to a large (~ -23 ppm) *upfield* shift relative to bulk liquid water. This shift is a consequence of strongly anisotropic magnetic fields induced in the CNT by an applied magnetic field.

[†]Lawrence Livermore National Laboratory
[‡]University of California, Davis

The complex behavior of water in nanoscale cavities, channels, and interfaces is fundamental to a broad range of phenomena, and can be quite different from bulk phases. In particular, single-walled carbon nanotubes (CNT) provide a well-defined environment to study confinement effects,[1] and serve as a model for more complicated systems, *e.g.*, biological membrane channels. Novel nanoscale properties of water confined to CNT channels include the experimental observation of fast water transport[2] and ion exclusion,[3] demonstrating the potential of CNT-based materials for advanced nanofluidic applications.

Simulations have been crucial in elucidating the microscopic origins of such unusual phenomena.[4] However, simulations are subject to a certain number of assumptions; in particular, approximations are made in the modeling of interatomic forces. Most theoretical work on confined water so far have relied on semiempirical model potentials that are fit to reproduce known bulk properties. As such, the applicability to confined water may be questionable. Strategies where interatomic forces are evaluated from first principles electronic structure methods instead of model potentials can provide a more unbiased picture, without input from experiment. At present, such calculations are expensive, and limited to water confined to narrow ($d < 1.5$ nm) CNTs for short (≤ 20 ps) time scales.[5] Therefore, progress requires exchange between theory and experiment, and it is essential to relate theoretical models to experimentally accessible observables that can be tested and validated in the laboratory.

One important class of observables is nuclear magnetic resonance (NMR), whose use in the structural studies of molecules and proteins is well-established. NMR techniques can resolve the different resonance frequencies of non-equivalent nuclei, thus providing a detailed, atomic-scale probe of the local electronic structure. The relaxation of nuclear spins contains information about rotational and diffusional correlation times, and is sensitive to local ordering (*i.e.*, solid versus liquid). This feature has been exploited to track the onset of freezing in CNT-confined water.[6–8] Unfortunately, it is difficult to prepare clean, uniform CNT samples for high resolution measurements. Usually, CNT samples contain a mixture of semiconducting and metallic nanotubes with different diameters and chiralities. Defects can be present at non-negligible concentrations, depending on

the preparation conditions. In addition, CNTs are often contaminated with the transition metal catalysts employed in their synthesis, and the presence of such paramagnetic impurity centers lead to large inhomogeneous broadenings in NMR spectra.

It is therefore not surprising that there are significant discrepancies among NMR studies of water in CNTs. The ^{1}H-NMR chemical shift associated with confined water in CNTs has been reported at values ranging from around $+8$ ppm downfield to -15 ppm upfield relative to the bulk water proton resonance.[6–9] Given the uncertainty in the experiments, it is important to establish a theoretical baseline value for the ^{1}H-NMR signature of confined water in well-defined systems. To this end, we evaluate the ^{1}H-NMR chemical shielding tensors for water in infinite, defect-free CNTs, with diameters $d = 11$ Å and 14.9 Å. These diameters are chosen to represent the range of average diameters reported in the ^{1}H-NMR experiments on CNT-confined water. The shieldings are compared to the proton shieldings for bulk water under standard conditions, which is an important test case of our methodology, and serves as a point of reference for the study of confinement effects. Our results indicate that the interior of the CNTs induces a significant upfield shift for confined water as compared to bulk liquid water, in qualitative agreement with the most recent experiments.

Theory and computational details. The application of a uniform magnetic field $\mathbf{B}_0$ to atoms and molecules induces an inhomogeneous electron current density $\mathbf{J}_{\rm ind}(\mathbf{r})$. From classical magnetostatics, the induced field $\mathbf{B}_{\rm ind}(\mathbf{r})$ generated by this current is given by the Biot-Savart law:

$$\mathbf{B}_{\rm ind}(\mathbf{r}) = \frac{1}{c}\int d\mathbf{r}'\,\mathbf{J}_{\rm ind}(\mathbf{r}')\times\frac{\mathbf{r}'-\mathbf{r}}{|\mathbf{r}'-\mathbf{r}|^3}. \tag{1}$$

We consider the linear response to the external field, so that the induced field can be expressed as

$$\mathbf{B}_{\rm ind}(\mathbf{r}) = -\boldsymbol{\sigma}(\mathbf{r})\cdot\mathbf{B}_0. \tag{2}$$

The tensor $\boldsymbol{\sigma}(\mathbf{r})$ characterizes the shielding of $\mathbf{B}_0$ by the electrons, and reflects the details of the local electronic structure. NMR probes $\boldsymbol{\sigma}(\mathbf{r})$ at nuclear positions $\mathbf{r} = \mathbf{r}_{\rm X}$; in this case, it is referred

to as the chemical shielding tensor associated with nuclei X.

For periodic systems, $\mathbf{J}_{\rm ind}(\mathbf{r})$, $\mathbf{B}_{\rm ind}(\mathbf{r})$, and $\boldsymbol{\sigma}(\mathbf{r})$ are periodic functions of $\mathbf{r}$, and so it is more convenient to work in their Fourier representations. The $\mathbf{G} \neq 0$ Fourier components of $\mathbf{B}_{\rm ind}(\mathbf{r})$ are evaluated from Eq. (1) as

$$\widetilde{\mathbf{B}}_{\rm ind}(\mathbf{G} \neq 0) = i\frac{4\pi}{c}\frac{\mathbf{G}}{|\mathbf{G}|^2} \times \widetilde{\mathbf{J}}_{\rm ind}(\mathbf{G}), \tag{3}$$

and substituting into the Fourier transform of Eq. (2) gives the $\mathbf{G} \neq 0$ components of the shielding tensor. The $\mathbf{G} = 0$ component is handled separately, for the evaluation of $\widetilde{\mathbf{B}}_{\rm ind}(\mathbf{G} = 0)$ involves an integration of $\mathbf{B}_{\rm ind}(\mathbf{r})$ over the entire volume of the macroscopic sample, which requires the specification of its shape. A common choice is a spherical sample, so that

$$\widetilde{\mathbf{B}}_{\rm ind}(\mathbf{G} = 0) = 4\pi\alpha\chi_v \cdot \mathbf{B}_0, \tag{4}$$

where α is a diagonal tensor with $\alpha_{xx} = \alpha_{yy} = \alpha_{zz} = 2/3$, and χ_v is the magnetic volume susceptibility tensor.[10] For a cylindrical sample with the cylinder axis along the z-direction, $\alpha_{xx} = \alpha_{yy} = 1/2$ and $\alpha_{zz} = 1$. The $\mathbf{G} = 0$ Fourier component of $\boldsymbol{\sigma}(\mathbf{r})$ is thus

$$\widetilde{\boldsymbol{\sigma}}(\mathbf{G} = 0) = -4\pi\alpha\chi_v. \tag{5}$$

While the accurate quantum chemical evaluation of chemical shielding tensors of small molecules is now considered to be routine, only within this last decade have methods emerged that can treat the magnetic response of extended systems under 3D periodic boundary conditions. Here, we evaluate $\boldsymbol{\sigma}(\mathbf{r})$ in the above periodic formulation, using the gauge-included projector augmented wave (GIPAW) method[11] as implemented in the QUANTUM-ESPRESSO[12] suite of plane-wave electronic structure codes. The GIPAW method is based on earlier work by Mauri *et al.* on the evaluation of the magnetic susceptibility χ_v and chemical shielding tensor $\boldsymbol{\sigma}(\mathbf{r})$ within the pseudopotential approximation.[10,13] GIPAW goes beyond pseudopotentials to obtain $\boldsymbol{\sigma}(\mathbf{r})$ with an all-electron, frozen core treatment.

In short, the GIPAW procedure begins with the zeroth-order electronic wavefunctions $\{\psi_n^{(0)}\}$ in the absence of $\mathbf{B}_0$. In the present case, we use Kohn-Sham density functional theory (DFT) with the PBE approximation[14] for exchange-correlation, using a plane-wave basis set truncated at $E_c = 70$ Ry. For the systems of interest here, increasing this cutoff to $E_c = 85$ Ry only changes the shieldings by ~ 0.01 ppm. The first-order wavefunctions $\{\psi_n^{(1)}\}$ are then evaluated from the linear response to the perturbation due to the presence of $\mathbf{B}_0$, from which the induced current $\mathbf{J}_{\text{ind}}(\mathbf{r})$ is obtained. Finally, the induced field $\mathbf{B}_{\text{ind}}(\mathbf{r})$ and shielding tensor $\boldsymbol{\sigma}(\mathbf{r})$ are computed according to Eqs. (1)–(5). Since the focus of this work is on ^{1}H-NMR chemical shieldings, from this point on $\boldsymbol{\sigma} = \boldsymbol{\sigma}(\mathbf{r}_{\text{H}})$ unless otherwise noted.

In a liquid, molecules are tumbling rapidly relative to typical NMR timescales ($\sim 10^{-6}$ s) and so one effectively measures an orientationally-averaged, isotropic shielding,

$$\sigma_{\text{iso}} = \frac{1}{3}\text{Tr}[\boldsymbol{\sigma}]. \tag{6}$$

The most immediate quantity from NMR is the chemical shift δ, which is a difference in isotropic shieldings,

$$\delta = \sigma_{\text{iso}}^{\text{ref}} - \sigma_{\text{iso}}, \tag{7}$$

where $\sigma_{\text{iso}}^{\text{ref}}$ is the shielding at nuclei X in some reference compound, and σ_{iso} is the shielding of the same nuclei X in the compound of interest. A positive (downfield) shift means the nuclei of interest is *less* shielded than the reference, while a negative (upfield) shift means the nuclei of interest is *more* shielded than the reference. The chemical shielding anisotropy $\Delta\sigma$ is defined as

$$\Delta\sigma = \sigma_{11} - \frac{1}{2}\left(\sigma_{22} + \sigma_{33}\right), \tag{8}$$

where $\sigma_{11}, \sigma_{22}, \sigma_{33}$ are the principal values of the irreducible rank 1 tensor $\boldsymbol{\sigma}^{(1)} = \left(\boldsymbol{\sigma} + \boldsymbol{\sigma}^T\right)/2$, with $\sigma_{11} > \sigma_{22} > \sigma_{33}$.

Bulk liquid water. We consider bulk liquid water at ambient conditions as the reference state,

and compute ^{1}H chemical shieldings with a spherical susceptibility correction $\alpha = 2/3$ [Eq. (4)]. The thermally-averaged isotropic shielding $\langle\sigma_{\rm iso}^{\rm liq}\rangle$ is evaluated by averaging $\sigma_{\rm iso}$ of each water molecule over configurations from first-principles molecular dynamics (FPMD). We sample $N_c = 15$ configurations from an FPMD trajectory generated with classical Born-Oppenheimer dynamics, for $N = 64$ water molecules in a cubic box of size $a = 12.43$ Å. A simulation temperature of $T = 400$ K was used to partly mimic proton quantum effects at $T = 300$ K. Such a temperature rescaling was previously shown to yield radial distribution functions that are in good agreement with experiment at $T = 300$ K.[15,16] Statistical errors are estimated by averaging $\sigma_{\rm iso}$ of all protons in an individual FPMD configuration, and taking the population standard deviation of the set of configuration averages.

Our results are summarized in Table 1, and compared to previous theoretical bulk water studies under periodic boundary conditions, and experiment. Among the prior theoretical studies, the most direct comparison with ours is the work of Pfrommer *et al.*,[17] who use a DFT-based linear response approach similar to that employed here. However, there are differences in the underlying details, the most significant being the FPMD simulations used to generate the water configurations. Ref. 17 averages over $N_c = 9$ configurations sampled from the Car-Parrinello simulation of Sprik *et al.*,[18] which was performed for a smaller box of $N = 32$ water molecules at $T = 300$ K. There, a rather large value of $\mu = 1100$ a.u. was chosen for the fictitious electron mass that is needed in the Car-Parrinello scheme. Despite these differences, our result for $\langle\sigma_{\rm iso}^{\rm liq}\rangle$ agrees closely with Ref. 17. While such excellent agreement may be somewhat fortuitous, it is not unreasonable as the underlying FPMD simulations in both cases give similar results for the overall liquid water structure.

Sebastiani and Parrinello[19] also use a DFT-based linear response approach, but there the magnetic perturbation under periodic boundary conditions is handled differently from this work and Ref. 17. The water configurations are generated by the CPMD simulations of Silvestrelli *et al.*,[21] which should be similar ($N = 32$, $T = 303$ K, $\mu = 900$ a.u.) to that used in Ref. 17. Ref. 19 does not report averaged absolute shieldings, only the gas-to-liquid shift.

Table 1: Thermally-averaged isotropic proton shielding $\langle\sigma_{\rm iso}^{\rm liq}\rangle$ and shielding anisotropy $\langle\Delta\sigma^{\rm liq}\rangle$ for bulk liquid water. Ref. 19 reports only the gas-to-liquid chemical shift $\delta = \sigma_{\rm iso}^{\rm gas} - \langle\sigma_{\rm iso}^{\rm liq}\rangle$. All shieldings are in units of ppm.

	$\langle\sigma_{\rm iso}^{\rm liq}\rangle$	δ	$\langle\Delta\sigma^{\rm liq}\rangle$
This work	24.3(3)		26.9(5)
Ref. 17	24.3(1)[a]	5.8(1)	
Ref. 19		5.2(2)	
Ref. 20 (expt.)	25.71(2)[b]		27.4(1)

[a]Converted to an absolute shielding using the reported value for the reference shielding $\sigma_{\rm iso}^{\rm gas}$. Ref. 17 evaluates the statistical error as the sample standard deviation of all proton shieldings over all configurations.

[b]Ref. 20 derives an absolute shielding using the chemical shift relative to CH_4 gas; see reference for details.

While changes in the isotropic shielding $\sigma_{\rm iso}$ are usually taken as qualitative signatures of hydrogen bonding, the shielding anisotropy $\Delta\sigma$ is a much more sensitive measure of hydrogen bond formation and geometry than $\sigma_{\rm iso}$.[22,23] For solids, high-resolution, solid-state NMR techniques can determine the orientation and principal values of the shielding tensor. These methods are not directly applicable to the liquid state, where information about the components of the shielding tensor is averaged out by molecular tumbling. To our knowledge, the only measurement of $\langle\Delta\sigma^{\rm liq}\rangle$ in liquid water is by Modig *et al.*, who extract $\langle\Delta\sigma^{\rm liq}\rangle$ from proton spin relaxation rates.[20] Average hydrogen bond distances and angles were subsequently inferred by fitting to a geometrical model relating the liquid structure to $\langle\sigma_{\rm iso}^{\rm liq}\rangle$ and $\langle\Delta\sigma^{\rm liq}\rangle$.[23]

Here, we evaluate $\langle\Delta\sigma^{\rm liq}\rangle$ by computing $\Delta\sigma$ for each proton from its instantaneous principal value, and then averaging the individual $\Delta\sigma$ over configurations. This averaging is done over the same $N_c = 15$ configurations used in the evaluation of $\langle\sigma_{\rm iso}^{\rm liq}\rangle$ above. The result is listed in Table 1, along with the experimental value from Ref. 20. While the ability of FPMD simulations to reproduce the correct radial structure in liquid water has been demonstrated, the good agreement seen between the theoretical and experimental value for $\langle\Delta\sigma^{\rm liq}\rangle$ confirms the ability of the FPMD to give the correct angular structure as well.

Water in carbon nanotubes. First-principles calculations for the magnetic response and ^{13}C-NMR chemical shifts of empty, infinite CNTs have been reported previously.[24–27] Here, we evaluate ^{1}H-NMR shieldings of water enclosed in semiconducting, zigzag (14,0) and (19,0) CNTs,

whose diameters are $d = 11.0$ Å and $d = 14.9$ Å, respectively. In order to isolate the effects of the nanotube, we begin by considering a single water molecule in a (14,0) CNT. The water/(14,0) nanotube system is modeled in a tetragonal supercell with lattice parameters $a = b = 17.0$ Å, and $c = 12.7607$ Å, which corresponds to three primitive nanotube unit cells along the c-axis, and 6 Å of vacuum between nanotubes. The susceptibility corrections to the chemical shieldings [Eq. (4)] are evaluated as $\alpha_{xx} = \alpha_{yy} = 1/2$ and $\alpha_{zz} = 2/3$. This choice was previously shown to yield the fastest convergence of the ^{13}C-NMR chemical shifts with respect to the inter-tube spacing,[26] which we have also verified here. Integration over the Brillouin zone is done using six k-points spaced $\Delta k = 0.04924$ Å^{-1} apart. These computational parameters are similar to those in Ref. 26 (except for the plane-wave basis cutoff E_c, which is necessarily higher here due to the presence of oxygen atoms), and yield ^{1}H-NMR shieldings that are converged to < 0.5 ppm.

For the calculations of a single water molecule inside a CNT, the water molecule is positioned with the oxygen at the CNT center, in two different orientations: one O-H bond oriented parallel to the tube axis, and both O-H bonds perpendicular to the tube axis. Table 2 lists the principal values for the proton shieldings, along with the isolated molecule values (*i.e.*, no CNT present). Upon encapsulation in a CNT, the most dramatic change is a $\delta \sim -22$ ppm upfield shift in $\sigma_{\rm iso}$, relative to the isolated molecule. This is quite large, considering that typical proton chemical shifts in small organic molecules are $\delta \sim 0-10$ ppm downfield relative to tetramethylsilane (TMS). The change in $\sigma_{\rm iso}$ upon encapsulation is at least an order of magnitude larger than changes due to intramolecular distortions, or the relative position of the molecule within the CNT. On the other hand, $\Delta\sigma$ is sensitive to the orientation of the water relative to the tube axis. Inside the CNT, the largest decrease in $\Delta\sigma$ (~ -9 ppm) occurs when the O-H bond is parallel to the tube axis, while the largest increase (~ 12 ppm) occurs when the O-H bond is perpendicular to the tube axis.

Similar behavior is also seen in the calculations of Besley and Noble for the proton chemical shifts of a variety of small molecules in CNTs. In general, they find upfield shifts relative to the isolated molecules, on the order of -13 ppm to -26 ppm for the zigzag CNTs.[28] However, we note that Ref. 28 examines finite, hydrogen-capped CNTs using molecular quantum chemical methods

Table 2: Principal values σ_{11}, σ_{22}, and σ_{33} of the proton shielding tensor, isotropic shielding σ_{iso}, and shielding anisotropy $\Delta\sigma$ for the water molecule. The three sets of values correspond to: no CNT present, one O-H bond parallel to the tube axis ($H_{\parallel}$), and both O-H bonds perpendicular to the tube axis ($H_{\perp}$). All shieldings are in units of ppm.

	σ_{11}	σ_{22}	σ_{33}	σ_{iso}	$\Delta\sigma$
No CNT:					
H	41.43	25.56	23.41	30.13	16.95
Parallel:					
$H_{\parallel}$	57.84	54.46	46.27	52.86	7.48
H	70.82	54.32	33.33	52.82	27.00
Perpendicular:					
$H_{\perp}$	72.62	56.45	29.43	52.83	29.68

with localized, Gaussian basis sets (gauge-including atomic orbitals method), while we consider here an infinite CNT with plane-wave basis sets. Zurek *et al.*[24] have made a direct comparison between ^{13}C-NMR shifts in capped and infinite CNTs, and found very slow convergence of the capped CNTs with respect to tube length; this is consistent with our own observations of finite-size effects on ^{1}H-NMR shifts in CNTs.

We see similar behavior in the thermally-averaged isotropic proton shielding $\langle\sigma_{\text{iso}}^{\text{liq}}\rangle$ for liquid-filled (14,0) and (19,0) CNTs. The (14,0) CNT contains 34 water molecules in a tetragonal supercell similar to the one used for the single water molecule calculations above, except with a longer length $c = 25.52$ Å. This corresponds to six primitive nanotube unit cells along the c-axis. The averaged isotropic shielding $\langle\sigma_{\text{iso}}^{\text{liq}}\rangle$ and shielding anisotropy $\langle\Delta\sigma^{\text{liq}}\rangle$ are evaluated by sampling $N_c = 12$ configurations from the FPMD simulation of Cicero *et al.*[5] As with bulk water, the FPMD simulations were run at $T = 400$ K. The liquid-filled (19,0) CNT is modeled similarly, except it contains 54 water molecules in a supercell with length $c = 17.06$ Å, corresponding to four primitive nanotube unit cells along the c-axis.

The results are summarized in Table 3. Like the single encapsulated molecule, the most noticeable effect in the confined liquid is the large upfield shift in $\langle\sigma_{\text{iso}}^{\text{liq}}\rangle$ relative to free bulk water. The difference in the averaged proton shielding between the 11 Å and 14.9 Å tubes is ~ 1.5 ppm, which is an order of magnitude smaller than the dominant effect of encapsulation within the CNT. The

Table 3: Thermally-averaged proton shielding $\langle\sigma_{\rm iso}^{\rm liq}\rangle$ and shielding anisotropy $\langle\Delta\sigma^{\rm liq}\rangle$ for liquid water in a (14,0) and (19,0) CNT with diameter d. The shift δ is referenced relative to the computed bulk water isotropic shielding of 24.3(3) ppm (Table 1). All shieldings are in units of ppm.

	d	$\langle\sigma_{\rm iso}^{\rm liq}\rangle$	$\langle\Delta\sigma^{\rm liq}\rangle$	δ
(14,0)	11.0 Å	48.5(4)	25.3(5)	−24.2(5)
(19,0)	14.9 Å	47.1(8)	25.3(7)	−22.8(9)

shift due to encapsulation is also is much larger than changes expected from reasonable variations in the liquid structure or computational parameters in the DFT linear response methodology. On the other hand, the confined liquid $\langle\Delta\sigma^{\rm liq}\rangle$ is similar to that of free bulk water. Given the above observations for single molecules, $\langle\Delta\sigma^{\rm liq}\rangle$ is sensitive to both hydrogen bonding in the liquid, and the orientation of individual water molecules relative to the CNT axis. The computed shieldings for water in the (14,0) and (19,0) tubes are very similar, and more statistical sampling would be required in order to clearly resolve any differences.

Figure 1 shows the shieldings of individual protons as a function of radial distance r from the center of the (14,0) and (19,0) CNTs. The corresponding radial hydrogen density distributions from Ref. 5 are also shown. The spread in proton shieldings is generally quite large, which reflects the sensitivity of the proton shieldings to the local hydrogen bond environment. A similar effect was also seen in the bulk water studies of Refs. 19 and 23. Nevertheless, one clear feature is evident: in both the (14,0) and (19,0) CNTs, the distribution of $\sigma_{\rm iso}$ for protons closest to the CNT wall exhibits a significant narrowing and shift to higher values, while the distribution of $\Delta\sigma$ narrows and shifts to lower values.

As previously described in Ref. 5, the CNT-confined water has an interfacial layer that peaks at about 3.5 Å from the CNT wall. The water molecules in this interfacial layer are mostly arranged to form hydrogen bonds parallel to the CNT wall. The small shoulder seen in this first density peak is due to a slight preference for molecules to orient with a non-hydrogen-bonded O-H pointing out towards the CNT wall. By comparison with the radial densities, the qualitative changes in the shieldings at the interface correlate with these non-hydrogen-bonded O-H, which are shifted upfield relative to the other hydrogen-bonded protons. The main difference in the confined liquid

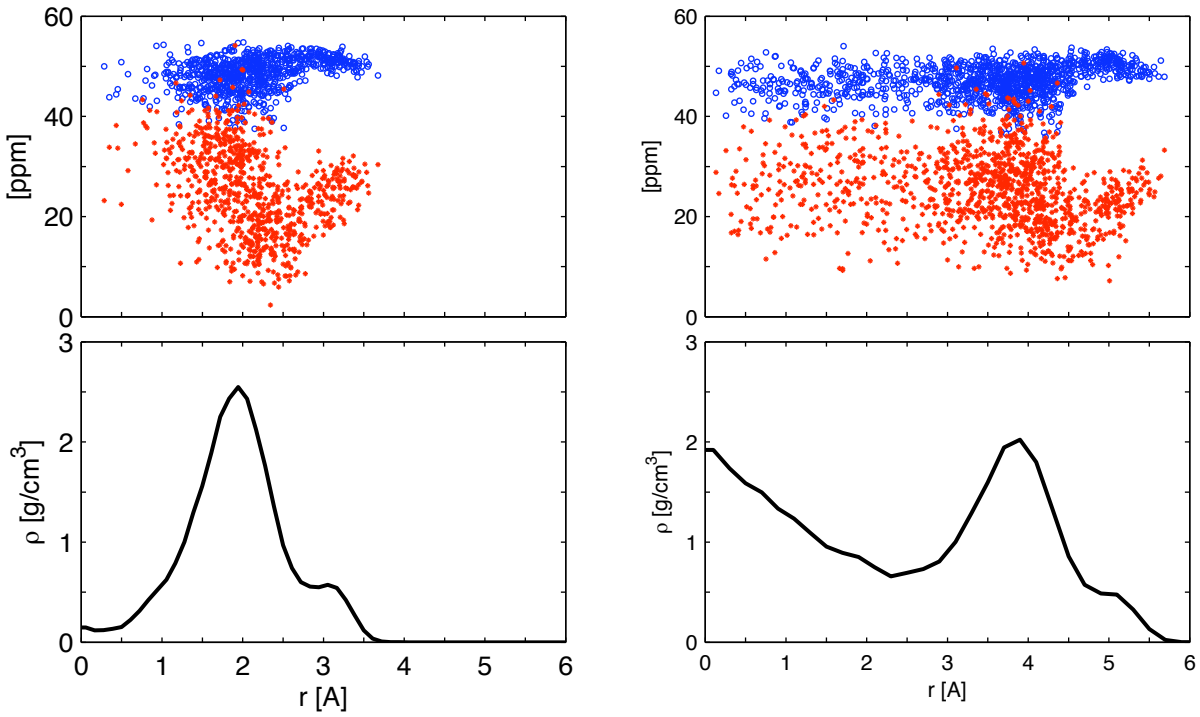

Figure 1: (color on-line) Upper panels: Isotropic shielding $\sigma_{\rm iso}$ (blue) and shielding anisotropy $\Delta\sigma$ (red) for individual water protons in a (14,0) CNT (left) and (19,0) CNT (right), as a function of distance r from the nanotube center. Lower panels: Corresponding proton densities, adapted from Ref. 5. The (14,0) CNT radius is 5.5 Å, and the (19,0) CNT radius is 7.45 Å.

structure for the (14,0) and (19,0) CNTs is that the smaller (14,0) CNT essentially contains just interfacial water with very little liquid in the center of the nanotube, while the (19,0) CNT is large enough to hold both an interfacial layer and a bulk-like fluid in the interior.

In order to determine if this strongly diamagnetic environment is restricted to the interior of the CNT, we have also examined the effect on water molecules outside a nanotube. In an actual sample, nanotubes typically aggregate in bundles, creating interstitial regions that molecules could potentially occupy. This is modeled as a hexagonal array of CNTs with a single water molecule in the hollow sites. The interstital water is oriented with one O-H bond parallel to the CNT, and the second O-H pointing towards the region between two adjacent CNTs. We did not attempt to optimize atom positions, as the aim here is to qualitatively probe the proton shielding in these regions. Brillouin zone sampling is done using a 4×4 k-point mesh along the lateral directions, and the sampling along the c-axis is the same as the isolated nanotube calculations above. A cylindrical susceptibility correction [Eq. (4)] of $\alpha_{xx} = \alpha_{yy} = 1/2$ and $\alpha_{zz} = 1$ is used. We find a *downfield* proton shift of $\delta \sim 1.7$ ppm and $\delta \sim 0.5$ ppm relative to the isolated water molecule, with the smaller shift due to the proton on the parallel O-H bond. While the direction of the shift is opposite to that of water inside the CNT, the magnitude is not nearly as dramatic.

It is unlikely that the large effects of the CNT on the confined water shieldings are due to chemical bonding interactions, as the water is positioned too far from the carbon atoms in the cases discussed above. Instead, these effects can be understood as originating from induced currents on the CNT. This is analogous to the textbook example of ring currents in benzene and other π-conjugated molecules, which generate a strongly anisotropic induced field that causes large chemical shifts in nearby protons. In CNTs, the application of an external magnetic field along the tube axis generates extended currents encircling the circumference of the nanotube, whose topology creates a strongly diamagnetic environment inside the nanotube.[27] Here, we have quantified these effects on the proton isotropic shift, and demonstrated the sensitivity of the shielding tensor components to the orientation of the encapsulated water molecules.

There is a large spread in the experimental values for the isotropic proton shifts of water con-

fined in CNTs, which is likely to be due to different CNT preparation procedures, as well as the precise details of how the measurements are carried out. The early experiments of Ghosh *et al.*[6] report a confined water resonance at 13.8 ppm and free bulk water at 4.6 ppm, implying that confinement in CNTs results in a +9.2 ppm *downfield* shift relative to bulk water. Sekhaneh *et al.*[7] and Chen *et al.*[9] subsequently employed magic angle spinning techniques to improve the spectral resolution; both studies found the confined water resonance to be shifted *upfield* relative to their reported resonances for free bulk water, by -3.3 ppm[7] and -4.4 ppm,[9] respectively. Matsuda *et al.*[8] report a larger ~ -15 ppm upfield shift for the confined water relative to free bulk water.

The theoretical calculations here for the liquid-filled CNTs find large upfield shifts relative to bulk water, that are around -8 ppm to -9 ppm farther upfield than the results of Matsuda *et al.*[8] In general however, one must be careful in making a direct comparison between our ideal, defect-free, single CNT model with experiments, as the process of opening the CNTs will certainly introduce defects that can potentially obscure the experimental data. We have repeated the single encapsulated water molecule studies above, using instead a CNT with a single Stone-Wales defect,[29] but the differences were minor compared to the large proton shifts induced by the defect-free CNT. However, this may or may not be representative of the types of defects formed during sample preparation, and a thorough survey of possible defects is beyond the scope of this work. We note that a recent experimental study using a gentler procedure to remove end caps report a ^{1}H-NMR spectra for ethane gas in CNTs. A broad resonance for confined ethane is observed, whose peak is shifted by > 50 ppm upfield relative to the free ethane resonance.[30]

In summary, we have evaluated the magnetic response and ^{1}H-NMR chemical shieldings of water confined in ideal, infinite CNTs. The calculations are done using a DFT-based linear response theory with plane-wave basis sets and periodic boundary conditions. The confined water resonance is shifted upfield relative to free, bulk water. This is consistent with previous theoretical work on empty CNTs, which find a strongly diamagnetic environment in the interior, as well as with the more recent experiments reported to date. For the liquid-filled CNT, we find the magnitude of the confined water shift to be ~ -23 ppm upfield relative to free bulk water, which is still

large compared to the range of -3.3 ppm to -15 ppm seen in experiments so far. However, the large spread in the experimental values suggest that the actual shift is probably very sensitive to details involved in sample preparation. A more detailed examination of the proton shieldings for the confined liquid reveals a component associated with non-hydrogen-bonded O-H groups at the immediate interface between the liquid and the CNT wall, and a component due to the bulk-like interior.

Acknowledgments We thank Julie Herberg and Jason Holt for helpful discussions regarding the ^{1}H-NMR experiments. This work was partly performed under the auspices of the U.S. Department of Energy by Lawrence Livermore National Laboratory under Contract DE-AC52-07NA27344, and was supported by the Office of Science, U.S. Department of Energy, SciDAC grant DE-FC02-06ER46262. Use of computer resources from Lawrence Livermore National Laboratory and the Innovative and Novel Computational Impact on Theory and Experiment (INCITE) program are gratefully acknowledged.

References

(1) Rasaiah, J. C.; Garde, S.; Hummer, G. *Annu. Rev. Phys. Chem.* **2008**, *59*, 713.

(2) Holt, J. K.; Park, H. G.; Wang, Y.; Stadermann, M.; Artyukhin, A. B.; Grigoropoulos, C. P.; Noy, A.; Bakajin, O. *Science* **2006**, *312*, 1034.

(3) Fornasiero, F.; Park, H. G.; Holt, J. K.; Stadermann, M.; Grigoropoulos, C. P.; Noy, A.; Bakajin, O. *Proc. Natl. Acad. Sci. U.S.A.* **2008**.

(4) Hummer, G.; Rasaiah, J. C.; Noworyta, J. P. *Nature* **2001**, *414*, 188.

(5) Cicero, G.; Grossman, J. C.; Schwegler, E.; Gygi, F.; Galli, G. *J. Am. Chem. Soc.* **2008**, *130*, 1871.

(6) Ghosh, S.; Ramanathan, K. V.; Sood, A. K. *Europhys. Lett.* **2004**, *65*, 678.

(7) Sekhaneh, W.; Kotecha, M.; Dettlaff-Weglikowska, U.; Veeman, W. S. *Chem. Phys. Lett.* **2006**, *428*, 143.

(8) Matsuda, K.; Hibi, T.; Kadowaki, H.; Kataura, H.; Maniwa, Y. *Phys. Rev. B* **2006**, *74*, 073415.

(9) Chen, Q.; Herberg, J. L.; Mogilevsky, G.; Wang, H.-J.; Stadermann, M.; Holt, J. K.; Wu, Y. *Nano Lett.* **2008**, *8*, 1902.

(10) Mauri, F.; Louie, S. G. *Phys. Rev. Lett.* **1996**, *76*, 4246.

(11) Pickard, C. J.; Mauri, F. *Phys. Rev. B* **2001**, *63*, 245101.

(12) P. Giannozzi et al., http://www.quantum-espresso.org.

(13) Mauri, F.; Pfrommer, B. G.; Louie, S. G. *Phys. Rev. Lett.* **1996**, *77*, 5300.

(14) Perdew, J. P.; Burke, K.; Ernzerhof, M. *Phys. Rev. Lett.* **1996**, *77*, 3865.

(15) Grossman, J. C.; Schwegler, E.; Draeger, E. W.; Gygi, F.; Galli, G. *J. Chem. Phys.* **2004**, *120*, 300.

(16) Schwegler, E.; Grossman, J. C.; Gygi, F.; Galli, G. *J. Chem. Phys.* **2004**, *121*, 5400.

(17) Pfrommer, B. G.; Mauri, F.; Louie, S. G. *J. Am. Chem. Soc.* **2000**, *122*, 123.

(18) Sprik, M.; Hutter, J.; Parrinello, M. *J. Chem. Phys.* **1996**, *105*, 1142.

(19) Sebastiani, D.; Parrinello, M. *Chem. Phys. Chem.* **2002**, *3*, 675.

(20) Modig, K.; Halle, B. *J. Am. Chem. Soc.* **2002**, *124*, 12031.

(21) Silvestrelli, P. L.; Bernasconi, M.; Parrinello, M. *Chem. Phys. Lett.* **1997**, *277*, 478.

(22) Ditchfield, R. *J. Chem. Phys.* **1976**, *65*, 3123.

(23) Modig, K.; Pfrommer, B. G.; Halle, B. *Phys. Rev. Lett.* **2003**, *90*, 075502.

(24) Zurek, E.; Pickard, C. J.; Walczak, B.; Autschbach, J. *J. Phys. Chem. A* **2006**, *110*, 11995.

(25) Sebastiani, D. *Chem. Phys. Chem.* **2006**, *7*, 164.

(26) Marques, M. A. L.; d'Avezac, M.; Mauri, F. *Phys. Rev. B* **2006**, *73*, 125433.

(27) Sebastiani, D.; Kudin, K. N. *ACS Nano* **2008**, *2*, 661.

(28) Besley, N. A.; Noble, A. *J. Chem. Phys.* **2008**, *128*, 101102.

(29) Stone, A. J.; Wales, D. J. *Chem. Phys. Lett.* **1986**, *128*, 501.

(30) Wang, H.-J.; Xi, X.-K.; Kleinhammes, A.; Wu, Y. *Science* **2008**, *322*, 80.

LAWRENCE
LIVERMORE
NATIONAL
LABORATORY

UCRL-JRNL-235619

Probing Properties of Water Under Confinement: Infrared Spectra

M. Sharma, D. Donadio, E. Schwegler, G. Galli

October 17, 2007

Physical Review Letters

Probing properties of water under confinement: Infrared spectra.

Manu Sharma,[1], Davide Donadio,[1] Eric Schwegler,[2] and Giulia Galli[1]
[1] *Department of Chemistry, University of California, One Shields Avenue, Davis, CA 95616 and*
[2] *Lawrence Livermore National Laboratory, Livermore, CA 94550*
(Dated: October 9, 2007)

We have computed infrared (IR) spectra of heavy water (D_2O) confined between graphene and deuterium-terminated (D-terminated) diamond(111) surfaces using first principles molecular dynamics simulations. The analysis of these spectra reveal clear signatures of electronic charge fluctuations at the interfaces, occurring even in the case of highly hydrophobic substrates. Our results point at a complex electro–dynamical interaction of liquid water and the surfaces, and highlight the key role played by the surface electronic structure in determining interfacial interactions. The computed spectra also exhibit blue shifts of stretching modes under confinement, and red shifts of the hindered translational modes, that arise mostly from the modified hydrogen bonded network at the interface.

PACS numbers:

Understanding the behavior of water in confined media has profound implications in vastly different areas of science, ranging from nanofluidics [1, 2], enzyme catalysis [3, 4] and biosensors [5, 6] to geological sciences [7]. Unfortunately, the experimental characterization of the fluid under confinement is very challenging and many of the available experimental data are the subject of debate. In particular, the interpretation of vibrational, X-Ray or other spectroscopic measurements [8, 9] revealing new liquid phases of water at the nanoscale remains controversial.

Recently a first–principles computational study of the structural properties of water confined between graphite and carbon nanotubes has been performed [10], where it was found that the perturbation on the water hydrogen bonded network induced by the confining surfaces is spatially localized within a thin (∼0.5 nm) interfacial layer, with enhanced lateral diffusion of the fluid at the interface. However, a fundamental question that remains open is the identification of a set of observables allowing for a straightforward comparison between simulations and existing and future measurements, thus providing a robust probe of the fluid under confinement.

Here we present a series of *ab-initio* calculations of infrared (IR) spectra of water confined between graphene and deuterated diamond surfaces, and we show that IR spectroscopy can reveal key physical features of the fluid at the interface with confining media. In particular, the analysis of IR spectra provides clear signatures of electronic charge fluctuations occurring at interfaces, even in the case of highly hydrophobic substrates, highlighting the important role played by the surface electronic structure in determining interfacial properties. This is a general result, with important implications for the behavior of water at different interfaces, encompassing, e.g. biological environments and inorganic materials. In addition our findings provide a clear interpretation of recent IR spectra measured for water in carbon nanotubes (CNT) [8].

We employed a parameter free, first–principles approach based on density functional theory (DFT) [11, 12]. We computed the IR spectra of heavy water (D_2O) confined between (a) graphene and (b) D-terminated diamond (111) surfaces using a modified Car-Parrinello (CP) [13, 14] scheme, as implemented in the `Quantum ESPRESSO` package [15], in which maximally localized Wannier functions (MLWFs) [16], in place of delocalized Bloch orbitals, are propagated "on-the-fly". MLWFs provide a convenient local picture of polarization by allowing one to assign molecular dipole moments to individual molecules and the confining surface. This enables one to devise dynamical correlation functions and isolate the actual IR contributions arising from specific modes and/or specific atomic species. As in Refs. [17, 18] we defined the dipole moment of a water molecule μ_i as: $\mu_i = 6R_O + R_{D_1} + R_{D_2} - 2\sum_{l=1,4} R_{W_l}$ where R_{D_1} and R_{D_2} are the co–ordinates of the two deuterium atoms, R_O is the position of the oxygen atom and $R_{W_l}, l = 1, 4$ are the centers of the four (doubly occupied) MLWFs associated to molecule i. The total polarization is then given as the sum of the individual dipole moments and the dipole moment of the surface.

The IR absorption coefficient per unit path length of a sample of volume V is given by [19, 20]:

$$\alpha(\omega) \propto \frac{\omega^2\beta}{n(\omega)V}\int_{-\infty}^{\infty} dt\ \mathrm{e}^{-i\omega t}\langle \sum_{ij} \boldsymbol{\mu}_i(t)\cdot\boldsymbol{\mu}_j(0)\ \rangle, \qquad (1)$$

where $n(\omega)$ is the refractive index and $\beta = k_B T^{-1}$ is the inverse temperature.

We first present the IR spectra of water confined by graphene sheets (composed of 60 C atoms), starting from the case with smallest confinement distance, i.e. 32 D_2O with 19.07 a.u. confinement length. We then discuss the effect of confinement on the observed properties as the separation between surfaces is increased. Finally, we discuss water confined by D-terminated diamond(111) surfaces (96 C atoms) and comment on similarities and differences with respect to the graphene case.

In order to identify spectral features possibly arising from "confinement" effects and to distinguish them from those due to "surface effects", (*i.e.*, due to the mere interaction of the water molecules with the surface) we performed several molecular dynamics MD simulations with varying confinement distances. We considered three systems containing 32, 54 and 108 D_2O molecules confined within graphene sheets with separations of 19.07, 27.23 and 47.28 a.u., respectively. The simulations were performed in the microcanonical ensemble at a temperature of ∼350 K [10, 22]. As described in Ref. [10], in order to prepare an initial configuration for our MD simulations, we performed several classical MD runs using the GROMACS [21] package, and chose the one that resulted in an average pressure close to 1 atm. We also verified that water remains diffusive during the time–scale of the simulation [23, 24]. The characterization of the structural properties for these systems have been described elsewhere [10].

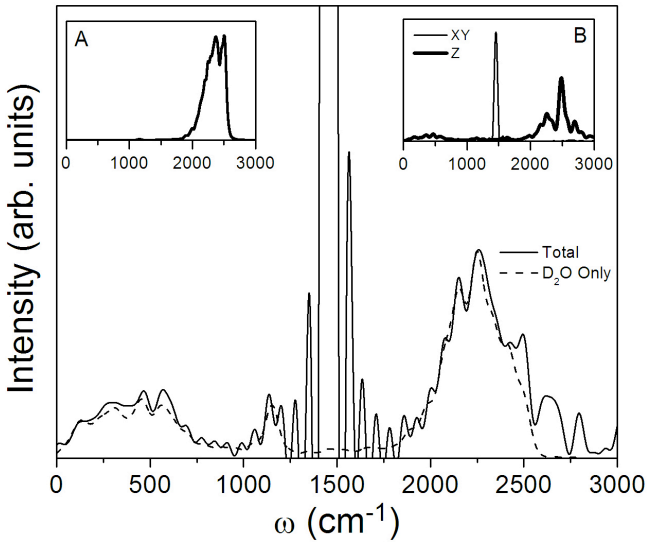

FIG. 1: Computed IR spectrum of 32 D_2O molecules in graphene with a confinement distance of 19.07 a.u. The solid line represents the full spectrum (D_2O plus surface) and the dashed line represents the contribution from the water molecules. The insets show (A) the O–D stretch power spectrum and (B) the in–plane and out–of–plane IR spectra of the graphene surface (see text). The peaks at higher frequency in the full spectrum are likely overtones of the ∼2500 cm^{-1} O-D stretch and the ∼200 cm^{-1} hindered translational mode. See *e.g.,* Ref. [18].

In Fig. 1, we report the computed IR spectrum of 32 water molecules in graphene at a confinement of 19.07 a.u. The solid line represents the full spectrum (surface plus D_2O), while the dashed line shows the contribution from the water molecules. This has been evaluated by restricting the sum in Eq. 1 to the molecules only, when computing the dipole-dipole correlation function. We focus on the high frequency modes, which are related to the O-D bond stretching. While the full spectrum exhibits a peak at ∼2500 cm^{-1}, the water one does not, although such a feature is present in the power spectrum of the O-D stretch (see inset A). This indicates that the IR activity of some of the O-D stretching modes is negligible. Inspection of atomic trajectories identifies these modes as pertaining to vibrations of O-D bonds not engaged in hydrogen bonding (HB), due to the presence of the surface. The lack of IR activity is surprising, as stretching modes of asymmetric-top molecules such as water result in a change of the molecular dipole moment (see *e.g.*, [25, 26]) and thus are expected to be IR active. In the case of interfacial water molecules, the IR activity of O-D bonds not engaged in HB is made negligible by electro-dynamical interactions between the water molecules and the surface, in particular by the overlap of the highly polarizable p-electrons of graphene with the water molecules. Therefore the IR activity of interfacial molecules is much decreased with respect to that expected from molecules with 'free' O-D bonds, i.e. bonds not engaged in the hydrogen bonded network. The intricate interactions of the electrons of graphene with the water molecules are also apparent when comparing the IR and power spectra of the surface (not shown). The latter shows no high frequency modes (above ∼ 1600 cm^{-1}), while the IR spectrum does, as shown by the inset (B) of Fig. 1, where we plot the in-plane and out-of-plane IR spectra of the confining graphene sheet. The in-plane spectrum contains only a single mode (corresponding to the C-C stretch of the graphene layer); the out-of-plane spectrum contains instead a prominent peak at ∼2500 cm^{-1}, and it correlates well with *all* the features observed in the water spectrum. These high frequency peaks of the graphene spectrum are not related to ionic vibrations but to charge fluctuations induced by the interaction with water. This complex interaction also manifests itself in the dipole density profile (Fig. 4 inset D), which displays a peculiar peak at the interface, indicating a preferential orientation of the water dipoles at the interface. This electro-dynamical interaction depends critically on the chemical nature of the confining surface, as it will be shown below.

Fig. 2 reports the D_2O contribution to the IR spectra of the three D_2O systems confined in graphene. Also shown in the inset is the IR spectrum of bulk water (thick line) along with that of 108 D_2O (thin line) with a confinement distance of 47.28 a.u. The high frequency region of the spectrum shows a systematic blue shift as the confinement distance is decreased, since the fraction of molecules close to the surface (i.e. the fraction of molecules with broken H-bonds) increases, thus resulting in an increased O-D stretching frequency (the computed frequency of the free O-D stretch in the isolated monomer is 2706 cm^{-1}). Furthermore, the far IR region of the spectrum shows a systematic red shift with increasing confinement. These low frequency modes arise from

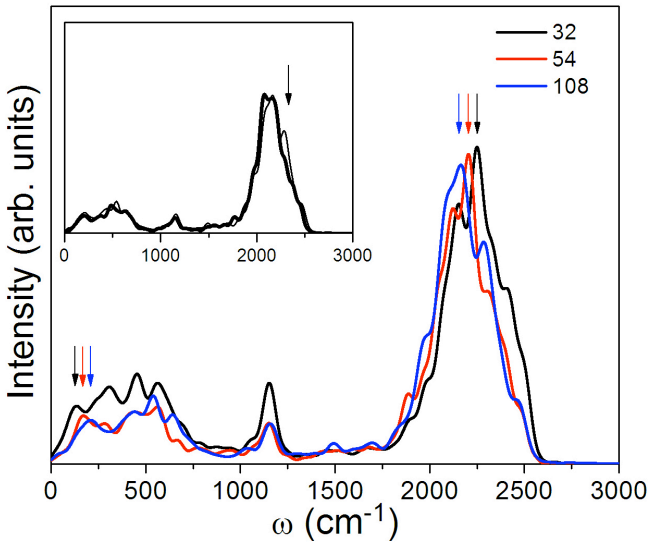

FIG. 2: The IR spectra of water at different confinements of 19.07 (black line), 27.23 (red line) and 47.28 (green line) a.u. respectively. The numbers in the legend correspond to the number of water molecules in the simulation. The arrows indicate blue (red) shift in the near(far) IR region of the spectrum with increasing confinement. The inset shows a comparison of the bulk water IR spectrum (thick line) with the simulation with the largest confinement distance (108 D_2O) (thin line). The arrow in the inset indicates the presence of high frequency O–D stretching modes in the 108 D_2O system, indicating more broken H–bonds with respect to the bulk.

hindered translational modes in water[18] and reflect the complex dynamics of the liquid H-bonds. The observed red-shift is again consistent with an increase in the fraction of interfacial molecules, as the confinement distance is increased. It is noteworthy that the spectrum of 108 D_2O is virtually indistinguishable from that of the bulk, (see inset) but for a weak feature in the near IR (indicated by an arrow); this feature reflects the presence of a larger number of broken H-bonds than in the bulk liquid, due to the presence of the surface.

We note that the features observed here in the IR spectrum of water confined between graphene surfaces have been reported also in experimental spectra detected for the fluid within CNT, where they have been interpreted as arising from a new phase present only under confinement [8]. We have shown here that such features arise instead due to subtle but important electronic effects occurring at the interface.

We now turn to the discussion of water confined by a surface that is qualitatively different from graphene, in that it has no diffuse p–orbitals. We considered a deuterium-terminated diamond (111) surface with 54 D_2O molecules and a confinement distance of 37.24 a.u. In this simulation, the temperature of the system was ∼390 K. Since in this case the surface layer has a closed shell electronic configuration, we expect negligible charge fluctuations in this system, associated to the "free" O-D stretching mode. Indeed, as Fig. 3 shows, the ∼2500 cm^{-1} peak is present both in the full IR spectrum (full line) and in that of the confined water molecules (dashed line). The insets show (A) the IR spectrum of the surface and (B) the O-D stretch power spectrum of the confined molecules, respectively.

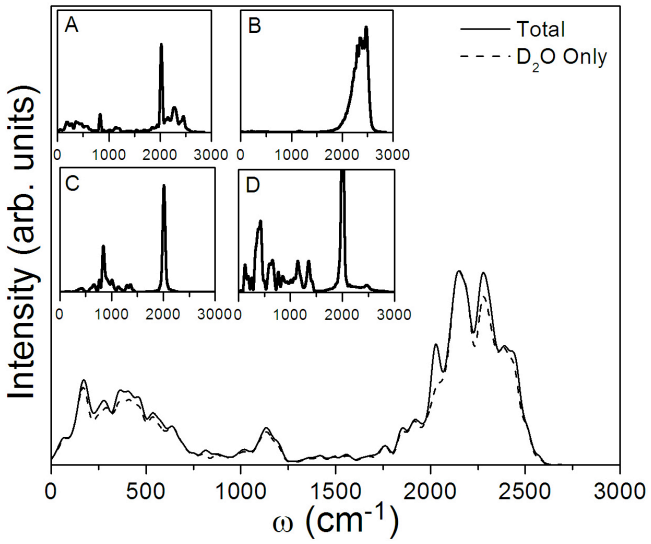

FIG. 3: Computed IR spectrum of 54 D_2O molecules confined by D-terminated diamond(111) surface. The solid line shows the full spectrum (surface plus water) and the dashed line represents the contributions from the water molecules. The insets show (A) the IR spectrum of the surface, (B) the O-D stretch power spectrum, (C) the "kinematic" C-D stretch power spectrum and (D) the "dynamical" C-D stretch power spectrum (see text).

However, in spite of having a closed shell structure, the IR spectrum of the surface has a small albeit finite intensity at ∼2500 cm^{-1}. The reason is that the electronic charge density of the surface layer does not follow rigidly the nuclear framework; even in a closed shell configuration characteristic of hydrophobic systems, the surface electronic structure is extremely sensitive to the environment. This is evident from the comparison of the spectra shown in insets (D) and (C) of Fig. 3. The former shows the "dynamical" power spectrum of the C-D stretching mode. Here we define the dipole moment associated to the C-D bond in terms of the nuclear co–ordinates of the C and D atoms and the Wannier function associated to the bond as $\mu_{CD} = R_C + R_D - 2R_{W_{CD}}$. Inset (C) shows the" kinematic" power spectrum of the C-D stretch which we compute by simply taking the Fourier transform of the C-D bond length autocorrelation function. While the kinematic spectrum shows no modes at ∼2500 cm^{-1}, the dynamical spectrum (inset (D)) does. This reflects the sensitivity of the surface electronic charge density to its environment.

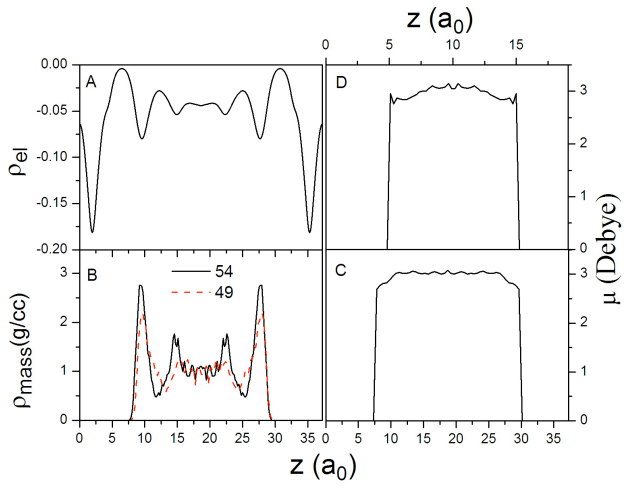

FIG. 4: (A). The electronic density profile for the 54 D_2O molecules in D-terminated diamond(111) surface showing a depletion of charge at the interface. The position of the surface D atoms is indicated by vertical lines. (B). the mass density profile for water confined in D-terminated diamond(111) surface at two different values of the density different by 10%. The sharp increase in the density at the interface is only weakly dependent on the density. (C). The dipole distribution of the water molecules normal to the surface for 54 D_2O in D-terminated diamond(111) surface. (D). The dipole distribution of the water molecules normal to the surface for 32 D_2O in graphene surface.

Further characterization of water confined in D-terminated diamond is shown in Fig. 4 which reports (A) the electronic charge density distribution, (B) the mass density distribution for two simulations performed at two densities different by 10%, (C) the dipole moment distribution for the 54 D_2O molecules confined in D-terminated diamond (111) surface and (D) the dipole moment distribution for the 32 D_2O molecules confined in the graphene surface, for comparison. The two dipole distributions (C) and (D) are qualitatively different, reflecting the different nature of the two surfaces. In the case of graphene, the average dipole moment per molecule shows a sharp increase when the molecule is very close to the surface. As mentioned before, this is due to the interaction between the "free" O–D bond of water and the p–electrons of the graphine. On average, the water molecules at the interface arrange in such a way that the D atoms lie above the underlying C atoms of the surface, while the O atoms occupy positions above the center of the underlying hexagons [10]. In the case of deuterated diamond, the situation is qualitatively different. The molecules exhibit no particular spatial preference, and the dipole of the molecules near the surface is not enhanced, but decreases to a value lower than that in the bulk, and lower than that found in the case of graphene confinement.

In summary, we have presented a study of the vibrational properties of water confined between graphene and hydrophobic, deuterated diamond surfaces, carried out using *ab-initio* calculations. A detailed analysis of the IR spectra showed the complex electronic nature of the interactions between the surface and the water molecules, present even in the case of closed shells, hydrophobic substrates. These findings also provide an alternative explanation of IR spectra recently detected for water in CNTs, that were interpreted as showing new phases of the liquid under confinement. We have proposed here that the detected effects arise instead from electro-dynamical coupling occurring at the interface. Finally, our results show that IR spectroscopy, in conjunction with *ab-initio* calculations, can be a very powerful tool to probe water under confinement, in several different environments.

Part of this work was performed under the auspices of the U.S. Department of Energy by Lawrence Livermore National Laboratory under Contract DE-AC52-07NA27344.

[1] J. K. Holt *et. al.*, Science **312**, 1034 (2006).
[2] M. Majumder, N. Chopra, R. Andrews and B. J. Hinds, Nature **438**, 44 (2005).
[3] J. Israelachvilli and H. Wennerstrom, Nature **379**, 219 (1996).
[4] R. G. Bryant, Ann. Rev. Biophys. Biomol. Str. **25**, 29 (1996).
[5] F. Balavoine *et. al.*, Angew. Chem. Int. ed., **38**, 1912 (1999).
[6] C. V. Nguyen *et. al.*, Nano Lett., **2**, 1079 (2002).
[7] S. Karaborni, B. Smit, W. Heidug, J. Urai and E. vanOort, Science **271**, 1102 (1996).
[8] O. Byl, J.-C. Liu, Y. Wang, W.-L Yim, J. K. Johnson and J. T. Yates, J. Am. Chem. Soc. **128**, 12090 (2006).
[9] A. Poynor, L. Hong, I. K. Robinson, S. Granick, Z. Zhang and P. A. Fenter, Phys. Rev. Lett. **97**, 266101 (2006).
[10] G. Cicero, J. C. Grossman, E. Schwegler, F. Gygi and G. Galli, *submitted* (2007).
[11] P. Hohenberg and W. Kohn, Phys. Rev. B **136**, 864 (1064) .
[12] W. Kohn and L. J. Sham, Phys. Rev. **140**, A1133 (1965).
[13] R. Car and M. Parrinello, Phys. Rev. Lett. **55**, 2471 (1985).
[14] M. Sharma, Y. Wu, and R. Car, Int. J. Quantum Chem. **95**, 821 (2003).
[15] http://www.quantumespresso.org.
[16] N. Marzari and D. Vanderbilt, Phys. Rev. B **56**, 12847 (1997).
[17] P. L. Silvestrelli and M. Parrinello, Phys. Rev. Lett. **82**, 3308 (1999).
[18] M. Sharma, R. Resta, R. Car, Phys. Rev. Lett. **95**, 187401 (2005).
[19] J. S. Bader and B. J. Berne, J. Chem. Phys. **100**, 8359 (1994).
[20] R. Ramírez, T. L. López-Ciudad, P. Kumar P and D. Marx, J. Chem. Phys. **121**, 3973 (2004).
[21] E. Lindahl, B. Hess and D. van der Spoel, J. Mol. Mod. **7**, 306 (2001).

[22] We adopt norm-conserving pseudopotentials [27], a plane-wave cutoff of 85 Ry, and the DFT Purdue Burke Ernzerhof functional for exchange and correlation [28]. Long range electrostatic effects are treated with the Ewald summation technique. We use an integration time step of 7 a.u. (0.17 fs) and a fictitious electron mass of 350 a.u. in the CP equations [13]. All simulations were equilibrated for 2 ps followed by 10 ps of data collection.

[23] J. C. Grossman, E. Schwegler, E. W. Draeger, F. Gygi and G. Galli, J. Chem. Phys. **120**, 300 (2004).

[24] E. Schwegler, J. C. Grossman, F. Gygi and G. Galli, J. Chem. Phys. **121**, 5400 (2004).

[25] C. N. Banwell and E. M. McCash, *Fundamentals of Molecular Spectroscopy, 4th ed.*, (McGraw Hill College (1994)).

[26] P. F. Bernath, *Spectra of Atoms and Molecules*, (Oxford University Press (1995)).

[27] D. R. Hamann, M. Schlüter and C. Chiang, Phys. Rev. Lett. **43**, 1494 (1979).

[28] J. P. Perdew, K. Burke and M. Ernzerhof, Phys. Rev. Lett. **77**, 3865 (1996).

LAWRENCE
LIVERMORE
NATIONAL
LABORATORY

UCRL-JRNL-232936

First-Principles Simulations of Aqueous Solutions

Eric Schwegler

July 22, 2007

Journal of Physics: Conference Series

First-Principles Simulations of Aqueous Solutions

Eric Schwegler

Lawrence Livermore National Laboratory, Livermore, CA 94550

E-mail: schwegler@llnl.gov

Abstract. The importance of water in many areas of science has motivated an enormous number of experimental and theoretical investigations. In this paper, we review several recent examples where first-principles molecular dynamics simulations coupled with large scale computing has enabled important insight into the unique properties of water in a variety of systems, including pure liquid water, the solvation of ions and hydrophobic solutes and nanoscale confined systems such as water inside carbon nanotubes.

1. Introduction

Advances in both experimental techniques and theoretical methods have resulted in the discovery of a wide range of fascinating new properties of materials. However, in many instances, experimental measurements and simple models are insufficient for a complete understanding of the emerging new phenomena at a microscopic level. In such cases, the combination of first-principles molecular dynamics (FPMD) with large-scale computations have proven to be extremely useful for resolving experimental ambiguities and for predicting the properties of materials where measurements do not yet exist.

One particular area where FPMD simulations have proven to be particularly useful is in examining the properties of liquid water and its interaction with a various solutes. These simulations, which treat electronic degrees of freedom quantum mechanically within density functional theory (DFT) and ionic motion classically, have allowed for important insights into the properties of aqueous solutions under a variety of thermodynamic conditions. Quantum simulation techniques combined with significant increases in available computer power have pushed the computational simulation of water to an exciting stage. Simulations can now be used both to make genuine predictions directly comparable with experiment as well as to establish the accuracy of newly developed classical potentials, which are critical for accessing much longer time scales and much larger systems.

In the following, we briefly review our recent use of FPMD to examine the properties of water in a number of different systems, including simulations of pure liquid water, the solvation of hydrophilic and hydrophobic solutes in water, and water confined to a nanoscale environment.

2. First-Principles Molecular Dynamics

Molecular dynamics has been used for decades to investigate dynamical properties of molecules, solids, and liquids by numerical simulations. In the standard approach, which is usually referred to as classical molecular dynamics, one must provide in advance a model potential for determining the interatomic interactions. In contrast, FPMD-based approaches do not require any empirical or fitted interatomic potentials as input because the interactions between atoms are computed directly from the

electronic structure of the system "on-the-fly" at every time step in the simulation. In particular, the underlying methods that are used are based on finding numerical solutions to the fundamental laws of quantum mechanics in an approximate, yet non-empirical manner. These methods have a distinct advantage over semiempirical or classical simulation approaches in that they can provide a quantitatively accurate description of chemically active species in realistic environment.

The typical FPMD simulation approach is based on the use of a planewave/pseudopotential implementation of density functional theory to describe the electronic structure, and with the MD carried out with either a Car-Parrinello (CP) approach [1], where the electronic and ionic degrees of freedom are coupled by a Lagrangian, or the Born-Oppenheimer (BO) approach, where the electronic wave functions are fully relaxed to the ground state at each time step. In either case, the main computational step is centered on solving the Kohn-Sham equations [2], which involves heavy use of numerical linear algebra methods and three-dimensional Fourier transforms. We refer the interested reader to Ref. [3] for a recent discussion of the challenges involved in massively parallel implementations of FPMD within the context of the Qbox code [4].

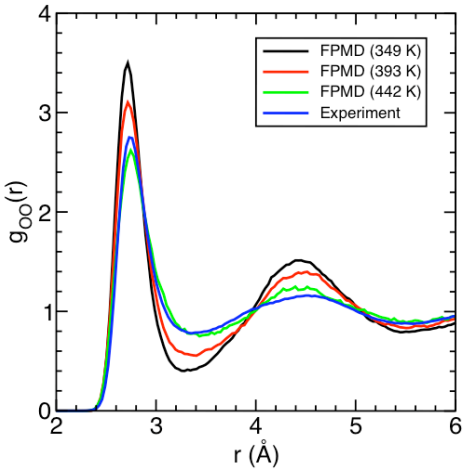

Fig. 1. Oxygen-oxygen radial distribution functions obtained from FPMD simulations of water as a function of temperature in comparison to experimental measurements under ambient conditions [12].

Although first-principles techniques offer distinct advantages over empirical models in terms of accuracy and predictive power, the methods are quite computationally expensive and often require significant computational resources just to simulate a moderate sized system for short periods of time. In the standard implementation, the cost of simulations involving N atoms grows as N^3, which quickly limits the size of systems that can be treated with a reasonable computational cost. For instance, we recently performed a series of first-principles molecular dynamics simulations of a water-filled carbon nanotube involving over 1,600 valence electrons. For this rather large system, a 20 ps long trajectory (1 ps = 10^{-12} s) required approximately 1.2M CPU hours on the Thunder computing platform [5].

3. First-Principles Simulations of Liquid Water

In order to better understand the level of accuracy that can be achieved with DFT-based techniques for the calculation of the properties of liquid water it is helpful to examine the importance of the various approximations that are needed to carry out the simulations. To this end, we have performed a series of long-time scale simulations of water where a number of approximations were tested by varying the density functional employed, the fictitious electron mass used in the CP approach, the system size and the use of CP versus BO approaches.

Our simulations showed that there are negligible differences in the structural properties of the room temperature liquid obtained using different density functionals such as PBE [6] and BLYP [7]; size effects, although not fully negligible when using 32-molecule cells, were found to be rather small. We also found that as long an appropriate fictitious mass parameter is used in the CP approach, results consistent with BO simulations can be readily achieved.

Overall, we have found that in well-converged DFT simulations of water under ambient conditions, the liquid exhibits significant over-structure and slow diffusion as compared to experimental measurements. Very similar results have been reported by a number of different research groups [8]. A significant fraction of this observed over-structure and slow diffusion is due to the neglect of proton quantum motion in the simulations, which can be effectively accounted for by performing simulations

at elevated temperatures. We note that approximately accounting for quantum effects via temperature rescaling is a technique that has been used in a variety of materials other than water [9]. This effect is illustrated in Figure 1, which shows the oxygen-oxygen radial distribution function obtained from FPMD simulations of liquid water at different temperatures in comparison with experimental measurements at ambient conditions. Work is currently underway to directly account the quantum proton motion in our simulations with Feynman path integral sampling techniques [10]. Additional details of these findings can be found in Refs. [11,12].

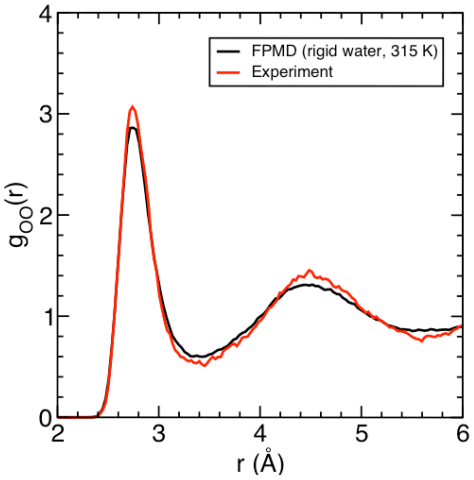

Fig. 2. The oxygen-oxygen radial distribution function from a FPMD simulation of rigid water in comparison with experiment [13].

4. The Rigid Water Approximation

Even with the development of sophisticated codes implemented on massively parallel computers, accurate and well-converged FPMD simulations of water have remained particularly challenging. One of the specific problems encountered in simulations of water is due to the presence of the high-frequency intramolecular modes, *i.e.* the O-H stretch (3200 to 3600 cm^{-1}) and H-O-H bending modes (~1600 cm^{-1}) of water. This is particularly relevant in CP simulations, where one must use a relatively small fictitious mass parameter in order to avoid a direct overlap of ionic and electronic degrees of freedom, which would otherwise lead to severe inaccuracies in the simulation. The use of small values of the fictitious mass necessitates the use of small MD time steps to ensure an accurate integration of the equations of motion. As a consequence, a typical FPMD time step with the CP approach can be less than 0.1 fs, which is at least ten times smaller than what is often used in classical MD simulations of water with empirical interatomic potentials. This poses a severe restriction on the time scales that can be accessed in CP simulations of water.

We note that when using BO dynamics (where the total energy of the system is minimized at each ionic step), it is possible to safely use larger time steps than in CP simulations, because electronic degrees of freedom are not propagated at the same time as ionic coordinates. However, the accuracy required to reduce systematic errors on the ionic forces so as to have conservative dynamics is such that large number of iterations are usually necessary to minimize the Kohn-Sham energy at each ionic step. Therefore, the gain in efficiency obtained with a larger time step is more than counter-balanced by the increased computational time requirement for total energy minimizations.

With the aim of investigating how to increase the integration time step in CP simulations of water and thus access longer time scales, we have carried out calculations using a rigid water approximation. By completely removing the high frequency vibrations and bending modes, the rigid water model allows for much larger values of the fictitious mass, as well as time steps in the CP method. As shown in Figure 2, the use of the rigid water approximation leads to a decrease in the liquid structure as compared to the FPMD simulations of flexible water, which brings the rigid water results into better agreement with experiment. Our results indicate that at least some of the improved agreement is related to the fact that the rigid water model can be considered to be a better representation when the quantum motion of the protons is taken into account. Additional details of these simulations can be found in Ref. [13].

5. Hydrophilic Solvation of Ions

The aqueous solvation of ions is encountered in a wide range of biological and chemical systems. In particular, the manner in which water solvates alkali cations is relevant to problems such as the

mechanism of enzymatic catalysis and the structural stability of DNA and RNA. In order to investigate the hydration structure of ions, a variety of experimental techniques can be used. For example, X-ray and neutron diffraction methods have proved to be valuable tools for determining the static structure factors of waters solvating a given ion. However, experimental measurements often yield an incomplete description of ionic solvation, due to, e.g., the lack of suitable isotope substitutions in neutron diffraction experiments, or difficulties in separating the atomic correlations of different species in diffraction data. In many cases, molecular dynamics simulations have emerged as a successful complement to experimental measurements and have led to a greater understanding of the solvation process.

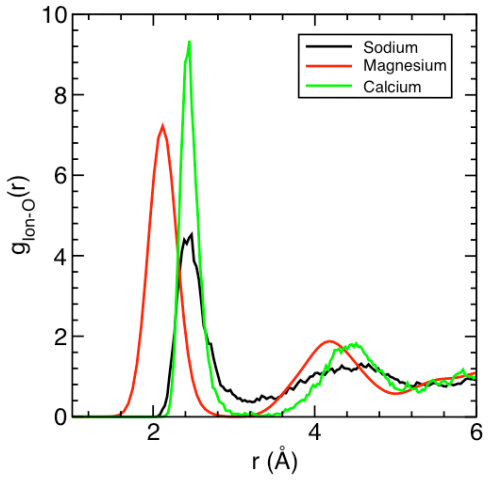

Fig. 3. The ion-oxygen radial distribution functions from FPMD simulations of Na^+ (black), Mg^{2+} (red) and Ca^{2+} (green) solvated in water [14,15,16].

We have carried out first principles molecular dynamics simulations on aqueous solutions of sodium [14], magnesium [15] and calcium [16] cations. The different cation-water radial distribution functions obtained in these simulations are shown in Figure 3. These simulations provide a rather detailed view of the ion solvation process, and can be used to directly interrogate how the properties of the water molecules are altered due to the presence of the ions. On of the more obvious differences between the different cations is that in the case of sodium, the first minimum in $g_{Na-O}(r)$ at approximately 3.5 Å is large. This suggests that the first solvation shell around sodium is rather floppy and that the water molecules move rapidly between the first and second solvation shells. In fact, during the rather short timescale of the simulations, numerous exchange events can be observed.

In the case of magnesium and calcium, the height of the first minimum is much smaller, which indicates that the first solvation shell around these ions is more structured than what is found around sodium. In general, the first solvation shells around magnesium and calcium consist of six water molecules in an octahedral arrangement. Because the ions are divalent cations, these six water molecules tend to be strongly oriented with their oxygen atoms closest to the ion and with their hydrogen atoms pointing away. In order to determine if the presence of the ion has a significant effect on the electronic structure of the first solvation shell waters, we examined the properties of the first solvation shell water molecules with the use of maximally localized Wannier functions [17]. Interestingly, what we found is that the first solvation shell waters tend to asymetrically coordinate with the ion with just one of the lone pair orbitals located on the oxygen atoms, which leads to significant changes in the polarization of the first solvation shell water molecules. This asymmetric orientation gives the water molecules a small "tilt" and only small modifications to hydrogen bonding in agreement with experimental measurements [18,19,20].

6. Hydrophobic Solvation of Small Solutes

The hydrophobic effect plays a central role in processes spanning numerous scientific and technological disciplines, from protein folding to the formation of natural gas hydrates in oil and gas pipelines. We have used a combination of classical and FPMD simulations to probe the impact of small hydrophobic solutes on the local structure of water [21]. In particular, we have recently carried out long time scale FPMD and classical simulations of a benzene molecule in water [22,23]. The solvation of benzene represents an interesting test case for molecular simulations because it involves two quite different interfaces when it is surrounded by water. The equatorial region around the

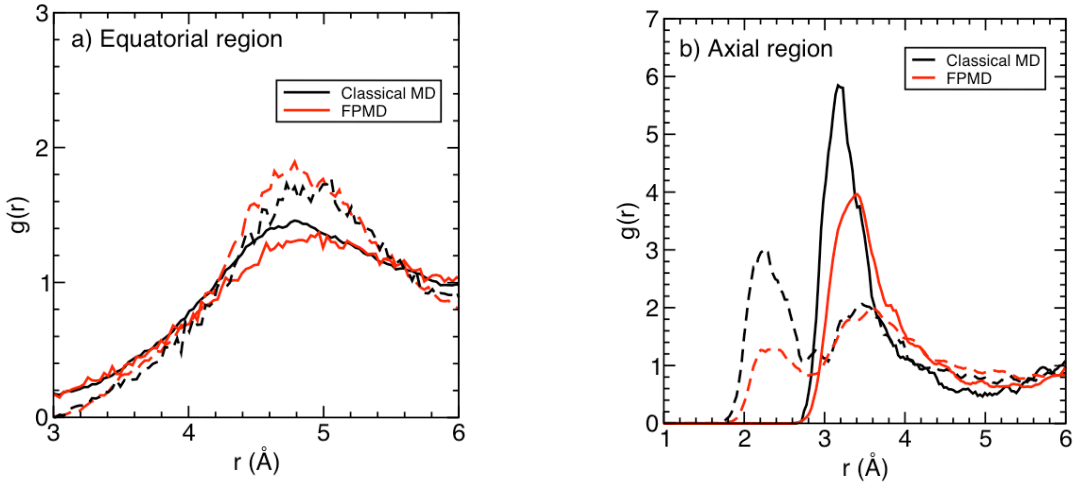

Fig. 4. The benzene-oxygen (solid lines) and benzene-hydrogen (dashed lines) radial distribution functions collected in a) the equatorial region, and b) the axial region around benzene from FPMD (red lines) and classical MD (black lines) simulations.

benzene ring resembles a typical hydrophobic solute, whereas the axial regions near the center of the benzene ring can interact with neighboring water molecules by forming weak π-hydrogen bonds.

In Figure 4, the benzene-oxygen and benzene-hydrogen radial distribution functions around the equatorial and axial regions of benzene obtained from an FPMD and a classical MD simulation are shown. Both simulation approaches find nearly featureless oxygen and hydrogen distributions near the equatorial regions that are peaked at approximately 4.9 Å from the center of the solute. In contrast, the distributions around the axial regions exhibit a noticeable amount of structure. In particular, there is a benzene-hydrogen peak located at approximately 2.3 Å that comes from a slight tendency to form π-hydrogen bonds with nearby water molecules. Although this peak is present in both simulations, the height of the peak is significantly smaller in the FPMD simulation as compared to the classical MD distribution.

The fact that there are similarities between the classical models and the FPMD simulations for the equatorial regions, and significant differences near the axial regions is perhaps not too surprising. In the case of small hydrophobic solutes it is known that the hydrogen bond network mostly persists around the solute - although in a rearranged form [24]. Because the local hydrogen bonds are not broken, the water molecules near the solute see an environment that looks similar to the bulk and as such the classical models tend to work well because these models were originally designed to reproduce the bulk properties of water. However, in cases such as the axial regions around benzene where solute-water interactions become significant, the local environment changes when the water-water hydrogen bonding is no longer preserved. Simple classical models cannot account for these subtle changes in the local environment. We note that a similar breakdown of classical water models should be expected to occur around large hydrophobic solutes and surfaces because it is not possible to preserve the water-water hydrogen bonding around an extended interface [24]. In the case of solvated benzene, the interfacial water molecules in the axial region are weakly bound to the π-electron system of benzene instead of forming water-water hydrogen bonds, which leads to smaller water molecule dipole moments by about 0.15 Debye when compared to the bulk. A similar decrease in the dipole moment of the interfacial waters near the equatorial region of the solute does not occur because water-water hydrogen bonding persists in this region.

7. Water Confined to the Nanoscale

While the properties of bulk liquid water and simple aqueous solutions have been extensively investigated, much less is known about water confined at the nanometer scale, where conventional

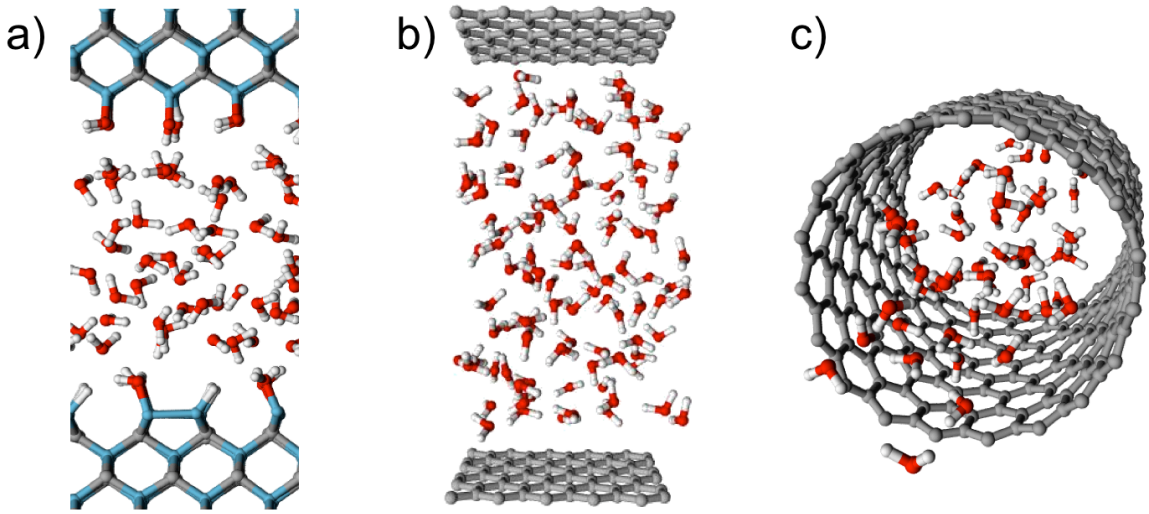

Fig. 5. FPMD simulations of water confined by a) hydroxylated silicon carbide surfaces [26], b) graphitic sheets, and c) a (19,0) carbon nanotube [27].

experimental probes (*e.g.* neutron diffraction and X-ray scattering) are difficult to use and accurate simulations become extremely challenging. Equilibrium properties, phase transformations and molecular mobility of water have all been observed to change upon confinement, however a thorough characterization of these changes is still missing.

A number of theoretical studies using both molecular dynamics and Monte Carlo techniques have been carried out to address some of the issues involved in confined water [25]. However, it should be noted that the existing simulations have all been based on empirically derived classical potentials. As previously mentioned, because these potentials are usually designed to reproduce the properties of bulk water, it is unclear whether they can accurately describe confined states of water that presumably involve complex interfacial regions. Furthermore, as we found near the axial region around benzene, subtle electronic effects can play an important role in understanding the behavior of both water-water and water-solute interactions, which are effects that cannot be captured with simple classical potentials.

We are currently using FPMD simulations to examine how the properties of water change when confined to the nanoscale. As illustrated in Figure 5, our simulations have been designed to address specific issues such as confinement length scale, dimensionality of the confining media, interface effects such as hydrophobic versus hydrophilic surfaces, and the influence of confinement on ion solvation processes.

In the cases of one and two-dimensional confinement by hydrophobic surfaces, our simulations indicate that there is a noticeable spatial ordering of the interfacial water molecules and an overall enhancement of density oscillations that persist for approximately 5 Å away from the surface. For the water molecules closest to the surface, we find a moderate increase in hydrogen bond donors and a specific orientational ordering that leads to an enhancement of four-fold hydrogen bonded ring structures relative to the bulk liquid water. Overall, our results indicate that the majority of changes that occur when water is confined are limited to small regions near the interface and that the liquid quickly recovers its bulk-like properties at moderate distances away from the surface. More specific details from these simulations can be found in Refs. [26,27].

8. Conclusions

We have reviewed several recent examples of the use of FPMD to examine the properties of water in a variety of different systems, including pure liquid water, the solvation of ions and hydrophobic solutes and nanoscale confined systems such as water inside carbon nanotubes. In each case, we highlighted the advantages of using an FPMD approach over less computationally expensive classical methods, especially when dealing with complicated interfacial systems where a high degree of transferability and predictive power is required.

9. Acknowledgments

Parts of this work are the result of collaborations with M. Allesch, E. W. Draeger, G. Galli, G. Cicero, J. C. Grossman, and F. Gygi. This work was performed under the auspices of the U.S. Department of Energy at the University of California/Lawrence Livermore National Laboratory under contract no. W-7405-Eng-48.

References

[1] R. Car and M. Parrinello, Phys. Rev. Lett. **55**, 2471 (1985).
[2] W. Kohn and L. J. Sham, Phys. Rev. A **140**, 1133 (1965).
[3] F. Gygi, J. Phys.: Conf. Ser. **46**, 268 (2006)
[4] Qbox, a scalable implementation of first-principles molecular dynamics (http://eslab.ucdavis.edu).
[5] Thunder is a 23 TFlop computer installed at LLNL in 2004 that consists of 1024 nodes of 4096 Itanium2 processors.
[6] J. P. Perdew, K. Burke and M. Ernzerhof, Phys. Rev. Lett. **77**, 3865 (1996).
[7] A. D. Becke, Phys. Rev. A **38**, 3098 (1988);
C. Lee, W. Yang and R. G. Parr, Phys. Rev. B **37**, 785 (1988).
[8] D. Asthagiri, L.R. Pratt and J.D. Kress, Phys. Rev. E **68**, 041505 (2003);
M.V. Fernandez-Serra and E. Artacho, J. Chem. Phys. **121**, 11136 (2004);
J. VandeVondele, F. Mohamed, M. Krack, J. Hutter, M. Sprik and M. Parrinello, J. Chem. Phys. **122**, 014515 (2005);
P. H. L. Sit and N. Marzari, J. Chem. Phys. **122**, 204510 (2005).
[9] C. Z. Wang, C. T. Chan and K. M. Ho, Phys. Rev. B **42**, 11276 (1990)
L. J. Porter, J. Li and S. Yip, J. Nucl. Mater. **246**, 53 (1997).
[10] R. P. Feynman and A. R. Hibbs, *Quantum Mechanics and Path Integrals* (McGraw Hill, New York, 1965).
[11] J. C. Grossman, E. Schwegler, E. W. Draeger, F. Gygi and G. Galli, J. Chem. Phys. **120**, 300 (2004).
[12] E. Schwegler, J. C. Grossman, F. Gygi and G. Galli, J. Chem. Phys. **121**, 5400 (2004).
[13] M. Allesch, E. Schwegler, F. Gygi and G. Galli, J. Chem. Phys. **120**, 5192 (2004).
[14] J.A. White, E. Schwegler. G. Galli and F. Gygi, J. Chem. Phys. **113**, 4668 (2000).
[15] F. C. Lightstone, E. Schwegler, R.Q. Hood, F. Gygi and G. Galli, Chem. Phys. Lett. **343** 549 (2001).
[16] F. C. Lightstone, E. Schwegler, M. Allesch, F. Gygi and G. Galli, ChemPhysChem **6**, 1745 (2005).
[17] F. Gygi, J. L. Fattebert and E. Schwegler, Comp. Phys. Comm. **155**, 1 (2003).
[18] J. L. Fulton, S. M. Heald, Y. S. Badyal and J.M. Simonson, J. Phys. Chem. A **107**, 4688 (2003).
[19] A. W. Omta, M. F. Kropman, S. Woutersen, H.J. Bakker, Science **301**, 347 (2003).
[20] L. A. Naslund, D. C. Edwards, P. Wernet, U. Bergmann, H. Ogasawara, L.G.M. Pettersson, S. Myneni and A. Nilsson, J. Phys. Chem. A **109**, 5995 (2005).
[21] J. C. Grossman, E. Schwegler and G. Galli, J. Phys. Chem. B **108**, 15865 (2004).
[22] M. Allesch, E. Schwegler and G. Galli, J. Phys. Chem. B **111**, 1081 (2007).
[23] M. Allesch, F. C. Lightstone, E. Schwegler and G. Galli, submitted (2007).

[24] D. Chandler, Nature **437**, 640 (2005).
[25] See for example: G. Hummer, J. C. Rasaiah, J. P. Noworyta, Science **414**, 188 (2001);
K. Koga, G-T. Gao, H. Tanaka and X. C. Zeng, Science **412**, 802 (2001);
l A. Striolo, Nano Lett. **6**, 633 (2006);
K. Shirono and H. Daiguji, J. Phys. Chem. C **111**, 7938 (2007);
P. Hirunsit, P. B. Balbuena, J. Phys. Chem. C **111**, 1709 (2007).
[26] G. Cicero, J. C. Grossman, A. Catellani and G. Galli, J. Amer. Chem. Soc. **127**, 6830 (2005).
[27] G. Cicero, J. C. Grossman, E. Schwegler, F. Gygi and G. Galli, submitted (2007).

LAWRENCE
LIVERMORE
NATIONAL
LABORATORY

LLNL-JRNL-408009

Vibrational properties of water under confinement: Electronic effects

D. Donadio, G. Cicero, E. Schwegler, M. Sharma, G. Galli

October 22, 2008

Journal of Physical Chemistry

Vibrational properties of water under confinement: electronic effects.

Davide Donadio[1], Giancarlo Cicero[2], Eric Schwegler[3],
Manu Sharma[1] and Giulia Galli[1]
[1]Department of Chemistry, University of California,
One Shields Avenue, Davis, CA 95616
[2] Politecnico di Torino, Turin, Italy
[3]Lawrence Livermore National Laboratory, Livermore, CA 94550

August 29, 2008

Abstract

We compare calculations of infrared (IR) spectra of water confined between non polar surfaces, carried out using *ab initio* and classical simulations. *Ab-initio* results show important differences between IR spectra and vibrational density of state, unlike classical simulations. These differences originate from electronic charge fluctuations at the interface, whose signature is present in IR spectra but not in the density of states. The implications of our findings for the interpretation of experimental data are discussed.

1 Introduction

Given the importance of confined water in a variety of scientific fields,[1] ranging from biology[2–5] to materials science,[6–8] many experimental and theoretical studies have been conducted to determine its properties, yet many of them are still the subject of debate.[9–12]

Interpreting experimental results on water in confined media has proven rather difficult in many instances, and firm conclusions based only on experimental observations are sometimes hard to draw. For this reason it is desirable to interpret and complement experimental data by using atomistic simulations. Recently we have undertaken a series of first–principles computational study of the structural properties of water confined between hydrophilic silicon carbide surfaces[13] and non polar surfaces, including graphene

sheets, carbon nanotubes[14] and deuterated diamond.[15] For all cases we found that the perturbation on the water hydrogen bonded network induced by the confining surfaces is spatially localized within a thin interfacial layer ((∼0.5 nm in the case of non polar substrates and slightly smaller, about 0.3 nm in the case of SiC). An important question yet to be fully addressed is the identification of a set of observables allowing for a clear connection between simulations and existing and future measurements, thus providing a robust probe of the fluid under confinement.

Here we focus on the vibrational properties of confined water, in particular its IR spectra. We compare results obtained using *ab initio* and classical simulations, and we discuss subtle but important electronic effects contributing to IR signals. Such effects can be accounted for only within an *ab initio* framework, and are responsible for specific features found in IR spectra. We chose to compare classical and first principles calculations in the case of graphene, for which well established empirical, interaction potentials are available in the literature. Our findings provide guidance in the interpretation of current and future experimental results, and highlight the importance of considering all contributions determining an IR signal, including electronic ones, and not only incomplete information contained in vibrational density of states. The comparison between IR spectra obtained with *ab initio* and classical calculations also sheds light on the nature of the interaction between water molecules and non polar confining surfaces.

The rest of the paper is organized as follows: in the next section the theoretical framework of our classical and *ab initio* simulations is outlined, and the way we obtained IR spectra from equilibrium molecular dynamics simulations is described. In section 3 we discuss the *ab initio* results for water confined between graphene surfaces, and in Sec. 4 we compare them to the spectra obtained from classical MD simulations. Sec. 5 contains our conclusions.

2 Method

We carried out molecular dynamics (MD) simulations of water confined between graphene sheets at distances varying from 1.01 to 2.5 nm, by using both *ab initio* simulations[15] and classical empirical potentials. In particular, we used a flexible simple point charge model (SPCF)[16] and a polarizable model.[17]

When performing computer simulations, the preparation of a solid/liquid interface within a confined medium is not straightforward. The main diffi-

culty lies in estimating the number of water molecules required to fill up the confined space, in the presence of an excluded volume between the surface and the wetting layer. Such volume is not a priori known and eventually has to be subtracted from the volume accessible to water molecules, in order to determine the density of the confined fluid. To compute the number of water molecules, we determined the initial configuration of the system by using classical simulations with a SPC/E[18] potential in all cases. First a trial system (with a tentative number of water molecules) was equilibrated and then MD runs were repeated either by changing the number of water molecules in the confined space or by varying the dimensions of the confining volume until the stress on the simulation cell corresponds to atmospheric pressure conditions. The samples obtained in this way were used as starting points for both *ab initio* and subsequent classical runs. We chose an SPC/E model to prepare our samples because well tested van der Waals parameters to describe the interaction between water and graphite surfaces and nanotubes (NTs) were available in the literature.[19] In particular the carbon atoms were modeled as neutral particles interacting with the oxygen atoms through a Lennard-Jones potential determined by the parameters $\varepsilon_{CO} = 0.3651$ kJ/mol and $\sigma_{CO} = 0.319$ Å.[19,20] In the graphene/water system the cell dimensions in the (x,y) plane were fixed and determined by the size of a relaxed graphene sheet containing 60 carbon atoms (12.4×12.1 Å). In the z direction the graphene layer distance was optimized to accommodate 32 water molecules. The thickness of the exclusion volume present at the graphene/water interface, as determined by the atomic density profile $\rho(z)$, was estimated to be ∼2 Å.

In classical simulations[21] of IR spectra we used two different parameterizations of the flexible SPC forcefield,[16,22] and a polarizable force field where the oxygen polarizability is described by a Drude model.[17] In these cases, the IR spectra were computed from the autocorrelation function of the total dipole moment $\vec{M}$, which is the sum of the molecular dipoles $\vec{\mu_i}$. The dipole of each water molecule for the flexible simple point charge (SPC) models used in the classical simulations is easily defined: $\vec{\mu}_i = q_O\vec{r}_O + q_H\vec{r}_{H1} + q_H\vec{r}_{H2}$.

In the first principle MD simulations the interatomic interactions are computed by solving the electronic structure within density functional theory using the generalized gradient approximation by Perdew, Burke and Ernzerhof .[23] We adopted norm-conserving pseudopotentials ,[24] and a plane-wave basis set with a cutoff of 85 Ry. In this case, we computed IR spectra using a version of Car-Parrinello (CP)*ab initio* MD[25–27](AIMD), in which maximally localized Wannier functions (MLWFs),[28] in place of Bloch orbitals, are propagated "on-the-fly". MLWFs are equivalent to Boys

orbitals[29] used in Quantum Chemistry. Wannier Functions (WF) are obtained from the eigenstates of the Hamiltonian by a unitary transformation and then MLWF are derived from WF by localization in real space. We use a time step of 7 a.u. (0.17 fs) and a fictitious electron mass of 350 a.u. to integrate the electronic and ionic equations of motion .[25] The main advantage of using MLWF is that we can define the dipole moment of a water molecule μ_i as: $\mu_i = e(6\vec{r}_O + \vec{r}_{D_1} + \vec{r}_{D_2} - 2\sum_{l=1,4}\vec{r}_{W_l})$ where $\vec{r}_{D_1}$, $\vec{r}_{D_2}$ and $\vec{r}_O$ are the coordinates of the deuterium and oxygen atoms, respectively, and $\vec{r}_{W_l}$ are the centers of the four (doubly occupied) MLWFs associated to molecule i. The total polarization is given as the sum of the individual dipole moments of the water molecules and the dipole moment of the surface atoms. The x and y components of the surface dipole have been computed from the atomic and Wannier center coordinates, modulo the "polarization quantum", as in the theory of polarization based on the Berry phase formalism.[30,31]

The IR absorption coefficient per unit length $\alpha(\omega)$ is related to the refractive index $n(\omega)$ and the imaginary part of the dielectric constant $\varepsilon(\omega)$ by $\alpha(\omega)n(\omega) = (\omega/c)\varepsilon(\omega)$. Within linear-response theory, $\alpha(\omega)$ is given by the power spectrum of the time-correlation function of the total dipole operator $\hat{M}$. Here we approximate the quantum time-correlation function with the classical one, i.e., with $\langle M(0)M(t)\rangle$ where M is the total dipole moment in the simulation cell and the brackets indicate classical ensemble averages. The quantum time-correlation function can be expressed in several equivalent ways, leading to formulae for the IR absorption coefficient characterized by different prefactors; these are known as quantum correction factors. Following Refs.,[32–34] we adopt the so-called harmonic approximation (HA) that is obtained by replacing the Kubo-transformed quantum correlation function with the classical one. The quantum corrected line-shape $I(\omega)$ is:

$$I(\omega) = \frac{\beta\hbar\omega}{1 - e^{-\beta\hbar\omega}} I_{cl}(\omega) \tag{1}$$

where β is the inverse temperature and $I_{cl}(\omega)$ is the Fourier transform of the classical $\langle M(0)M(t)\rangle$. In the harmonic regime, the HA is exact. Ramirez et al.[33] showed that HA is the only correction factor that satisfies the fluctuation-dissipation theorem in addition to detailed balance. The same authors also found that HA performs better than the other quantum correction factors for one-dimensional anharmonic potentials modeling several, different H-bond scenarios. In Ref.[34] the HA prefactor was shown to provide a good agreement with experiment, for the relative intensities of IR absorption bands of deuterated bulk water computed within the same *ab initio* framework as in the present work.

In the HA the IR absorption coefficient per unit path length of a sample of volume V is given by:

$$\alpha(\omega)n(\omega) = \frac{2\pi\omega^2\beta}{3cV}\int_{-\infty}^{\infty} dt\ \mathrm{e}^{-i\omega t}\langle \sum_{ij} \boldsymbol{\mu}_i(t)\cdot\boldsymbol{\mu}_j(0)\ \rangle. \qquad (2)$$

All the IR and power spectra presented hereafter have been smoothened by a Fourier filter with a 50 cm^{-1} width.

The IR spectra have been computed in microcanonical (constant number of particles, volume and energy, NVE) MD simulations; the *ab initio* and classical runs were 10 and 50 ps long, respectively. Production runs were performed after equilibrating the system at 350 K[35] and at room temperature, in the *ab initio* and classical case, respectively.

The use of a CP scheme to perform *ab initio* MD involves assigning a fictitious mass to the electronic states (MLWF in our specific case) and a fictitious equation of motion for the electrons is solved at each ionic step, without solving self-consistently the Kohn-Sham problem. Values of this fictitious mass must be chosen carefully, for each specific system, in order not to affect significantly the dynamical properties of the simulated sample, and thus obtain results equivalent to those of Born-Oppenheimer (BO) simulations. In BO simulations at each ionic step the electronic ground state is obtained by solving self-consistently the Kohn-Sham problem.[35] To check how the choice of the fictitious electronic mass affects calculations of IR spectra, we performed a CP simulation of a 16 molecule proton disordered model of hexagonal ice, with $m_e = 350$ a.u. and we compared our results to those obtained by BO molecular dynamics simulations,[14,36] where the MLWF were computed every 1.2 fs (Fig. 1) using the algorithms developed by[37] We observed a red-shift of the high frequency bands computed by CP molecular dynamics, with the shift being larger, the higher the frequency. In the harmonic approximation, if we assign an effective mass $\mathcal{M}$ to harmonic modes of frequency ν, for a fictitious mass m_e, ν is shifted by $\Delta\nu$, such that $\nu+\Delta\nu = \nu/(1+m_e/\mathcal{M})^{\infty/\in}$, with respect to that obtained in BO simulations. Fig. 1 shows that by applying this simple correction term, one achieves good agreement between CP and BO IR spectra, for the value of the fictitious electron mass used in this work. Besides this frequency dependent shift, no significant changes have been observed in the IR line shape of ice computed with CP and BO simulations.

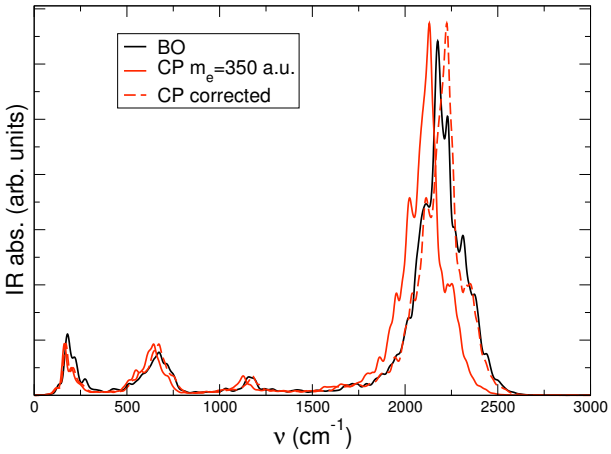

Figure 1: Simulated IR spectrum of ice I_h by Born-Oppenheimer (black solid line) and Car-Parrinello (red solid line) MD with a fictitious electronic mass $m_e = 350$ a.u. The Car-Parrinello IR spectrum, corrected by $\nu + \Delta\nu = \nu/(1+m_e/\mathcal{M})^{\infty/\in}$ assuming M equal to the mass of Deuterium is also shown (red dashed line).

3 Ab initio IR spectra

In this section we present the IR and power spectra of water confined by graphene sheets (composed of 60 C atoms) at a distance of 1.01 nm and discuss the main features of the IR signal arising from electronic effects. Before doing so, we briefly summarize the structural and electronic properties of the interfacial liquid layer.

The structural properties of confined water found in *ab initio* simulations have been presented in Ref.[14] and ,[15] where we have shown that in the presence of a surface delimiting liquid water, density oscillations are induced extending few Angstrom from the interface, with an increased density of molecules in close proximity of the surface. In particular, in proximity of a boundary there exists one (or few) layer(s) of water, which is structurally different from the bulk liquid. Interestingly, we found that the properties of this highly perturbed water layer do not depend on surface separation. In addition, even in the case of high, hydrophobic confinement, the perturbation on water structural properties induced by the surface is localized within a layer 0.3-0.5 nm thick. This is consistent with the results of recent investigations[38,39] where experimentally upper bounds to the surface layer were given (varying between 0.25 and 0.6 nm). It has been suggested[10] that

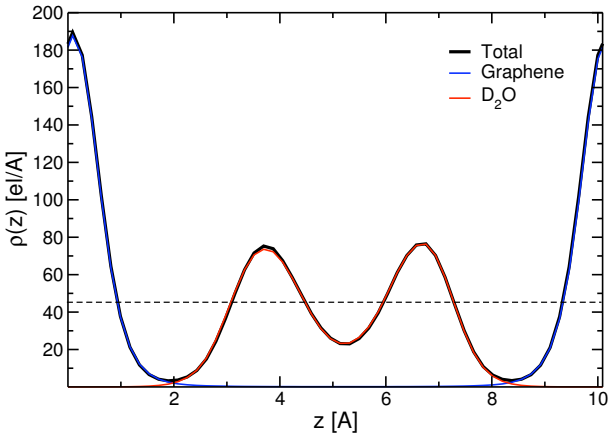

Figure 2: Electron density of the coupled water-graphene system (32 water molecules confined within graphene sheets at a distance of 1.01 nm), as obtained from *ab initio* simulations (see text). The positions of the carbon atoms of the graphene layers are at 0 and 10.1 Å respectively. The red, blue and black curves represent the electronic density of water, graphene and the total density, respectively. The dashed line indicates the average bulk density.

a rarefaction of the density of water is present in proximity of a hydrophobic surface and this topic is still the subject of heated debate. Ref.[10]'s results were recently challenged by Ocko *et al.*[11] and by Kashimoto *et al.*[12] Fig. 2 shows the electronic density as a function of the graphene layer separation as obtained in our calculations. The observed depletion of electronic density in close proximity of the surface (i.e. in a region of linear dimension ∼1 Å from which water molecules are excluded) does not imply and is not accompanied by a rarefaction of water molecules at the interface. In fact, we find a peak of the mass density of water at the graphene interface, similar to that observed at the deuterated diamond interface,[15] showing the absence of a water molecule depletion layer, consistent with the results of Ref.[12]

In Fig. 3, we report the computed IR spectrum of 32 water molecules in contact with graphene at a confinement of 1.01 nm (red line) and we compare it with computed vibrational density of states (v-DOS) (blue line) and with the IR signal obtained for the coupled water-graphene system (black line). The spectrum shown by the red line has been evaluated by restricting the sum yielding the total dipole moment to the water molecules only, when computing the dipole-dipole correlation function. The position of the

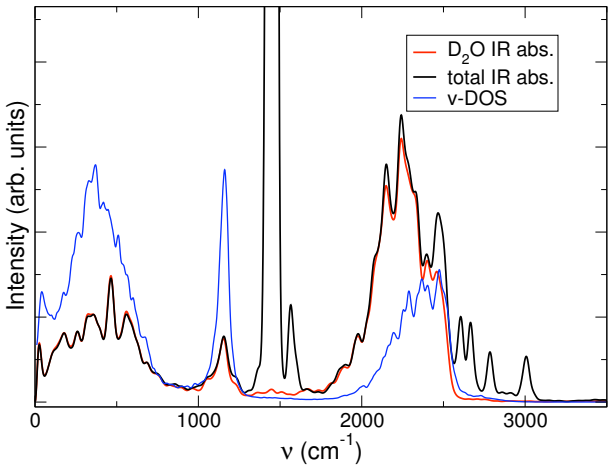

Figure 3: Computed IR spectrum of 32 D_2O molecules confined between graphene sheets at a distance of 1.01 nm. The black and red lines represent the full spectrum (D_2O plus surface) and that of the water molecules, respectively. The blue line represents the power spectrum of D_2O, obtained from the Fourier transform of the velocity autocorrelation functions of the D atoms.

lowest frequency peak and of the bending modes is the same in the v-DOS and IR spectra, although the relative peak intensities are different. The main peak of the high frequency modes is instead shifted towards higher frequencies in the v-DOS, compared to IR, indicating a different IR activities of stretching modes, depending on weather OD bonds are engaged in hydrogen bonding and on the character of the hydrogen bonds (donor or acceptor). An analysis of the ionic trajectories shows that the peak of the v-DOS at 2500 cm^{-1} corresponds to OD bonds not engaged in hydrogen bonding with other molecules, and belonging to molecules in the immediate interfacial region. The feature corresponding to "free" OD bonds in the IR spectrum is much weaker than in the v-DOS, and it appears as a shoulder of the high frequency peak. This indicates that the IR activity of free OD bonds is negligible. This is surprising, as it is well known that stretching modes of a symmetric-top molecules such as water are IR active.

Interestingly the full spectrum (surface plus D_2O), represented by the black line in Fig. 3, does show a peak at $\sim$2500 cm^{-1}. Therefore the difference between the full spectrum and the D_2O spectrum must come from interactions between water molecules and the surface; indeed we find that in the case of interfacial water molecules, the electronic charge density fluctua-

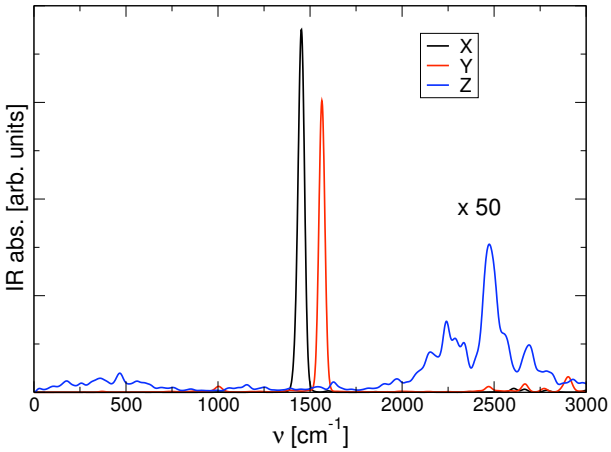

Figure 4: In-plane (X, Y black and red lines) and out-of-plane (Z, blue line) contributions to the graphene sheet IR spectrum, originating from the oscillating dipole of the graphene foils. In the out-of-plane spectrum a correlation with the IR modes of water can be seen by comparing with the results of Fig. 3.

tions at the interface greatly affect the IR activity of O-D bonds not engaged in HB. In particular it is the overlap of the highly polarizable p-electrons of graphene with the electronic charge density of the water molecules that is responsible for the modified IR activity. The intricate interactions of the electrons of graphene with the water molecules are also apparent when decomposing the IR spectrum of the graphene confining surface (Fig. 4) . The power spectrum of graphene shows no modes at frequency higher than $\sim$ 1600 cm^{-1}, while the IR spectrum reveals resonances with the IR modes of water.[15] The in-plane spectrum of the surface contains only a single mode (corresponding to the C-C stretch of the graphene layer); the out-of-plane spectrum contains instead a prominent peak at $\sim$2500 cm^{-1}, and all of its features correlate well with those observed in the water-graphene spectrum. We emphasize that the high frequency peaks of the graphene spectrum are not related to ionic vibrations but to electronic charge fluctuations induced by the interaction with water.

These results show that an explicit treatment of the electronic structure of the surface and of the liquid is required to understand IR spectra and that interpretation of experimental results based solely on vibrational density of states (or power spectra) does not suffice and may be misleading, as it is shown in the following section, where we discuss results obtained using

classical potentials.

It is interesting to note an analogy between the high frequency features observed in our simulated IR spectra and those reported for hydrogenated water confined in CNTs with very high curvature (diameter of $\sim$ 1 nm).[9] The measurements of Ref.[9] have been interpreted as indicating the presence of a new phase of water under confinement, and in particular of weak inter–ring bonds not present in the bulk. Our calculations show that a peak similar to that reported in Ref.[9] may appear due to charge fluctuations between the OD not involved in hydrogen bonds and the confining surface. Therefore, our results provide a possible, alternative interpretation of the data reported in Ref.[9] In fact water tends to form small rings at hydrophobic (or weakly hydrophilic) surfaces, so as to maximize the number of hydrogen bonds, however without altering the local tetrahedral geometry[40] of the fluid. Although we observed the presence of an increased number of 4- and 5-fold membered rings in confined water, with respect to bulk water, we did not find the occurrence of quasi-planar structures in the interfacial fluid, as suggested in ref.[9]

4 Classical MD simulations

In the previous section we have discussed the details of the IR spectra of confined water computed by AIMD simulations. In particular we have shown that accounting explicitly for electronic polarization is essential to achieve a proper description of the interaction between graphene and water, and we have identified the fingerprints of such interaction in IR signals. In classical simulations the surface-water interaction is usually modeled by a Lennard-Jones potential[16,19] that does not include any specific information about the electronic structure of the confining surface, nor about the polarizability of the interfacial water molecules. Here we aim at investigating the impact, on the description of IR spectra, of neglecting the water molecule polarizability, as done in several classical models, or of approximating it *via* a Drude model.

We compared the vibrational density of states obtained from simulations using two different parameterization of the flexible SPC model[16,22] and we conclude that the potential of Ref. [16,41] gives a satisfactory agreement with the power spectrum computed from first principles. In particular, Fig.5 shows that when using this potential there are no qualitative differences between classical MD and AIMD power spectra, except for a small shift of the OD stretching and bending peaks. Based on our results for ice (see Fig.1), we ascribe these differences to inaccuracies of the *ab initio* IR spectra,

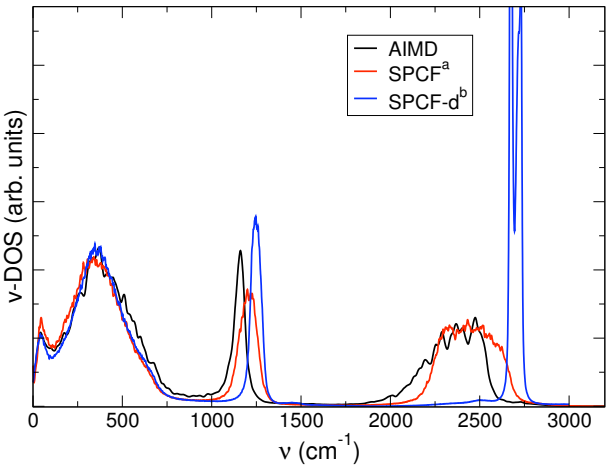

Figure 5: Comparison between the vibrational density of states (v-DOS) of confined water as obtained by using *ab initio* simulations and two different classical force fields: flexible SPC from reference a)[16] and b),[22] respectively.

introduced by the use of a fictitious electron mass in the AIMD simulations. While classical and *ab initio* v-DOS are qualitatively similar, the IR spectra obtained within the two formulations show very important differences both in peak position and relative intensities (see Fig. 6).

As a classical potential does not account for dipole changes occurring in a water molecule upon rigid translation in a charged environment, the low frequency band related to hindered translations (ν less than 250 cm^{-1}) is absent in the classical IR spectrum. The hindered-libration band is instead much amplified and is by far the most intense peak of the spectrum. This effect is strictly related to the fluid in the confined geometry, and it is much less prominent in the IR of bulk water obtained with the same classical potential (inset of Fig 6). The absence of a hindered translation band and the amplification of the hindered libration most likely stem from the unphysical lack of electrostatic coupling between water and the confining medium. In AIMD calculations the hindered libration band is damped by polarization effects on a given molecules, originating from surrounding water molecules; in a confined geometry the intensity of this band is further damped by the polarization of the confining medium (graphene). Indeed we have shown that the IR activity of graphene layers exhibit modes corresponding to all the IR active modes of water (see Fig. 4). The OD bending peak obtained in classical simulations is also more intense than in the AIMD spectra, again

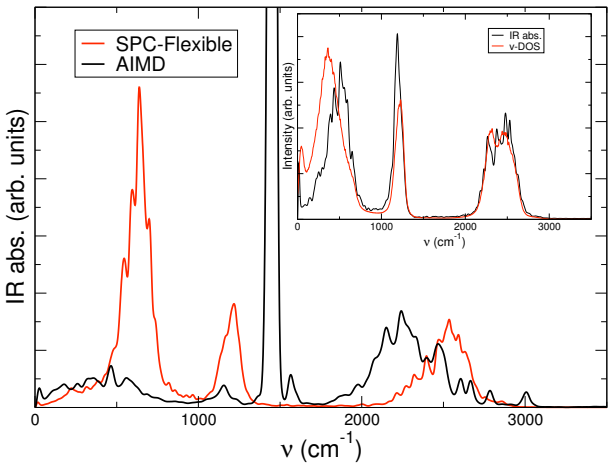

Figure 6: Comparison between classical (red line) and *ab initio* (black line) IR spectra of water confined between two graphene sheets at a distance of 1.01 nm. The inset shows the power spectrum (red) and the IR spectrum (black) of bulk water from classical MD simulations adopting the SPCF force field.[16]

because of lack of polarization effects from the aqueous environment; in this case the confining medium does not appear to play a significant role . The OD bending peak has similar relative intensity in the bulk and in the confined geometry; in addition the corresponding out-of-plane component of the graphene signal, found in the *ab initio* simulation,is rather weak, indicating no substantial coupling between the water molecules and the electrons of graphene. In the high frequency OD stretching band, the mode related to non hydrogen-bonded OD bonds does not appear as a distinct feature in the classical spectrum, however a slight shift of the IR peak towards high frequencies with respect to the bulk is found.

From the comparison shown above we conclude that even when using a flexible point charge potential yielding v-DOS in very good agreement with those obtained ab initio, the IR line shapes differ substantially from those found in first principle calculations. This disagreement is due to the fact that classical model potentials do not account for water-surface interactions and polarization effects in a physical sound manner.

A possible route to incorporate polarization effects in a classical simulation is to use a polarizable Drude model. We therefore probed the IR spectrum of bulk and confined water, as described by the polarizable model by Lamoureux *et al.*[17] This model, dubbed SWM4-NDP, is built upon the

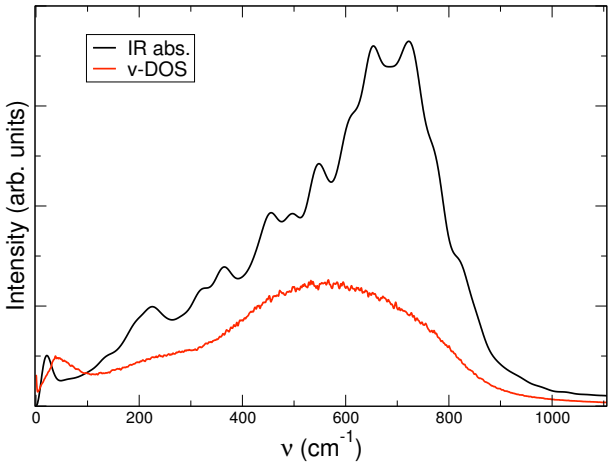

Figure 7: IR spectrum (black line) and vibrational density of states (red) of confined water from classical MD simulations where the polarizable SWM4-NDP potential[17] is adopted.

TIP4P model.[42] The water molecules are treated as a rigid bodies with fixed O-H length (0.9572 Å) and HOH angle (104.52^o). A massless point charge is placed along the symmetry axis of the molecule in order to account for the permanent dipole moment of water. In addition to this TIP4P like model, the SWM4-NDP force field has a charged shell associated to the oxygen atoms. The oxygen shell and core have opposite charges and therefore account for the effect of a varying dipole. As the water molecules are treated as rigid bodies, by using the SWM4-NDP model we can only probe the far infrared part of the spectrum, which is related to hindered translations and librations. The IR and power spectra of confined water are compared in Fig. 7. At variance with the other classical models considered so far, hindered translational modes are found to be IR active, although the position of the peak in the IR spectrum is shifted with respect to the power spectrum. IR active translational modes have been previously observed for bulk water in Ref.,[43] by using a classical polarizable forcefield, however they differ from those found experimentally and by AIMD,[44] since they obey different selection rules. The ratio of the intensities of translational and librational modes is imbalanced in favor of the latter, this indicates that, as for the SPCF model, a screening term coming from the surface polarization is missing to attenuate the dipole fluctuations along the z axis.

5 Conclusions

In summary, we have presented a comparison between IR spectra of water confined within graphene layers, obtained by using *ab initio* and classical simulations. We have shown that in order to describe the interaction of water with non polar surfaces and to account for IR spectra, electronic charge density fluctuations occurring at the interface must be explicitly taken into account. In the near-IR region, *ab initio* vibrational and IR spectra show important differences arising from electronic effects, that is electronic charge fluctuations occurring at the interface. We have also shown that even in the case of classical potentials yielding v-DOS in good, qualitative agreement with *ab initio* results, computed classical and *ab initio* IR spectra differ substantially, due to the lack of a proper account of water-surface interaction and water polarization effects in classical simulations. The use of a polarizable Drude model for water brings classical and *ab initio* simulations into better qualitative agreement, however one should describe also the confining surface as a polarizable system to achieve a satisfactory description of the system.

Finally, our *ab initio* simulations show that all of the notable features found in IR spectra of water confined within graphene layers arise from mere interface effects, i.e. from interactions occurring in close proximity of the interface, and not from new phases of water under confinement.

We gratefully acknowledge support from Scidac grant No. DE-FG02-06ER46262. Part of this work was performed under the auspices of the U.S. Dept. of Energy at the University of California/Lawrence Livermore National Laboratory under contract no. DE-AC52-07NA27344.

References

1. Buch, V.; Devlin, J. P. *Water in confining geometries;* Springer Series in cluster physics Springer: Berlin, 2003.
2. Bryant, R. G. *Ann. Rev. Biophys. Biomol. Str.* **1996,** *25,* 29.
3. Israelachvilli, J.; Wennerstrom, H. *Nature* **1996,** *379,* 219.
4. Balavoine, F.; Schultz, P.; Richard, C.; Mallouh, V.; Ebbesen, T. W.; Mioskowski, C. *Angew. Chem. Int. Ed.* **1999,** *38,* 1912.
5. Nguyen, C. V.; Delzeit, L.; Cassell, A. M.; Li, J.; Han, J.; Meyyappan, M. *Nano Lett.* **2002,** *2,* 1079.
6. Holt, J. K.; Park, H. G.; Wang, Y.; Stadermann, M.; Artyukhin, A. B.; Grigoropoulos, C. P. *Science* **2006,** *312,* 1034.
7. Majumder, M.; Chopra, N.; Andrews, R.; Hinds, B. J. *Nature* **2005,** *438,* 44.
8. Karaborni, S.; Smit, B.; Heidug, W.; Urai, J.; van Oort, E. *Science* **1996,** *271,* 1102.
9. Byl, O.; Liu, J.-C.; Wang, Y.; Yim, W.-L.; Johnson, J. K.; Yates, J. T. *J. Am. Chem. Soc.* **2006,** *128,* 12090.
10. Poynor, A.; Hong, L.; Robinson, I. K.; Granick, S.; Zhang, Z.; Fenter, P. A. *Phys. Rev. Lett.* **2006,** *97,* 266101.
11. Ocko, B.; Dhinojwala, A.; Daillant, J. *Phys. Rev. Lett.* **2008,** *101,* 039601.
12. Kashimoto, K.; Yoon, J.; Hou, B.; hao Chen, C.; Lin, B.; Aratono, M.; Takiue, T.; Schlossman, M. L. *Phys. Rev. Lett.* **2008,** *101,* 076102.
13. Cicero, G.; Grossman, J. C.; Catellani, A.; G, G. *J. Am. Chem. Soc.* **2005,** *127,* 6830-6835.
14. Cicero, G.; Grossman, J. C.; Schwegler, E.; Gygi, F.; Galli, G. *J. Am. Chem. Soc.* **2008,** *130,* 1871.
15. Sharma, M.; Donadio, D.; Schwegler, E.; Galli, G. *Nano Lett.* **2008,** *in press,*.

16. M. C. Gordillo, G. N.; Marti, J. *J. Chem. Phys.* **2005,** *123,* 054707.

17. Lamoureux, G.; MacKerell Jr., A. D.; Roux, B. *J. Chem. Phys.* **2003,** *119,* 5185.

18. Berendsen, H. J. C.; Grigera, J. R.; Straatsma, T. P. *J. Phys. Chem.* **1987,** *91,* 6269-6271.

19. Werder, T.; Walther, J. H.; Jaffe, R.; Halicioglu, T.; Koumoutsakos, P. *J. Phys. Chem. B* **2003,** *107,* 1345-1352.

20. Jaffe, R. L.; Gonnet, P.; Werder, T.; Walther, J. H.; Koumoutsakos, P. *Molecular Simulation* **2004,** *30,* 205-216.

21. Smith, W.; Leslie, M.; Forester, T. R. "DLPOLY version 2.16", CCLRC, Daresbury Laboratoy, Daresbury, England.

22. Deng, L. X.; Pettitt, B. M. *J. Chem. Phys.* **1987,** *91,* 3349.

23. Perdew, J. P.; Burke, K.; Ernzerhof, M. *Phys. Rev. Lett.* **1996,** *77,* 3865.

24. Hamann, D. R.; Schluter, M.; Chiang, C. *Phys. Rev. Lett.* **1979,** *43,* 1494.

25. Car, R.; Parrinello, M. *Phys. Rev. Lett.* **1985,** *55,* 2471.

26. Sharma, M.; Wu, Y.; Car, R. *Int. J. Quantum Chem.* **2003,** *95,* 821.

27. *http://www.quantumespresso.org* .

28. Marzari, N.; Vanderbilt, D. *Phys. Rev. B* **1997,** *56,* 12847.

29. Boys, S. F. *Rev. Mod. Phys.* **1960,** *32,* 296.

30. Resta, R. *Rev. Mod. Phys.* **1994,** *66,* 899.

31. King-Simth, R.; Vanderbilt, D. *Phys. Rev. B* **1993,** *47,* 1651.

32. Bader, J. S.; Berne, B. J. *J. Chem. Phys.* **1994,** *100,* 8359.

33. Ramirez, R.; Lopez-Ciudad, T. L.; P, P. K.; Marx, D. *J. Chem. Phys.* **2004,** *121,* 3973.

34. Chen, W.; Sharma, M.; Resta, R.; Galli, G.; Car, R. *Phys. Rev. B* **2008,** *77,* 245114.

35. Grossman, J. C.; Schwegler, E.; Draeger, E. W.; Gygi, F.; Galli, G. *J. Chem. Phys.* **2004,** *120,* 300.

36. Gygi, F. "QBOX version 1.33.3", http://eslab.ucdavis.edu/software/qbox.

37. Gygi, F.; Fattebert, J. L.; Schwegler, E. *Comp. Phys. Comm.* **2003,** *155,* 1-6.

38. Mezger, M.; Reichert, H.; Schder, S.; Okasinski, J.; Schroeder, H.; Dosch, H.; Palms, D.; Ralston, J.; Honkimaki, V. *Proc. Natl. Acad. Sci. USA* **2006,** *103,* 18401.

39. Ge, Z.; Cahill, D. G.; ; Braun, P. V. *Phys. Rev. Lett.* **2006,** *96,* 186101.

40. Andreussi, O.; Donadio, D.; Parrinello, M.; Zewail, A. H. *Chem. Phys. Lett.* **2006,** *426,* 115-119.

41. Marti, J.; Padro, J. A.; Guardia, E. *J. Mol. Liq.* **1994,** *62,* 17-31.

42. Jorgensen, W. L.; Chandrasekhar, J.; Madura, J. F.; Impey, R. W.; Klein, M. L. *J. Chem. Phys.* **1983,** *79,* 926.

43. Madden, P. A.; Impey, R. W. *Chem. Phys. Lett.* **1986,** *123,* 502.

44. Sharma, M.; Resta, R.; Car, R. *Phys. Rev. Lett.* **2005,** *95,* 187401.